DEVELOPMENT OF OPTICAL IMAGING METHOD FOR DETECTING RNA-PROTEIN INTERACTIONS

A Dissertation
Presented to
The Academic Faculty

by

Jeenah Jung

In Partial Fulfillment
of the Requirements for the Degree
Doctor of Philosophy in the
Department of Biomedical Engineering

Georgia Institute of Technology

December 2014

DEVELOPMENT OF OPTICAL IMAGING METHOD FOR DETECTING RNA-PROTEIN INTERACTIONS

Approved by:

Dr. Philip J. Santangelo, Advisor
Department of Biomedical Engineering
Georgia Institute of Technology

Dr. Gary J. Bassell
Department of Cell Biology and Neurology
Emory University

Dr. Ravi Bellamkonda
Department of Biomedical Engineering
Georgia Institute of Technology

Dr. John F. McDonald
School of Biology
Georgia Institute of Technology

Dr. Wilbur Lam
Department of Biomedical Engineering
Georgia Institute of Technology

Date Approved: 9/3/2014

ACKNOWLEDGEMENTS

I would like to thank my mom for her guidance and unconditional support. Without her this work would not have been possible. I am grateful to have many teachers and mentors who have encouraged my love of science along the way. I'd like to thank my advisor, Philip Santangelo, for giving me the opportunity to perform this research, encouraging me during the tough times, and supporting me when no one else would. I'd like to thank the members of the Santangelo lab and the IBB core facilities for helping me execute my experiments.

TABLE OF CONTENTS

LIST OF TABLES

LIST OF FIGURES

SUMMARY

The localization and translation of messenger ribonucleic acids (mRNAs) play crucial roles in cellular function and disease pathogenesis, and are regulated by numerous RNA-binding proteins (RBPs) and small non-coding ribonucleic acids (RNAs), called *trans*-acting factors. In recent years, biochemical and imaging methods used to study RNA interactions with these *trans*-acting elements have made several important discoveries in identifying these factors, characterizing how they regulate gene expression, and determining the RNA sequence to which they bind. However, the spatiotemporal information regarding these interactions in subcellular compartments have been difficult to determine or to quantify accurately.

Imaging techniques, such as fluorescence resonance energy transfer (FRET) and fluorescence complementation (FC), have been used to study RNA–protein interactions. In these methods, the RNA is labelled with either SytoxOrange or the MS2 system. Although the Sytox system is bright, it lacks RNA specificity. In comparison, the MS2-based approach is specific but suffers from limited sensitivity for detecting RNA–protein interactions and lacks the ability to detect these interactions at native levels, requiring expression of the RNA or RBP. To image and to quantify native RNA and RNA–protein interactions simultaneously *in situ*, we developed a proximity ligation assay (PLA) using peptide-modified, multiply-labelled tetravalent RNA imaging probes (MTRIPs). This method combines sequence-specific imaging of native RNA with proximity ligation and rolling circle amplification (RCA) and allows for the visualization of RNA-protein interactions.

The goal of this research was to develop and to apply a new method for imaging and quantifying interactions between native, non-engineered RNAs and proteins with single interaction-sensitivity. This method has three important properties. It is compatible with different fixation methods, and immunostaining can be performed in addition to the methodology. It can detect the RNA in live cells and the interaction *in situ*. Lastly, it can produce results that can be quantified easily. We have developed this technique and tested its specificity and sensitivity using two model systems: interactions between the genomic RNA and the N protein of human respiratory syncytial virus as well as those between exogenous transcripts with or without the Human antigen R (HuR) binding site and HuR. To validate this method, its accuracy and utility will be demonstrated in three model systems: *poly(A)+* or *β-actin* mRNAs binding to different cytoskeleton for localization, *poly(A)+* or *β-actin* mRNAs interacting with HuR for stabilization, and *programmed cell death 4* (*PDCD4*) mRNA binding to HuR or T-cell intracellular antigen (TIA1) for translational regulation.

CHAPTER 1

INTRODUCTION

Background

In eukaryotic cells, RNA transcripts are processed extensively. This begins in the nucleus, where they are spliced of unnecessary segments (Padgett, Grabowski et al. 1986, Shapiro and Senapathy 1987, Black 2003), capped with a nucleotide linkage at the 5' end, and extended with adenylate at the 3' end to form a poly(A) tail. The transcripts are then transported to the cytoplasm, where they are further processed for translation and post-transcriptional regulation. These cytoplasmic processes are directed mainly by RNA-binding proteins and small RNAs, which interact with the mRNAs to form ribonucleoprotein (RNP) complexes.

These *trans*-acting factors regulate the stability (Sachs 1993, Chen, Xu et al. 1995, Ross 1995, Fan and Steitz 1998), localization (Martin and Ephrussi 2009, Jung, Lifland et al. 2013), and translation (Pain 1996, Selbach, Schwanhausser et al. 2008, Sonenberg and Hinnebusch 2009) of mRNAs through their interactions with *cis*-acting elements in the target RNA sequence. The importance of interactions between RBP and mRNAs is reflected in various diseases that are associated with incorrectly expressed RBP or interrupted interactions between RBPs and mRNAs (Cooper, Wan et al. 2009).

Fluctuations in the expression level of RBP has been strongly correlated with tumorigenesis (Kim, Hur et al. 2009, Barrios-Garcia, Tecalco-Cruz et al. 2014, Kechavarzi and Janga 2014, Kotta-Loizou, Giaginis et al. 2014). In order to elucidate

how changes in the RBP-mRNA interactions lead to cancer, understanding the frequency, localization, and function of these interactions is necessary. However, conventional biochemical assays, such as immunoprecipitation, or imaging methods, such as fluorescence complementation, are inadequate for meeting these needs. A new technique for imaging and quantifying mRNA-RBP interactions *in situ* is necessary.

mRNA-RBP interactions are important for regulating gene expression

Interactions between the bases within transcripts result in complex higher order structures, which expose the RNA backbone and bases to binding with certain protein groups (Mattaj 1993). For example, Watson-Crick paired helical RNA stems are not as effective for specific protein recognition as double-stranded RNAs. The double-stranded RNAs form A-form helices with accessible minor grooves present hydrogen bond donors and acceptors regardless of the bases, facilitating protein binding (Steitz 1990).

RBPs also may induce conformational changes in the RNA structure (Mattaj 1993). The RNP motif or RNA recognition motif (RRM) consists of 90 to 100 amino acids which form an RNA-binding domain (RBD) that is present in multiple copies in RBPs. The RNP consensus sequence (RNP-CS) consists of two sequences (RNP1 and RNP2) with hydrophobic amino acids throughout the motif. (Swanson, Nakagawa et al. 1987, Bandziulis, Swanson et al. 1989, Kenan, Query et al. 1991) Although RNP1 and RNP2 are highly conserved, they do not distinguish between different RNA sequences. The variable regions in the loops and the termini as well as single-stranded RNA determine RNA-binding specificity. These irregularities have the effect of widening the

major groove (Li, Quon et al. 2010), and this bias toward accessible binding sites can be used to predict *in vitro* interactions between RNA and RBP (Gao, Carson et al. 1994).

But *in vivo*, structural accessibility is not adequate to predict RBP binding to an RNA largely due to difficulty in predicting higher order structure of RNAs (Geis, Flamm et al. 2008). In an RNP, interactions between proteins could affect the RNA structure by bringing together different RNA sequences to form more stable RNP complexes or to influence the binding of other RBPs (Goguel and Rosbash 1993, Wu and Maniatis 1993, Portman and Dreyfuss 1994).

Despite a variety of RBDs, RBPs generally bind to AU-rich or U-rich elements in various mRNAs with little sequence specificity. (Scherly, Kambach et al. 1991, Wang and Tanaka Hall 2001) These regions can be bound by multiple ARE binding proteins (Brennan and Steitz 2001). Additionally, an RBP can have numerous functional targets (Licatalosi, Mele et al. 2008, Hafner, Landthaler et al. 2010), and its interactions with mRNAs are context dependent, since it has different functions in different subcellular compartments (Khorshid, Rodak et al. 2011). Therefore, experiments need to reliably detect the spatiotemporal organization (Rodriguez, Czaplinski et al. 2008, Martin and Ephrussi 2009) and the cellular population heterogeneity (Kaern, Elston et al. 2005) of RBP-mRNA interactions.

For example, Human antigen R (HuR) is a member of the Hu/ELAV family of RNA binding proteins and has various functions in mRNA processing (Hinman and Lou 2008). HuR regulates alternative splicing by binding to U-rich elements (Zhu, Hasman et al. 2006). In the cytoplasm, HuR can stabilize mRNAs, such as c-fos, c-myc,

cyclooxygenase-2, tumor necrosis factor-α (Palanisamy, Jakymiw et al. 2012), by binding to AU-rich elements (AREs) in the 3' untranslated regions (3'UTRs) of mRNAs (Brennan and Steitz 2001, Hinman and Lou 2008). Tristetraprolin (TTP), an ELAV family member, binds to mRNAs via a CCCH zinc finger motif (Blackshear 2002) and regulates the cytoplasmic mRNAs. Unlike HuR that stabilizes mRNAs when bound to the 3'UTR, TTP promotes degradation of mRNAs upon binding to them in the cytoplasm and localizing them to the exosomes (Anant and Houchen 2009). Considering these differences in function and localization, comparing the frequency and the location of HuR- and TTP-mRNA interactions in a cell may demonstrate whether the mRNAs are undergoing stabilization or degradation. No method exists that can describe both the frequency and the localization of these interactions in a single cell.

mRNA-protein interactions can be detected using RNA imaging probes and proximity ligation assay

Multiply-labeled tetravalent RNA imaging probes (MTRIPs) (Santangelo, Lifland et al. 2009) and proximity ligation assay (PLA) (Soderberg, Gullberg et al. 2006) can be combined to detect RNA-protein interactions. MTRIPs consist of a neutravidin (NA) or streptavidin core to which bind fluorophore-labeled 2'O-methyl RNA-DNA chimeric oligonucleotides that are antisense to the mRNA target (Santangelo, Lifland et al. 2009). The neutravidin core of MTRIPs can be modified by conjugating high-affinity tags, like the flag tag, which is readily detectable via antibodies (Ab) (Jung, Lifland et al. 2013). Adding high-affinity tag to the neutravidin is necessary for immunodetection of the probe, because the specificity and variety of species for commercially available

antibodies against neutravidin or streptavidin are lacking compared to those against the high-affinity tags.

In order to modify MTRIPs for PLA compatibility, we synthesized Cy3B-labeled flag-tagged MTRIPs (FMTRIPs) with a molar ratio (MR) of 1 or 2 flag, delivered them into live cells using SLO, and post-hybridization, fixed the cells. FMTRIPs were designed against specific RNA sequences near RBP binding sites. The flag peptides on FMTRIPs provided a partner for a PLA reaction with an RBP. Live-cell hybridization and subsequent fixation obviated the need for antigenicity-reducing formamide, allowing for efficient antibody binding. Anti-flag and anti-RBP antibodies were then added to the cells, followed by oligonucleotide-linked secondary antibodies against the primary antibodies (the proximity probes).

If the RNA and protein interact, the oligonucleotides on the proximity probes came together to form a template for a circularized DNA strand by enzymatic ligation. Catalyzed by the phi29 DNA polymerase, one of proximity probe's oligonucleotides served as a primer for rolling circle amplification (RCA), whereas three mismatched exonuclease-resistant 2'O-methyl RNA nucleotides at the 3' end prevented the other proximity probe's oligonucleotide from acting as a primer. This reaction resulted in a coiled single-stranded DNA, the PLA product, complementary to the circular DNA strand and covalently bound to the antibody-antigen complex. The PLA product was detectable by hybridizing complementary Cy5 equivalent-labeled oligonucleotides (Soderberg, Gullberg et al. 2006).

Probes and PLA can image and quantify mRNA-cytoskeleton interactions

Using both flag-tagged multiply-labeled tetravalent RNA imaging probes (FMTRIP) (Santangelo, Lifland et al. 2009) and proximity ligation assay (PLA) (Soderberg, Gullberg et al. 2006), *poly(A)+* and *β-actin* mRNA interactions with β-tubulin, vimentin, and filamentous-actin (F-actin) were detected in HDFs and A549s. Depolymerization of these cytoskeletal structures in HDF and in A549 cells resulted in no PLA signal, although the mRNAs appeared near the depolymerized elements, suggesting that this method can accurately detect the interacting mRNA and cytoskeleton, not two that may be close together. Generally, in both cell types, we confirmed previous electron microscopy findings (Bassell, Powers et al. 1994). We also observed that significantly more *poly(A)+* and *β-actin* mRNAs were bound to F-actin than the other cytoskeleton. And the PLA punctae were localized to the branching points of actin filaments. Significantly less mRNAs were bound to the intermediate filament or microtubules. As a negative control, probes lacking the flag tag were delivered to cells. No PLA signal was observed in these cells.

Probes and PLA can image and quantify mRNA-HuR interactions

In order to test the specificity of proximity ligation assay (PLA) to detect interactions between HuR and mRNAs, HuR interactions with plasmid-derived mRNAs with or without HuR binding site in varying levels of HuR were studied. We used plasmids that encode RNAs spanning the green fluorescent protein (GFP) coding region and the *c-Myc* 3'UTR (referred to as *c-Myc*) with or without the HuR binding site (*c-Myc AB* and *c-Myc A*, respectively). The 3'UTR A segment precedes the HuR binding site in the B segment. (Kim, Kuwano et al. 2009) We designed RNA imaging probes to target three sites on the *c-Myc* 3'UTR A region, which are proximal to the HuR binding site in

the B region. The probes are not complementary to any native mRNA in Vero cells, which were used for all the experiments. In cells transfected with *c-Myc A*, the plasmid lacking the HuR binding site, we observed no PLA signal between *c-Myc* and HuR, as expected.

With the specificity of the PLA method established, we wanted to test how sensitive this method at detecting varying levels of HuR. We examined HuR interactions with *poly(A)+* or *β-actin* mRNA in HeLa cells transfected with HuR-GFP to overexpress HuR. We observed increased PLA punctae frequency in cells with increased HuR levels. Also, when the transcription was inhibited using actinomycin D, mRNA interactions with HuR increased, and this increase was also observable in the number of PLA punctae.

Post-transcriptional regulation of *PDCD4* by HuR and TIA1 can be demonstrated using RNA probes and PLA

Programmed Cell Death 4 (PDCD4) is a tumor suppressor that is regulated by RBPs, HuR and T-cell Intracellular Antigen 1 (TIA1). The PDCD4 protein binds to and inhibits the activity of the eukaryotic translation initiation factor 4A (eIF4A) (Yang, Jansen et al. 2003). Reduction of PDCD4 protein levels, which is observed in a number of cancer types (Lankat-Buttgereit and Goke 2009), results in an increase in protein production and increased tumor promotion (Cmarik, Min et al. 1999, Yang, Jansen et al. 2003). We extensively characterized the *PDCD4* transcript as a novel target of HuR and TIA1 in a breast cancer cell line, MCF-7 (Soule, Vazguez et al. 1973). In addition to RNA-immunoprecipitation (RNA-IP) with HuR and TIA1, we employed RNA-imaging probes deliverable to live cells (Santangelo, Lifland et al. 2009) and PLA (Soderberg,

Gullberg et al. 2006) to examine the interplay between HuR and TIA1 on the *PDCD4* transcripts with single-interaction sensitivity on a per cell basis. Contrary to previous studies that describe a cooperative relationship between HuR and TIA1 in binding to RNA (Kawai, Lal et al. 2006), we demonstrated that HuR and TIA1 compete for interaction with the *PDCD4* transcript, likely via the 3′UTR and reveal a novel mechanism for fine-tuning the level of PDCD4 protein.

Conclusion

Various RNA-protein interactions can be imaged and quantified in a population of cells with high specificity and sensitivity by combining MTRIPs and PLA. We can detect the localization and frequency of these interactions at a single interaction level on a per cell basis. We achieved similar results as previous electron microscopy findings about mRNA-cytoskeleton interactions. We described changes in mRNA-HuR interactions in cells with varying levels of HuR protein. Ultimately, we uncovered a novel mechanism for post-transcriptional regulation of a tumor suppressor. If the binding site of two RBPs overlap on an mRNA, then the two proteins can compete for the binding site. Thus, an mRNA-stabilizing RBP can compete with a translation-inhibiting RBP as a more complex mechanism for regulating gene expression.

The method presented here has shown much promise for discovering other novel relationships between RBPs for regulating a broad range of mRNAs. This method can be improved to detect interactions between a family of RBPs and mRNAs that underlie cellular function, such as neural plasticity or immune response, or condition, such as tumorigenesis or malignancy. Additionally, it can be used to elucidate intercellular

heterogeneity of mRNA-RBP interactions that direct the gene expression. Such an investigation has never been done before. In addition to cells, this method can be used to study tissue samples. The RNA imaging probes can be used for fluorescence in situ hybridization, and PLA can be easily applied to tissues. Correlating mRNA-RBP interactions in cells to those in tissues can allow us to discover important mechanistic findings for disorders, such as cancer.

References

Anant, S. and C. W. Houchen (2009). "HuR and TTP: two RNA binding proteins that deliver message from the 3' end." Gastroenterology **136**(5): 1495-1498.

Bandziulis, R. J., M. S. Swanson and G. Dreyfuss (1989). "RNA-binding proteins as developmental regulators." Genes Dev **3**(4): 431-437.

Barrios-Garcia, T., A. Tecalco-Cruz, V. Gomez-Romero, S. Reyes-Carmona, I. Meneses-Morales and A. Leon-Del-Rio (2014). "Tristetraprolin Represses Estrogen Receptor alpha Transactivation in Breast Cancer Cells." J Biol Chem **289**(22): 15554-15565.

Bassell, G. J., C. M. Powers, K. L. Taneja and R. H. Singer (1994). "Single mRNAs visualized by ultrastructural in situ hybridization are principally localized at actin filament intersections in fibroblasts." J Cell Biol **126**(4): 863-876.

Black, D. L. (2003). "Mechanisms of alternative pre-messenger RNA splicing." Annu Rev Biochem **72**: 291-336.

Blackshear, P. J. (2002). "Tristetraprolin and other CCCH tandem zinc-finger proteins in the regulation of mRNA turnover." Biochem Soc Trans **30**(Pt 6): 945-952.

Brennan, C. M. and J. A. Steitz (2001). "HuR and mRNA stability." Cell Mol Life Sci **58**(2): 266-277.

Chen, C. Y., N. Xu and A. B. Shyu (1995). "mRNA decay mediated by two distinct AU-rich elements from c-fos and granulocyte-macrophage colony-stimulating factor transcripts: different deadenylation kinetics and uncoupling from translation." Mol Cell Biol **15**(10): 5777-5788.

Cmarik, J. L., H. Min, G. Hegamyer, S. Zhan, M. Kulesz-Martin, H. Yoshinaga, S. Matsuhashi and N. H. Colburn (1999). "Differentially expressed protein Pdcd4 inhibits tumor promoter-induced neoplastic transformation." Proc Natl Acad Sci U S A **96**(24): 14037-14042.

Cooper, T. A., L. Wan and G. Dreyfuss (2009). "RNA and disease." Cell **136**(4): 777-793.

Fan, X. C. and J. A. Steitz (1998). "Overexpression of HuR, a nuclear-cytoplasmic shuttling protein, increases the in vivo stability of ARE-containing mRNAs." EMBO J **17**(12): 3448-3460.

Gao, F. B., C. C. Carson, T. Levine and J. D. Keene (1994). "Selection of a subset of mRNAs from combinatorial 3' untranslated region libraries using neuronal RNA-binding protein Hel-N1." Proc Natl Acad Sci U S A **91**(23): 11207-11211.

Geis, M., C. Flamm, M. T. Wolfinger, A. Tanzer, I. L. Hofacker, M. Middendorf, C. Mandl, P. F. Stadler and C. Thurner (2008). "Folding kinetics of large RNAs." J Mol Biol **379**(1): 160-173.

Goguel, V. and M. Rosbash (1993). "Splice site choice and splicing efficiency are positively influenced by pre-mRNA intramolecular base pairing in yeast." Cell **72**(6): 893-901.

Hafner, M., M. Landthaler, L. Burger, M. Khorshid, J. Hausser, P. Berninger, A. Rothballer, M. Ascano, Jr., A. C. Jungkamp, M. Munschauer, A. Ulrich, G. S. Wardle, S. Dewell, M. Zavolan and T. Tuschl (2010). "Transcriptome-wide identification of RNA-binding protein and microRNA target sites by PAR-CLIP." Cell **141**(1): 129-141.

Hinman, M. N. and H. Lou (2008). "Diverse molecular functions of Hu proteins." Cell Mol Life Sci **65**(20): 3168-3181.

Jung, J., A. W. Lifland, E. J. Alonas, C. Zurla and P. J. Santangelo (2013). "Characterization of mRNA-cytoskeleton interactions in situ using FMTRIP and proximity ligation." PLoS One **8**(9): e74598.

Kaern, M., T. C. Elston, W. J. Blake and J. J. Collins (2005). "Stochasticity in gene expression: from theories to phenotypes." Nat Rev Genet **6**(6): 451-464.

Kawai, T., A. Lal, X. Yang, S. Galban, K. Mazan-Mamczarz and M. Gorospe (2006). "Translational control of cytochrome c by RNA-binding proteins TIA-1 and HuR." Mol Cell Biol **26**(8): 3295-3307.

Kechavarzi, B. and S. C. Janga (2014). "Dissecting the expression landscape of RNA-binding proteins in human cancers." Genome Biol **15**(1): R14.

Kenan, D. J., C. C. Query and J. D. Keene (1991). "RNA recognition: towards identifying determinants of specificity." Trends Biochem Sci **16**(6): 214-220.

Khorshid, M., C. Rodak and M. Zavolan (2011). "CLIPZ: a database and analysis environment for experimentally determined binding sites of RNA-binding proteins." Nucleic Acids Res **39**(Database issue): D245-252.

Kim, H. H., Y. Kuwano, S. Srikantan, E. K. Lee, J. L. Martindale and M. Gorospe (2009). "HuR recruits let-7/RISC to repress c-Myc expression." Genes Dev **23**(15): 1743-1748.

Kim, M. Y., J. Hur and S. Jeong (2009). "Emerging roles of RNA and RNA-binding protein network in cancer cells." BMB Rep **42**(3): 125-130.

Kotta-Loizou, I., C. Giaginis and S. Theocharis (2014). "Clinical significance of HuR expression in human malignancy." Med Oncol **31**(9): 161.

Lankat-Buttgereit, B. and R. Goke (2009). "The tumour suppressor Pdcd4: recent advances in the elucidation of function and regulation." Biol Cell **101**(6): 309-317.

Li, X., G. Quon, H. D. Lipshitz and Q. Morris (2010). "Predicting in vivo binding sites of RNA-binding proteins using mRNA secondary structure." RNA **16**(6): 1096-1107.

Licatalosi, D. D., A. Mele, J. J. Fak, J. Ule, M. Kayikci, S. W. Chi, T. A. Clark, A. C. Schweitzer, J. E. Blume, X. Wang, J. C. Darnell and R. B. Darnell (2008). "HITS-

CLIP yields genome-wide insights into brain alternative RNA processing." Nature **456**(7221): 464-469.
Martin, K. C. and A. Ephrussi (2009). "mRNA localization: gene expression in the spatial dimension." Cell **136**(4): 719-730.
Mattaj, I. W. (1993). "RNA recognition: a family matter?" Cell **73**(5): 837-840.
Padgett, R. A., P. J. Grabowski, M. M. Konarska, S. Seiler and P. A. Sharp (1986). "Splicing of messenger RNA precursors." Annu Rev Biochem **55**: 1119-1150.
Pain, V. M. (1996). "Initiation of protein synthesis in eukaryotic cells." Eur J Biochem **236**(3): 747-771.
Palanisamy, V., A. Jakymiw, E. A. Van Tubergen, N. J. D'Silva and K. L. Kirkwood (2012). "Control of cytokine mRNA expression by RNA-binding proteins and microRNAs." J Dent Res **91**(7): 651-658.
Portman, D. S. and G. Dreyfuss (1994). "RNA annealing activities in HeLa nuclei." EMBO J **13**(1): 213-221.
Rodriguez, A. J., K. Czaplinski, J. S. Condeelis and R. H. Singer (2008). "Mechanisms and cellular roles of local protein synthesis in mammalian cells." Curr Opin Cell Biol **20**(2): 144-149.
Ross, J. (1995). "mRNA stability in mammalian cells." Microbiol Rev **59**(3): 423-450.
Sachs, A. B. (1993). "Messenger RNA degradation in eukaryotes." Cell **74**(3): 413-421.
Santangelo, P. J., A. W. Lifland, P. Curt, Y. Sasaki, G. J. Bassell, M. E. Lindquist and J. E. Crowe, Jr. (2009). "Single molecule-sensitive probes for imaging RNA in live cells." Nat Methods **6**(5): 347-349.
Scherly, D., C. Kambach, W. Boelens, W. J. van Venrooij and I. W. Mattaj (1991). "Conserved amino acid residues within and outside of the N-terminal ribonucleoprotein motif of U1A small nuclear ribonucleoprotein involved in U1 RNA binding." J Mol Biol **219**(4): 577-584.
Selbach, M., B. Schwanhausser, N. Thierfelder, Z. Fang, R. Khanin and N. Rajewsky (2008). "Widespread changes in protein synthesis induced by microRNAs." Nature **455**(7209): 58-63.
Shapiro, M. B. and P. Senapathy (1987). "RNA splice junctions of different classes of eukaryotes: sequence statistics and functional implications in gene expression." Nucleic Acids Res **15**(17): 7155-7174.
Soderberg, O., M. Gullberg, M. Jarvius, K. Ridderstrale, K. J. Leuchowius, J. Jarvius, K. Wester, P. Hydbring, F. Bahram, L. G. Larsson and U. Landegren (2006). "Direct observation of individual endogenous protein complexes in situ by proximity ligation." Nat Methods **3**(12): 995-1000.
Sonenberg, N. and A. G. Hinnebusch (2009). "Regulation of translation initiation in eukaryotes: mechanisms and biological targets." Cell **136**(4): 731-745.
Soule, H. D., J. Vazguez, A. Long, S. Albert and M. Brennan (1973). "A human cell line from a pleural effusion derived from a breast carcinoma." J Natl Cancer Inst **51**(5): 1409-1416.
Steitz, T. A. (1990). "Structural studies of protein-nucleic acid interaction: the sources of sequence-specific binding." Q Rev Biophys **23**(3): 205-280.
Swanson, M. S., T. Y. Nakagawa, K. LeVan and G. Dreyfuss (1987). "Primary structure of human nuclear ribonucleoprotein particle C proteins: conservation of sequence

and domain structures in heterogeneous nuclear RNA, mRNA, and pre-rRNA-binding proteins." Mol Cell Biol **7**(5): 1731-1739.
Wang, X. and T. M. Tanaka Hall (2001). "Structural basis for recognition of AU-rich element RNA by the HuD protein." Nat Struct Biol **8**(2): 141-145.
Wu, J. Y. and T. Maniatis (1993). "Specific interactions between proteins implicated in splice site selection and regulated alternative splicing." Cell **75**(6): 1061-1070.
Yang, H. S., A. P. Jansen, A. A. Komar, X. Zheng, W. C. Merrick, S. Costes, S. J. Lockett, N. Sonenberg and N. H. Colburn (2003). "The transformation suppressor Pdcd4 is a novel eukaryotic translation initiation factor 4A binding protein that inhibits translation." Mol Cell Biol **23**(1): 26-37.
Zhu, H., R. A. Hasman, V. A. Barron, G. Luo and H. Lou (2006). "A nuclear function of Hu proteins as neuron-specific alternative RNA processing regulators." Mol Biol Cell **17**(12): 5105-5114.

CHAPTER 2

DETECTING RNA-PROTEIN INTERACTIONS USING RNA IMAGING PROBES AND PROXIMITY LIGATION ASSAY

The work presented here is an excerpt from Jung, J, Lifland, AW, Zurla, C, Alonas, EJ, Santangelo, PJ (2013). "Quantifying RNA-protein interactions in situ using modified-MTRIPs and proximity ligation." Nucleic Acids Res **41**(1): e12.

Background

RNA-protein interactions have been detected using biochemical assays, such as electrophoretic mobility shift assay (EMSA) (Wassarman 2012) and immunoprecipitation (IP) (Ascano, Hafner et al. 2012), and imaging methods, such as fluorescence resonance energy transfer (FRET) (Huranova, Jablonski et al. 2009) and fluorescence complementation (FC) (Yin, Zhu et al. 2013).

EMSA is one of the earliest methods for detecting RNA-protein complexes (Kumar and Lindberg 1972; Spicer, Schwarzbauer et al. 1977; Fried and Crothers 1981; Garner and Revzin 1981). Fluorescent-, chemiluminescent-, or radioactive-labeled RNAs are incubated with a protein sample to form complexes, and the complexes are separated using polyacrylamide gel electrophoresis (Fried and Crothers 1981; Garner and Revzin 1981). The complexes migrate to the opposite charge through a gel at varying speeds. In a non-denaturing gel with a buffer of near neutral pH and low ionic strength, the stable non-covalent bond between the protein and RNA is maintained, and the larger protein bound RNAs migrate slower through the gel compared to unbound RNAs. Hence, the

RNA-protein complexes are separated based on their size, charge, and shape. Specificity of the assay is tested by comparing migration of complexes formed in varying concentrations of labeled and unlabeled RNA and/or specific or non-specific labeled RNA. Antibodies against the protein can be bound to the complex to increase the size and the shift of the complex compared to the unlabeled control (Cheyette, Ip et al. 1992; Calla-Choque, Figueroa-Angulo et al. 2014). Denaturing gels can be used to examine dissociation of cross-linked RNA-protein complexes. Performing EMSA is simple and low cost and requires minimal knowledge of the RNA-protein interaction, such as recombinant proteins or antibodies for protein isolation and pure nucleic acids encoding the protein-binding RNA sequence (Buratowski and Chodosh 2001).

RNA-IP isolates RNA-protein complexes from cell lysates using antibodies against the RNA-binding protein (RBP) of interest along with its associated RNA, and the extracted RNA can be converted to cDNA and identified via qPCR, microarrays, or sequencing (Setyono and Greenberg 1981; Dreyfuss, Choi et al. 1984). RBPs and RNAs in ribonucleoprotein (RNP) complexes may be cross-linked *in vivo* using ultraviolet light for covalently capturing close (near-covalent bond distances) association before immunopurification of the protein (Greenberg 1980; Wagenmakers, Reinders et al. 1980). This technique is called cross-linking and immunoprecipitation (CLIP). The advantage of cross-linking is that it captures only closely associated RNAs and proteins; therefore, it can be highly specific. But one clear disadvantage is that it may not work for all RBPs or capture all the RNAs bound to a given protein, since the RNA and protein may not be arranged optimally for crosslinking in the complex. (Ule, Jensen et al. 2003; Darnell 2012) CLIP also is limited by the low efficiency of UV 254 nm RNA-protein

crosslinking, and the location of the crosslink is not determinable within the cross-linked mRNA, making it difficult to separate the cross-linked target RNA from the background noncross-linked RNA in the sample (Hafner, Landthaler et al. 2010).

Incorporating 4-thiouridine (4SU) into mRNAs and identifying RBP binding sites by looking for thymidine (T) to cytidine (C) transitions in the sequenced cDNA (Kishore, Jaskiewicz et al. 2011; Ascano, Hafner et al. 2012), photoactivatable-ribonucleoside-enhanced crosslinking and immunoprecipitation (PAR-CLIP) improves upon the CLIP approach. The protein binding sites on the transcripts can be mapped genome-wide using high-throughput sequencing of RNA isolated by CLIP (HITS-CLIP), which provides adequate sampling to predict potential binding sites (Licatalosi, Mele et al. 2008; Zhang and Darnell 2011).

Similar to IPs, RNA pull-down assays also allow extraction of RNA-protein complexes from cell lysates. Conventionally, these assays use high affinity tags, such as biotin. RNA probes can encode the RNA sequence of interest with the affinity tag at the end. These probes can be added to the cell lysate, mimic the RNA of interest, and bind to the RBPs that usually bind to the RNA. The RNA-protein complex can be isolated using an antibody against the affinity tag or the protein of interest. The RNA and protein can be decoupled, and the RNA can be detected by RT-PCR, and the proteins can be detected by western blots or mass spectrometry. The pull-down assays are useful for testing whether an RNA can interact with an RBP. Their high sensitivity allows for detection of low abundant proteins.

Generally, these biochemical assays are excellent for initial identification of interactions between RNAs and proteins. However, a major disadvantage is that these assays require a large quantity of cells for adequate sampling (>2×10^6 cells). Since these approaches observe interactions in a large population of cells, the cell-to-cell variability is missed. Imaging techniques, such as FRET (Huranova, Jablonski et al. 2009; Lorenz 2009) and FC (Rackham and Brown 2004; Yin, Zhu et al. 2013), allow for visualization of single cells and localization of RNA-protein complexes.

FRET is a photophysical phenomenon in which energy is transferred between two fluorophores acting as a donor and acceptor. Fluorophores are attached to two proteins, and their proximity can be detected by the interaction and energy transfer between the tagged proteins. For detection, the two proteins do not need to be interacting directly. Two proteins in the same macromolecular complex may produce a detectable signal (Stanek and Neugebauer 2004; Rino, Desterro et al. 2008). In FRET methods, the RNA is labeled with either SytoxOrange (Lorenz 2009) or the MS2 system (Huranova, Jablonski et al. 2009). Although the Sytox system is bright, it lacks RNA specificity, as it targets nucleic acids in general. The MS2-based approach is specific but suffers from limited sensitivity for detecting RNA-protein interactions. Importantly, it requires expression of RNA containing MS2 binding sites and fluorescent RBP, which makes detecting these interactions at native levels impossible. The MS2 system is also used in FC experiments. A fluorescent protein that is split into two with one bound to the RNA of interest via MS2 system and the other bound to the protein of interest. When these two portions are in proximity, they form a fluorescent complex. (Rackham and Brown 2004; Yin, Zhu et al. 2013)

In these imaging experiments, the intensity of fluorescent signal is measured and compared between the cells. Usually, the fluorescent signal in the cell is dispersed throughout the cytoplasm and difficult to localize to a subcellular structure and to quantify. Additionally, because the signal depends on the expression level of the MS2 binding site containing RNA and fluorescent proteins, it is difficult to normalize it across the cell population for accurate comparison. These imaging methods are optimal for testing whether an RNA can interact with a protein inside a cell but may not be useful for quantifying or localizing the interactions. Hence, a new method is necessary to visualize and quantify RNA-protein interactions at their endogenous levels, such that their localization in subcellular structures can be imaged and the populational heterogeneity can be described. To achieve this, we modified protein-centered RNA imaging probes for RNA detection and combined the probes with proximity ligation assay (PLA) using antibodies against proteins of interest to detect RNA-protein interactions.

Probe synthesis and delivery

In order to image and quantify native RNA and RNA-protein interactions simultaneously *in situ*, we combined multiply-labeled tetravalent RNA imaging probes (MTRIPs) (Santangelo, Lifland et al. 2009) and PLA (Soderberg, Gullberg et al. 2006). MTRIPs consist of a neutravidin (NA) or streptavidin core to which bind fluorophore-labeled 2'O-methyl RNA-DNA chimeric oligonucleotides that are antisense to the mRNA target (Santangelo, Lifland et al. 2009). NA has isoelectric point of 7 and is preferred over the charged streptavidin for limiting charge induced non-specific binding. The nucleic acid ligand may be synthesized commercially with 3-6 amino-modified thymidines to which fluorophores can be attached, a biotin at the 5' end for binding to the

neutravidin core, and a short (5-7) spacer poly(T) or poly(A) sequence to extend the ligand from the surface of NA. N-hydroxysuccinimide (NHS) ester-modified fluorophores were conjugated to the amino on thymidines. For a nucleic acid ligand that is 20-25 nucleotides in length, usually 3-4 thymidines would be amino-modified. Of these, on average, each ligand would be labeled with 2-3 fluorophores, limiting self-quenching. The number of fluorophores may be adjusted for longer or shorter nucleic acid ligand; however, at least 2 fluorophores per ligand is necessary for optimal detection of fluorescence. The multiply labeled monovalent ligands were tetramerized via their binding to neutravidin, which increased probe brightness fourfold. (Santangelo, Lifland et al. 2009; Lifland, Zurla et al. 2011)

MTRIPs can be delivered to cells using reversible cell membrane permeabilization with streptolysin O (SLO) (Santangelo, Lifland et al. 2009; Lifland, Zurla et al. 2011). SLO is a membrane-damaging protein toxin that is produced by most strains of β-hemolytic group A streptococci. These water-soluble toxin molecules bind to cholesterol-containing target membranes to assemble into curved 7.5nm wide, 25-100nm long rod structures that penetrate into the apolar domain of the bilayer. (Duncan and Schlegel 1975; Bhakdi, Tranum-Jensen et al. 1985; Sekiya, Satoh et al. 1993) The embedment of the structure creates transmembrane pores with inner diameter of 24nm and outer diameter of 24-30nm in diameter (Sekiya, Satoh et al. 1993).

Modification of MTRIPs with varying molar ratios of flag peptide

The neutravidin core of MTRIPs can be modified by conjugating high-affinity tags, like the flag tag, which is readily detectable via antibodies (Ab) (Jung, Lifland et al.

2013). Adding high-affinity tag to the neutravidin is necessary for immunodetection of the probe, because the specificity and variety of species for commercially available antibodies against neutravidin or streptavidin are lacking compared to many high-affinity tags. In order to modify MTRIPs for PLA compatibility, we synthesized Cy3B-labeled flag-tagged MTRIPs (FMTRIPs) with a molar ratio (MR) of 1 or 2 flag, delivered them into live cells using SLO, and post-hybridization, fixed the cells. FMTRIPs were designed against specific RNA sequences near RBP binding sites. The flag peptides on FMTRIPs provided a partner for a PLA reaction with an RBP. Live-cell hybridization and subsequent fixation obviated the need for antigenicity-reducing formamide, allowing for efficient antibody binding. Anti-flag and anti-RBP antibodies were then added to the cells, followed by oligonucleotide-linked secondary antibodies against the primary antibodies (the proximity probes). If the RNA and protein interact (<40nm apart (Soderberg, Gullberg et al. 2006)), the oligonucleotides on the proximity probes come together to form a template for a circularized DNA strand by enzymatic ligation. Catalyzed by the phi29 DNA polymerase, one of proximity probe's oligonucleotides serve as a primer for rolling circle amplification (RCA), whereas three mismatched exonuclease-resistant 2'O-methyl RNA nucleotides at the 3' end prevent the other proximity probe's oligonucleotide from acting as a primer. This reaction results in a coiled single-stranded DNA, the PLA product, complementary to the circular DNA strand and covalently bound to the antibody-antigen complex. The PLA product is detectable by hybridizing complementary Cy5 equivalent-labeled oligonucleotides (Soderberg, Gullberg et al. 2006). (**Figure 2.1**)

To confirm the detection of the flag on FMTRIPs, we adsorbed FMTRIPs on glass and immunostained for flag. The flag immunofluorescence (IF) intensity of FMTRIP with a 2 molar ratio of flag (2MR-FMTRIP) was twice that of 1 MR-FMTRIP. IF was minimal using untagged MTRIPs. (**Figure 2.1**) An alternate primary anti-flag Ab showed similar results (**Figure 2.2**). Using FMTRIPs targeting the human respiratory syncytial virus (hRSV) genomic RNA (gRNA) in infected Vero and A549 cells, we characterized the FMTRIP and flag IF signals by their co-localization with a known RBP, the N protein. Because N binds tightly to gRNA, it was expected and confirmed that FMTRIP-labeled gRNA and N immunostaining colocalized (**Figure 2.3**). In A549 cells fixed 48 h post-infection (PI), the mean flag IF intensity increased with increasing flag MR, as observed on glass. The mean Pearson's and Mander's coefficients between flag and gRNA exceeded 0.9, indication that, when bound to gRNA, the flag on FMTRIP remained on the neutravidin and was accessible to its Ab. We detected no difference between MTRIP- and FMTRIP-labeled gRNA (**Figure 2.4**). Vero cells showed similar results.

PLA frequency increases with increasing flag molar ratio

To determine the effect of flag valency, PLA was performed between flag and N in hRSV-infected, FMTRIP-delivered A549 cells. We assumed a PLA product, a micro-sized fluorescent puncta, as an occurrence of interaction between N and gRNA, and that the volume of objects visualized by FMTRIPs correlated with the RNA copy number (Lifland, Zurla et al. 2011). A PLA product appeared as a puncta of consistent size and intensity for a variety of analytes, Ab and cell lines (**Figure 2.1** and **Figure 2.5**), therefore facilitating quantification. At 12 h PI, the mean PLA frequency (number of

PLA punctae/FMTRIP volume) increased with more flag, whereas the mean FMTRIP volume remained similar (one-way ANOVA with Dunn's method, $p = 0.326$). No PLA signal was observed using untagged-MTRIP. (**Figure 2.6**) Likely, not every antibody bound to FMTRIP participated in PLA productivity. As PLA detects interactions present at the time of fixation, we likely detected only a subset of gRNA and N that were bound at that moment. The distance between N and flag Ab may exceed the distance limit for proximity ligation due to their conformation or steric hinderance during virus replication. In the case of 2MR-FMTRIP, the second flag Ab might interfere with the probe binding or ligation. Indeed, for 3MR-FMTRIP, the mean flag IF intensity, as well as the mean PLA frequency decreased below those of 1MR, possibly due to steric hindrance by the additional flag and their Ab or quenching by the additional fluorophores.

Optimal blocking is important for achieving high specificity

For accurate RNA-protein PLA, where the RNA is in low abundance, optimal blocking and antibody titration are crucial. The standard Duolink II blocking solution (Olink Bioscience, Sweden) (std) used for PLA resulted in non-specific signal; modifying it (mod) eliminated the background signal (**Figure 2.7**). Limiting non-specific Ab binding through titration with untagged-MTRIPs as a negative control helped increase the signal-to-noise ratio. With varying N dilution, the mean PLA frequency fluctuated (**Figure 2.8**) concentrations, the specificity decreased, resulting in smaller variance but greater non-specific signal (**Figure 2.8**). For each experiment, we optimized the Ab dilution to achieve the highest specificity and minimum assay variance.

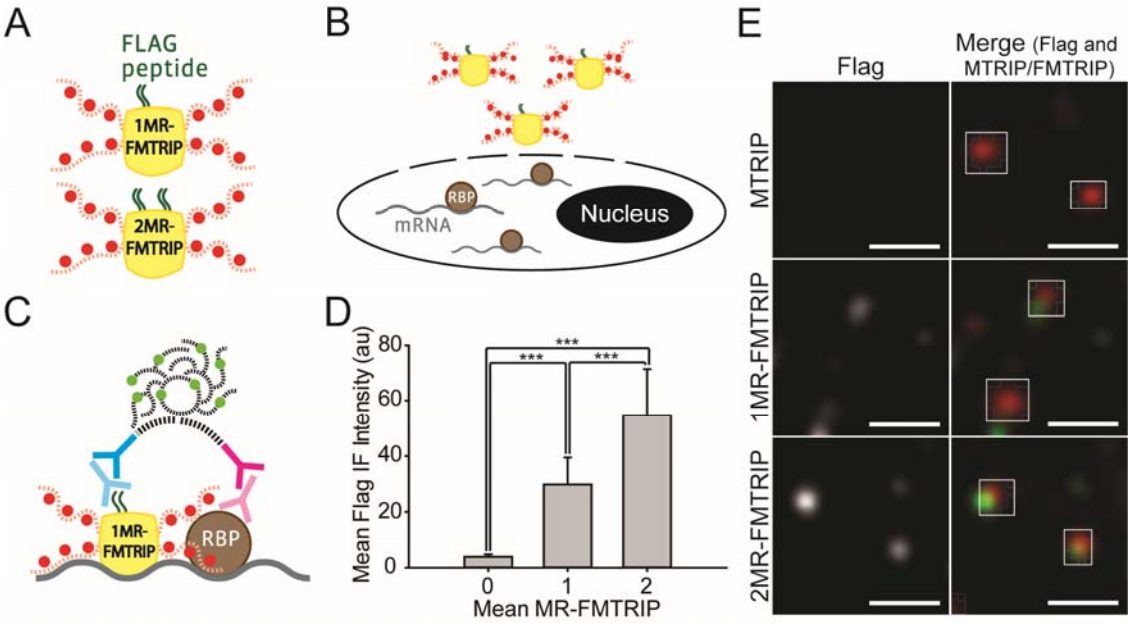

Figure 2.1: Production and imaging of flag-tagged MTRIP (FMTRIP). (A) Flags (dark green) bind to a neutravidin (yellow) with Cy3B-conjugated (red) oligonucleotides to form a 1 or 2 MR-FMTRIP. (B) FMTRIPs enter cells via SLO. (C) Antibodies (Ab) (light blue and magenta) and proximity probes (dark blue and magenta) attach to FMTRIP and RBP (brown) on the mRNA (gray); probes join to synthesize a Cy5-equivalent hybridized product (light green) via RCA. (D) Comparison of the mean flag immunofluorescence (IF) intensity for 0 (n=511, mean = 4, SD = 1), 1 (n=3255, mean = 30, SD = 10) and 2 (n=4724, mean = 55, SD = 17) MR-FMTRIP. (E) Untagged MTRIP, as well as 1 and 2MR-FMTRIP flag IF were imaged using a widefield microscope. MTRIP and FMTRIP (red) and flag IF (green) are merged. Scale bar, 2 µm. a.u., arbitrary units. Error bars, standard deviation. (Jung, Lifland et al. 2013)

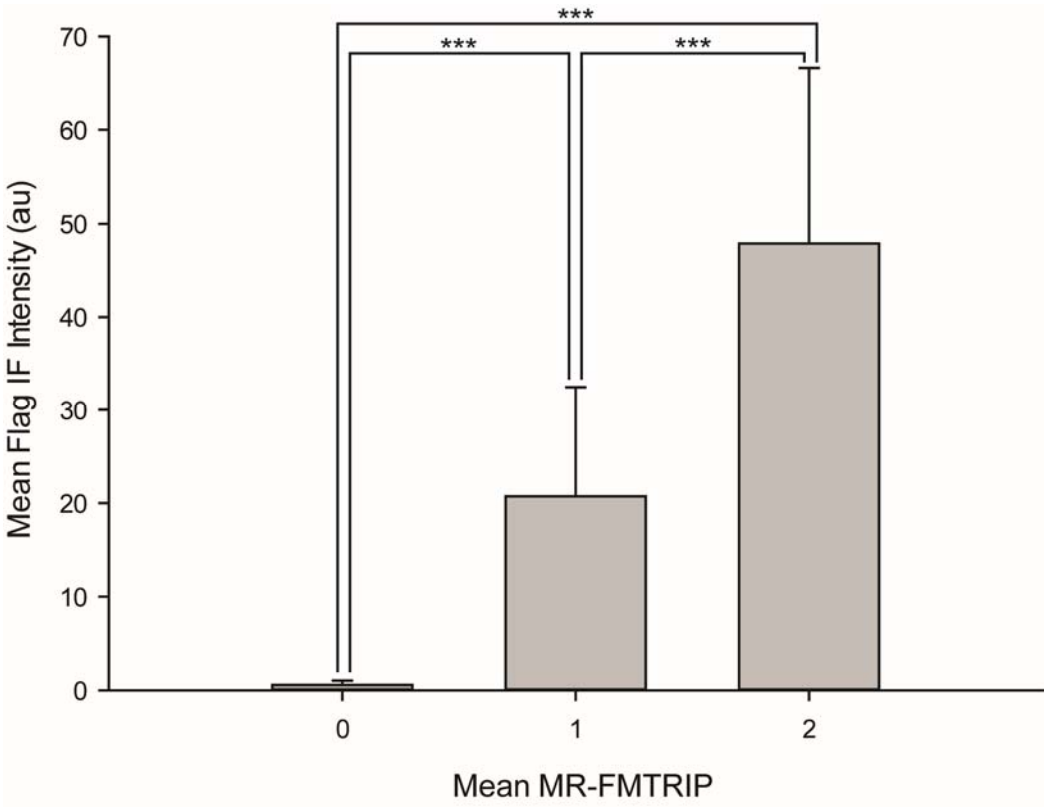

Figure 2.2: Quantification of the mean flag IF intensity of FMTRIPs using mouse anti-flag Ab. The mean flag IF intensity as the mean flag MR-FMTRIP increased from 0 (n=882, mean=0.6, s.d.= 0.5), 1 (n=1583, mean=21, s.d.=12) and 2 (n=1559, mean=48, s.d.=19). ***p<0.001 (one-way ANOVA with Dunn's post-hoc method). a.u., arbitrary units. Error bars, s.d. (Jung, Lifland et al. 2013)

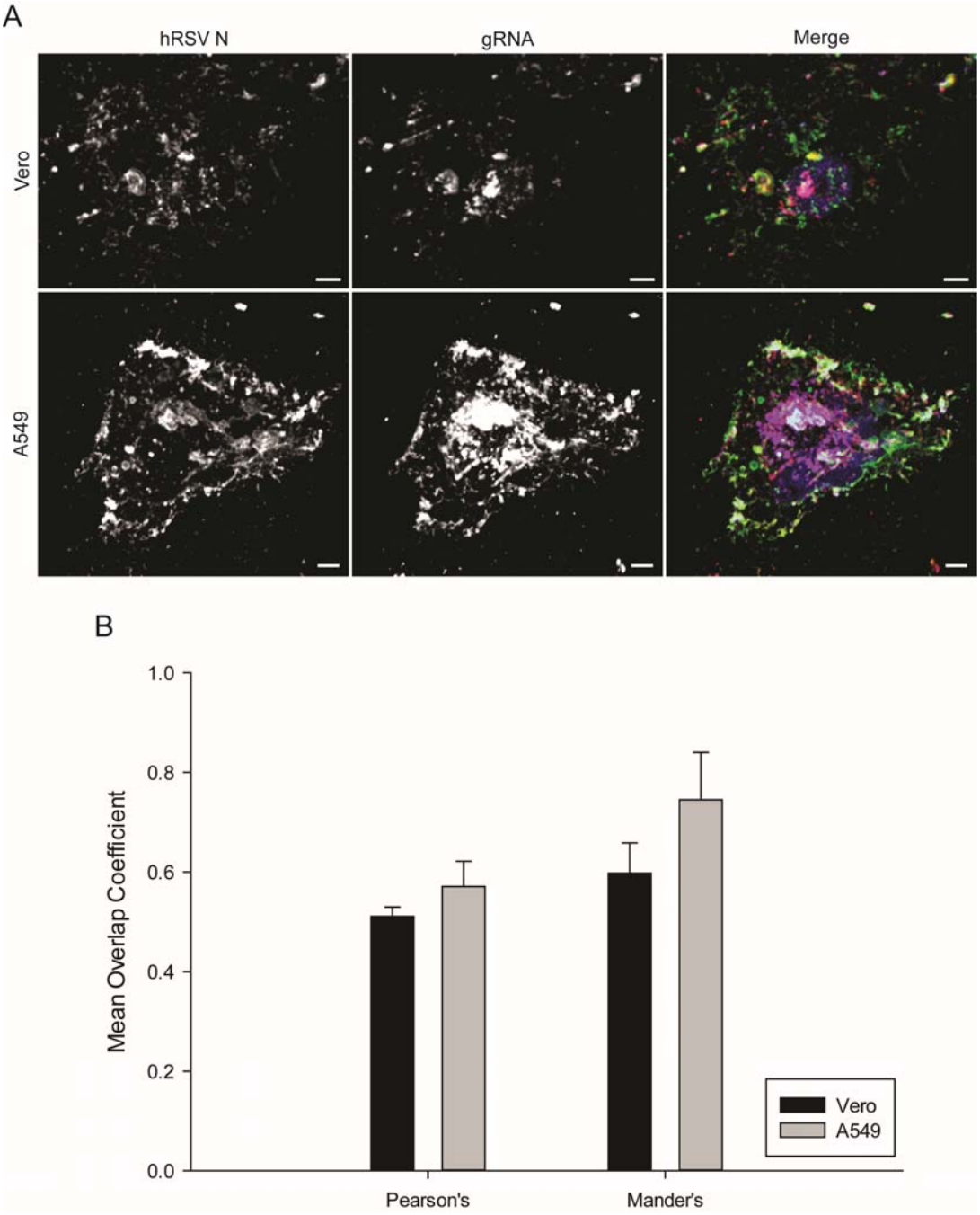

Figure 2.3: Imaging and quantification of colocalization between N IF and hRSV gRNA in Vero and A549 cells 48 h PI. (A) MTRIP-labeled gRNA and N IF in Vero and A549 cells 48 h PI were imaged with scanning laser confocal microscope. Merged images of gRNA (red), N (green) and nucleus (blue) are shown. All planes are represented. Scale bar, 5 µm. (B) The mean Pearson's (Vero: n = 25, mean=0.51, s.d.=0.02; A549: n = 24, mean=0.60, s.d.=0.06) and Manders' (Vero: n = 25, mean=0.57, s.d.=0.05; A549: n = 24, mean=0.75, s.d.=0.10) overlap coefficients showed colocalization between gRNA and N protein. (Jung, Lifland et al. 2013)

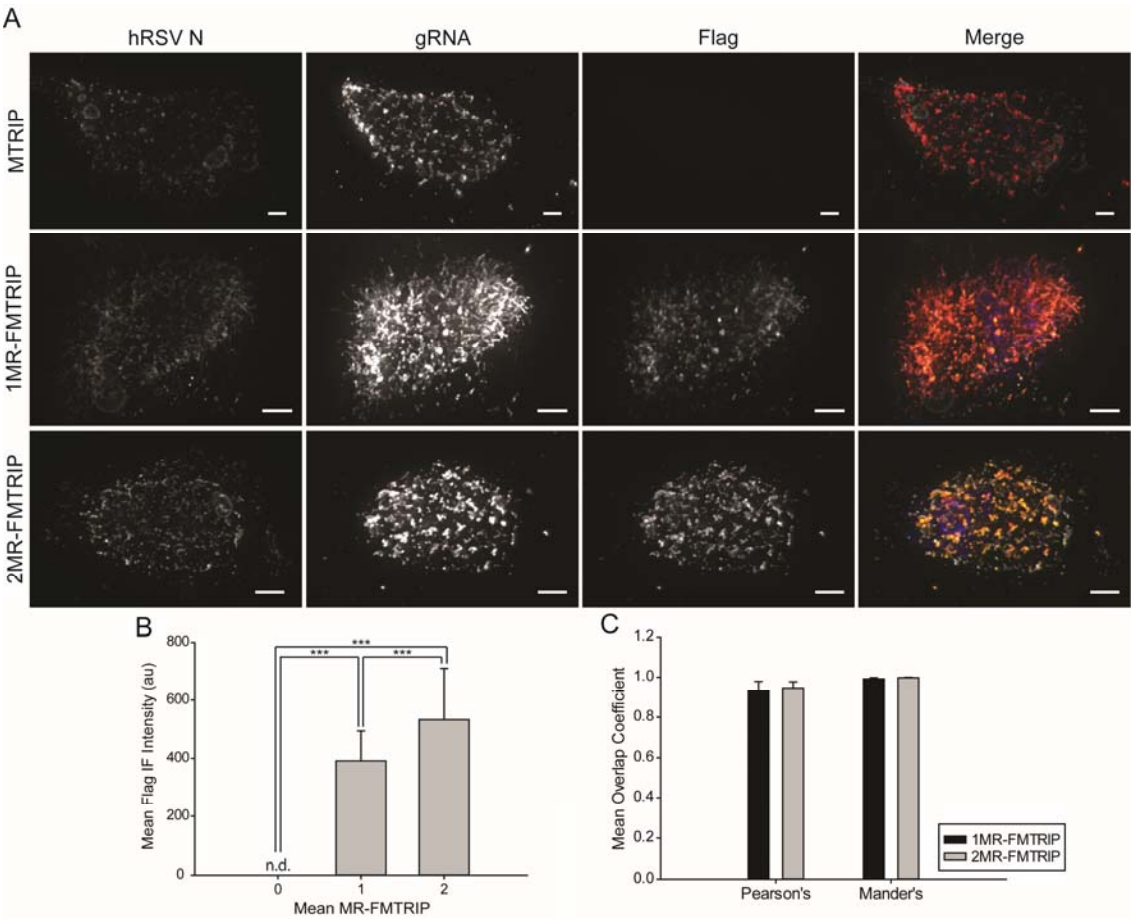

Figure 2.4: Imaging and quantification of colocalization between flag IF and hRSV gRNA in A549 cells 48 h PI. (A) hRSV N IF, gRNA and flag IF in A549 cells with 0, 1 or 2MR-FMTRIP were imaged with a widefield microscope and deconvolved. All image planes represented. Merged images of RSV N (white), gRNA (red), flag (green) and nucleus (blue) are shown. Scale bar, 5 μm. (B) The mean flag IF intensity increased as the mean MR-FMTRIP increased from 0 (n=20, mean=0, s.d.=0), 1 (n=18, mean=391, s.d.=101) to 2 (n=19, mean=532, s.d.=179). Rabbit anti-flag Ab was used. ***p<0.001 (one-way ANOVA with Dunn's post-hoc method). a.u., arbitrary units. n.d., not detected. Error bars, s.d. (C) In hRSV-infected A549 cells with 1 and 2MR-MTRIP, the mean Pearson's (1MR-FMTRIP: n=18, mean=0.93, s.d.=0.05; 2MR-FMTRIP: n=19, mean=0.97, s.d.=0.03) and Manders' (1MR-FMTRIP: n=18, mean=0.99, s.d.=0.01; 2MR-FMTRIP: n=19, mean=1.00, s.d.=0.00) overlap coefficients showed flag and FMTRIP colocalization. No difference in overlap coefficient was observed between 1 and 2MR-FMTRIP (Mann-Whitney rank sum test, p>0.05). Error bars, s.d. (Jung, Lifland et al. 2013)

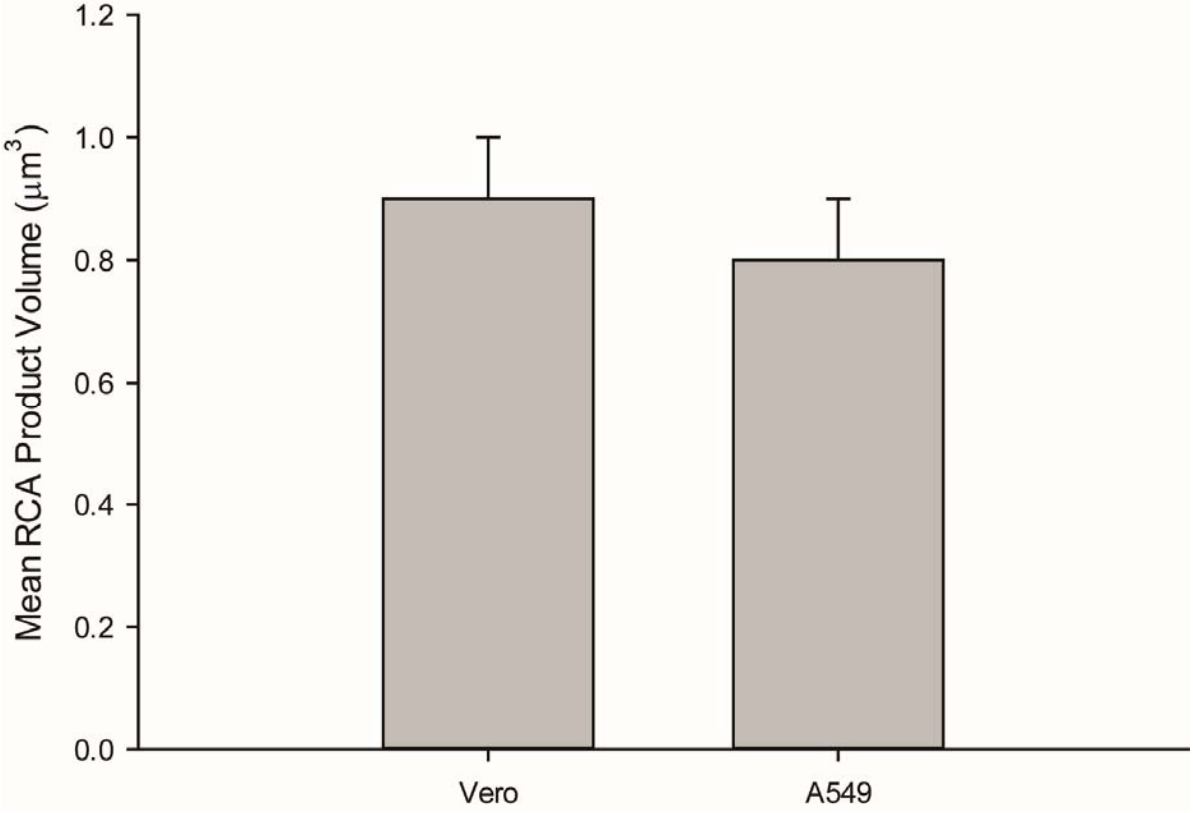

Figure 2.5: The mean RCA product volume in hRSV-infected Vero and A549 cells. Vero (n=93, mean=0.9, s.d.=0.1) and A549 cells (n=93, mean=0.8, s.d.=0.1) were infected with hRSV and fixed after 6, 24 and 48 h. After fixation and blocking, they were immunostained with rabbit anti-flag Ab (1:500 dilution) and mouse anti-N Ab (1:500 dilution), followed by labeling with the proximity probes. The proximity probes were ligated, and RCA reaction occurred for 1 h 40 min. The cells were imaged using a laser scanning confocal microscope. No significant difference was observed between different lengths of infection (two-way ANOVA Holm-Sidak post-hoc method, $p>0.6$). Error bars, s.d. (Jung, Lifland et al. 2013)

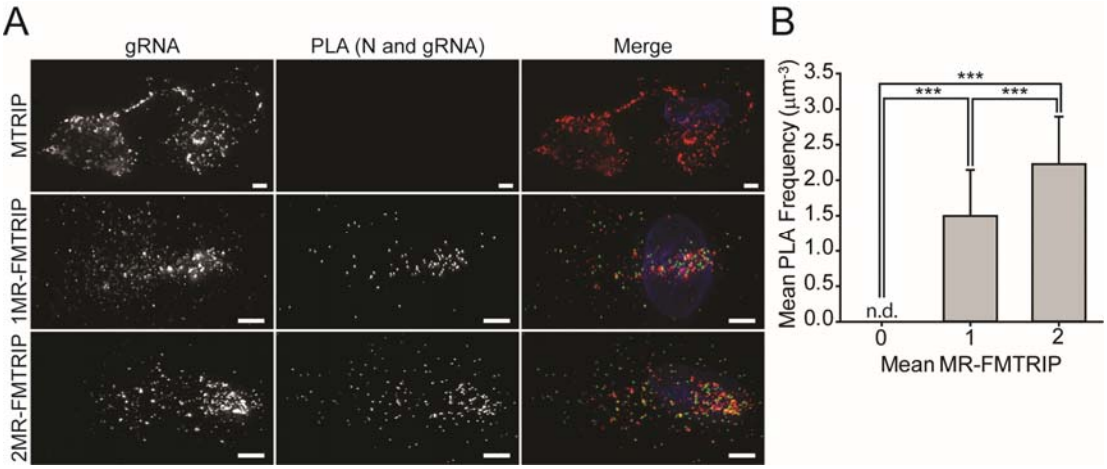

Figure 2.6: Imaging and quantification of hRSV gRNA FMTRIP and PLA with varying flag molar ratio. (A) gRNA FMTRIP and PLA in A549 cells 12 h PI were imaged with a widefield microscope and deconvolved. gRNA (red), PLA (green), and nuclei (blue) are merged. Scale bar, 5 µm. (B) Comparison of the mean PLA frequency for 0 (n = 20, mean = 0, SD = 0), 1 (n = 31, mean = 1.5, SD = 0.6) and 2 (n = 32, mean = 2.2, SD = 0.7) MR-FMTRIP in hRSV-infected A549 cells 12 h PI imaged using a widefield microscope. ***P < 0.001 (one-way ANOVA with Dunn's method. n.d., not detected. Error bars, standard deviation. (Jung, Lifland et al. 2013)

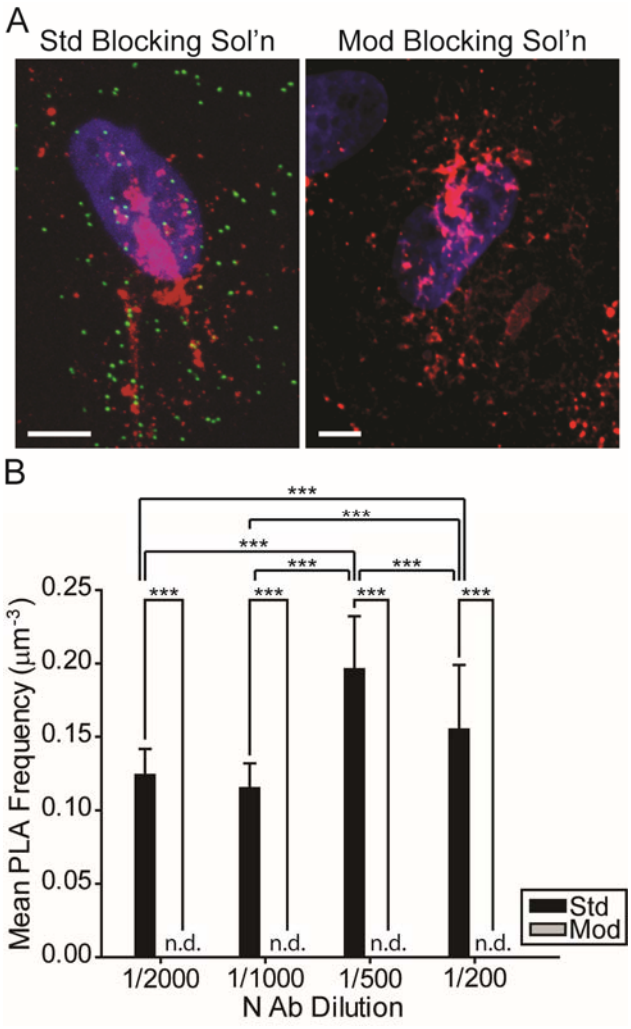

Figure 2.7: Optimization of blocking solution in untagged MTRIP-delivered A549 cells 48 h PI. (A) Merged images of hRSV gRNA (red), PLA between N and gRNA (green) and nuclei (blue) in A549 cells blocked with the standard Duolink II blocking solution (std) or modified blocking solution (mod) are shown. The cells were imaged with a laser scanning confocal microscope. All planes are represented. Scale bar, 5 μm. (B) The mean PLA frequency in cells blocked with std for 1/2000 (n=14, mean=0.12, s.d.=0.02), 1/1000 (n=14, mean=0.12, s.d.=0.02), 1/500 (n=14, mean=0.20, s.d.=0.04), 1/200 hRSV N Ab dilution (n=14, mean=0.16, s.d.=0.04) and mod (1/2000: n=14, mean=0, s.d.=0; 1/1000: n=14, mean=0, s.d.=0; 1/500: n=14, mean=0, s.d.=0; 1/200: n=14, mean=0, s.d.=0). *** $p \leq 0.001$ (two-way ANOVA with Holm-Sidak method). n.d., not detected. Error bars, s.d. (Jung, Lifland et al. 2013)

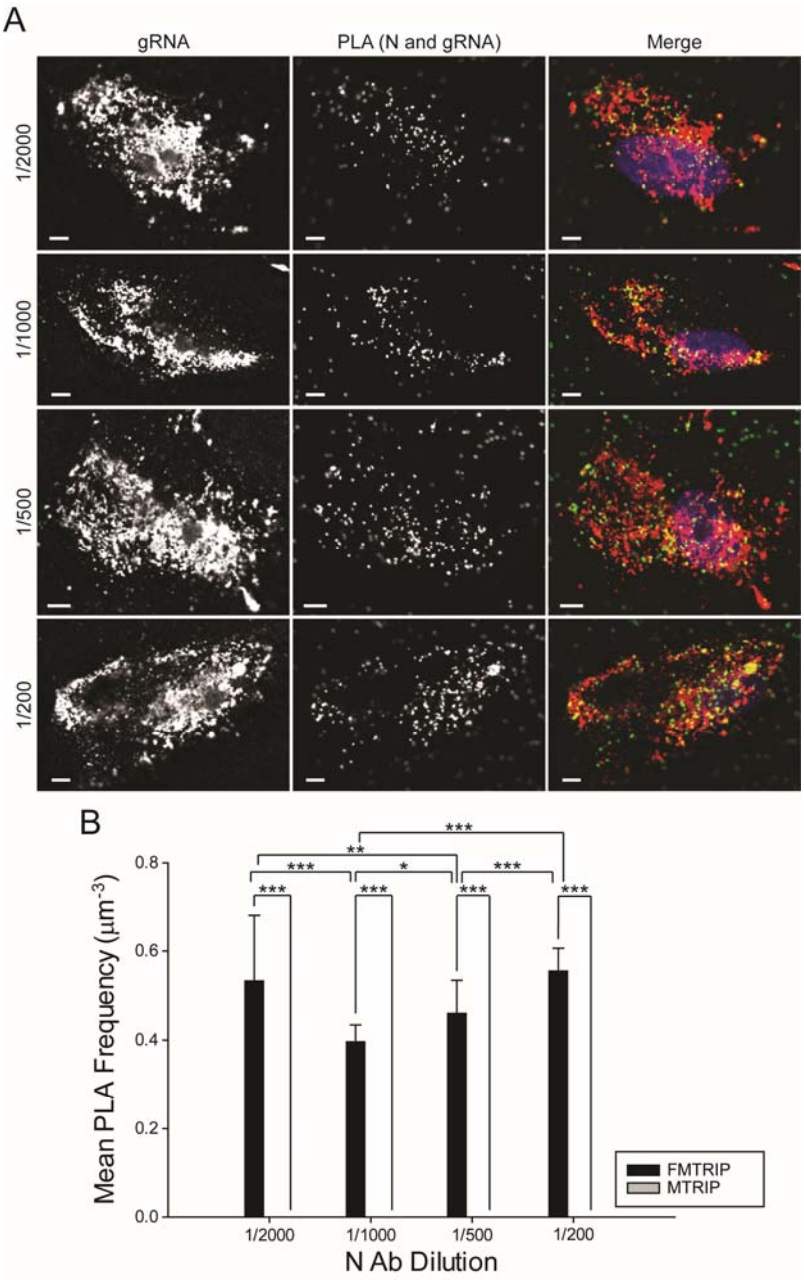

Figure 2.8: Anti-N Ab titration in FMTRIP- and MTRIP-delivered A549 cells 48 h PI. (A) hRSV gRNA and N-gRNA PLA in A549 cells imaged with a laser scanning confocal microscope. Merged images of hRSV gRNA (red), PLA (green) and nuclei (blue) are shown. All planes are represented. Scale bar, 5 µm. (B) The mean PLA frequency increased as hRSV N Ab dilution increased from 1/2000 (n=14, mean=0.53, s.d.=0.15), 1/1000 (n=14, mean=0.40, s.d.=0.04), 1/500 (n=14, mean=0.46, s.d.=0.07), to 1/200 (n=14, mean=0.56, s.d.=0.05) in 1MR-FMTRIP and MTRIP (1/2000: n=14, mean=0, s.d.=0; 1/1000: n=14, mean=0, s.d.=0; 1/500: n=14, mean=0, s.d.=0; 1/200: n=14, mean=0, s.d.=0) . *** $p \leq 0.001$, ** $0.001 < p \leq 0.01$, * $0.01 < p \leq 0.05$ (two-way ANOVA with Holm-Sidak method). Error bars, s.d. (Jung, Lifland et al. 2013)

Materials and methods

Flag-tagged neutravidin was synthesized by first conjugating flag tag-hyNic (Solulink) to neutravidin (Thermo) modified with 4FB (Solulink) using the manufacturer's protocol. The concentration of flag tag-hyNic and 4FB-modified neutravidin were adjusted to produce molar ratio of 1-2 flag/neutravidin. After flag labeling, FMTRIPs were assembled as previously described (Santangelo, Lifland et al. 2009). Briefly, 2'-O-methyl RNA-DNA oligonucleotide chimeras were designed with a 5'-biotin and dT-C6-NH2 internal modifications (Biosearch Technologies). Cy3B-NHS ester fluorophores (GE Healthcare) were conjugated to the oligonucleotide amine groups using the manufacturer's protocol. Free dye was removed using 3kD Amicon spin columns (Millipore). The purified, labeling oligonucleotides were then tetramerized by incubation for 1 h at RT with flag-tagged neutravidin at molar ratio of 5:1. The FMTRIP were assembled separately prior to delivery. Each neutravidin, tetramerized oligonucleotides that target the same sequence. For example, in order to deliver 20nM FMTRIP for each of three targets in an mRNA, 20 nM FMTRIP was incubated with 100nM fluorophore-labeled oligonucleotide that encodes one of three sequnces. Free ligands were removed using 30 kD Amicon spin columns (Millipore). Three 20 nM FMTRIP, each neutravidin bound to four of the same oligonucleotide sequences, were combined to form a 60 nM FMTRIP mixture.

For probe delivery, cells were washed in Dulbeco's phosphate buffered saline (DPBS) without Ca^{2+} and Mg^{2+} (Lonza), and then incubated with 0.2 U/mL activated SLO (Sigma) in OptiMEM (Invitrogen) containing FMTRIP [30 nM, 60 nM, or 20nM

flag-tagged neutravidin] for 10 min at 37 °C. Delivery media were replaced with growth media for 15 min to restore membrane integrity before further experimentation.

After probe delivery and cell recovery, the cells were fixed with 1% paraformaldehyde (Electron Microscopy Science) in PBS for 10min, permeabilized using 0.2% Triton X-100 (Sigma) for 5 min and blocked for 1 h with the standard Duolink II blocking solution (Olink Bioscience) or a modified blocking solution, which consists of 0.5% Tween-20 (CalBioChem), 0.1% Triton X-100, 0.1% gelatin (Aurion), 2% donkey serum (Sigma) and 1% bovine serum albumin (BSA) (EMD) in PBS. Cells were washed with PBS for 5 min. Then they were incubated for 30 min at 37 °C in each of two primary antibodies diluted in 0.25% gelatin, 0.5% Triton X-100, 0.5% donkey serum, and 1% BSA in PBS and then corresponding oligonucleotide-labeled PLA probes (Olink Bioscience) diluted in 0.05% Tween-20 in PBS. They were washed with Duolink wash solution (Olink Bioscience) after each Ab incubation. The ligation and RCA reactions (Olink Bioscience) were performed as instructed in the manufacturer's protocol. Then the cells were immunostained or DAPI-stained (Invitrogen) and mounted on slides using Prolong (Invitrogen).

Unless specified otherwise, all the images were taken using a laser scanning confocal microscope, Zeiss LSM 510 Meta using 63×, numerical aperture (NA) 1.4 Plan-Apochromat objective. Resolution was set to 1024 × 1024. Files were imported into Volocity (PerkinElmer) and linearly contrast enhanced for display. Widefield images were taken on an Axiovert 200 M microscope (Zeiss) with a 63× NA 1.4 Plan-Apochromat objective, and an ORCA-ER AG camera (Hamamatsu). The imaging was

performed using the Volocity acquisition software (PerkinElmer). Image stacks were recorded at 200 nm intervals to adequately sample volumes for iterative deconvolution.

Widefield images were deconvolved using Volocity's deconvolution algorithms (PerkinElmer). FMTRIP and PLA signal quantification, intensity quantification, as well as Mander's and Pearson's coefficients were computed in Volocity and imported into Excel (Microsoft) or Sigma Plot (Systat) for further analysis and plotting. Images presented have been linearly contrast enhanced for clarity. All calculations were performed directly on raw, deconvolved widefield data or raw confocal data.

The volume of RNA and the PLA frequency/RNA volume were measured using Volocity (PerkinElmer). Each cell analyzed individually as follows. Each cell was identified by MTRIP signal or vimentin immunostaining. The RNA volume was determined based on the SD intensity. The PLA signal initially was identified as PLA objects by their SD intensity, then separated into individual punctae using the 'separate touching objects' tool. The objects were further filtered based on size and maximum intensity. For each experiment, we analyzed at least 30 representative cells; experiments were repeated at least twice. In Sigma Plot, Mann-Whitney rank sum test was used to compare FMTRIP volume and the Pearson's and Manders' coefficients; one-way and two-way ANOVA statistical tests were performed to compare PLA frequency across various experimental groups. For one-way ANOVA test, multiple pairwise comparisons were performed with Dunn's method for unequal number of samples and Tukey method for equal number of samples. For two-way ANOVA test, multiple pairwise comparisons were performed with Holm-Sidak.

References

Ascano, M., M. Hafner, et al. (2012). "Identification of RNA-protein interaction networks using PAR-CLIP." Wiley Interdiscip Rev RNA **3**(2): 159-177.

Bhakdi, S., J. Tranum-Jensen, et al. (1985). "Mechanism of membrane damage by streptolysin-O." Infect Immun **47**(1): 52-60.

Buratowski, S. and L. A. Chodosh (2001). "Mobility shift DNA-binding assay using gel electrophoresis." Curr Protoc Mol Biol **Chapter 12**: Unit 12 12.

Calla-Choque, J. S., E. E. Figueroa-Angulo, et al. (2014). "alpha -Actinin TvACTN3 of Trichomonas vaginalis is an RNA-binding protein that could participate in its posttranscriptional iron regulatory mechanism." Biomed Res Int **2014**: 424767.

Cheyette, T. E., T. Ip, et al. (1992). "Characterization of the factors binding to a PEPCK gene upstream hypersensitive site with LCR activity." Nucleic Acids Res **20**(13): 3427-3433.

Darnell, R. (2012). "CLIP (cross-linking and immunoprecipitation) identification of RNAs bound by a specific protein." Cold Spring Harb Protoc **2012**(11): 1146-1160.

Dreyfuss, G., Y. D. Choi, et al. (1984). "Characterization of heterogeneous nuclear RNA-protein complexes in vivo with monoclonal antibodies." Mol Cell Biol **4**(6): 1104-1114.

Duncan, J. L. and R. Schlegel (1975). "Effect of streptolysin O on erythrocyte membranes, liposomes, and lipid dispersions. A protein-cholesterol interaction." J Cell Biol **67**(1): 160-174.

Fried, M. and D. M. Crothers (1981). "Equilibria and kinetics of lac repressor-operator interactions by polyacrylamide gel electrophoresis." Nucleic Acids Res **9**(23): 6505-6525.

Garner, M. M. and A. Revzin (1981). "A gel electrophoresis method for quantifying the binding of proteins to specific DNA regions: application to components of the Escherichia coli lactose operon regulatory system." Nucleic Acids Res **9**(13): 3047-3060.

Greenberg, J. R. (1980). "Proteins crosslinked to messenger RNA by irradiating polyribosomes with ultraviolet light." Nucleic Acids Res **8**(23): 5685-5701.

Hafner, M., M. Landthaler, et al. (2010). "Transcriptome-wide identification of RNA-binding protein and microRNA target sites by PAR-CLIP." Cell **141**(1): 129-141.

Huranova, M., J. A. Jablonski, et al. (2009). "In vivo detection of RNA-binding protein interactions with cognate RNA sequences by fluorescence resonance energy transfer." RNA **15**(11): 2063-2071.

Jung, J., A. W. Lifland, et al. (2013). "Quantifying RNA-protein interactions in situ using modified-MTRIPs and proximity ligation." Nucleic Acids Res **41**(1): e12.

Kishore, S., L. Jaskiewicz, et al. (2011). "A quantitative analysis of CLIP methods for identifying binding sites of RNA-binding proteins." Nat Methods **8**(7): 559-564.

Kumar, A. and U. Lindberg (1972). "Characterization of messenger ribonucleoprotein and messenger RNA from KB cells." Proc Natl Acad Sci U S A **69**(3): 681-685.

Licatalosi, D. D., A. Mele, et al. (2008). "HITS-CLIP yields genome-wide insights into brain alternative RNA processing." Nature **456**(7221): 464-469.

Lifland, A. W., C. Zurla, et al. (2011). "Dynamics of native beta-actin mRNA transport in the cytoplasm." Traffic **12**(8): 1000-1011.
Lorenz, M. (2009). "Visualizing protein-RNA interactions inside cells by fluorescence resonance energy transfer." RNA **15**(1): 97-103.
Rackham, O. and C. M. Brown (2004). "Visualization of RNA-protein interactions in living cells: FMRP and IMP1 interact on mRNAs." EMBO J **23**(16): 3346-3355.
Rino, J., J. M. Desterro, et al. (2008). "Splicing factors SF1 and U2AF associate in extraspliceosomal complexes." Mol Cell Biol **28**(9): 3045-3057.
Santangelo, P. J., A. W. Lifland, et al. (2009). "Single molecule-sensitive probes for imaging RNA in live cells." Nat Methods **6**(5): 347-349.
Sekiya, K., R. Satoh, et al. (1993). "A ring-shaped structure with a crown formed by streptolysin O on the erythrocyte membrane." J Bacteriol **175**(18): 5953-5961.
Setyono, B. and J. R. Greenberg (1981). "Proteins associated with poly(A) and other regions of mRNA and hnRNA molecules as investigated by crosslinking." Cell **24**(3): 775-783.
Soderberg, O., M. Gullberg, et al. (2006). "Direct observation of individual endogenous protein complexes in situ by proximity ligation." Nat Methods **3**(12): 995-1000.
Spicer, E., J. Schwarzbauer, et al. (1977). "Isolation of ribosomal protein-RNA complexes by nitrocellulose membrane filtration: equilibrium binding studies." Nucleic Acids Res **4**(2): 491-499.
Stanek, D. and K. M. Neugebauer (2004). "Detection of snRNP assembly intermediates in Cajal bodies by fluorescence resonance energy transfer." J Cell Biol **166**(7): 1015-1025.
Ule, J., K. B. Jensen, et al. (2003). "CLIP identifies Nova-regulated RNA networks in the brain." Science **302**(5648): 1212-1215.
Wagenmakers, A. J., R. J. Reinders, et al. (1980). "Cross-linking of mRNA to proteins by irradiation of intact cells with ultraviolet light." Eur J Biochem **112**(2): 323-330.
Wassarman, K. M. (2012). "Native gel electrophoresis to study the binding and release of RNA polymerase by 6S RNA." Methods Mol Biol **905**: 259-271.
Yin, J., D. Zhu, et al. (2013). "Imaging of mRNA-protein interactions in live cells using novel mCherry trimolecular fluorescence complementation systems." PLoS One **8**(11): e80851.
Zhang, C. and R. B. Darnell (2011). "Mapping in vivo protein-RNA interactions at single-nucleotide resolution from HITS-CLIP data." Nat Biotechnol **29**(7): 607-614.

CHAPTER 3

mRNA INTERACTIONS WITH THE CYTOSKELETON

The work presented here has been adapted from Jung, J, Lifland, AW, Alonas, EJ, Zurla, C, Santangelo, PJ (2013). "Characterization of mRNA-cytoskeleton interactions in situ using FMTRIP and proximity ligation." PLoS One **8**(9):e74598.

Background

mRNA localization regulates gene expression spatially and temporally by directing transcripts to restricted subcellular compartments for translation, stabilization, or degradation at the appropriate time (Martin and Ephrussi 2009; Xing and Bassell 2013). For example, during stress, mRNAs are degraded in localized foci, such as processing bodies and RNA exosomes (Chen, Gherzi et al. 2001; Kedersha, Stoecklin et al. 2005; Pillai, Bhattacharyya et al. 2007). *β-actin* mRNAs in fibroblasts are localized to the leading edge where actin polymerization promotes forward protrusions (Hill and Gunning 1993; Condeelis and Singer 2005; Rodriguez, Shenoy et al. 2006). Multiple labs have observed an association between mRNA and the cytoskeleton (Hesketh, Campbell et al. 1991; Sundell and Singer 1991; Hill, Schedlich et al. 1994; Glotzer, Saffrich et al. 1997).

Using electron microscopy (EM), *poly(A)+* mRNA in human fibroblasts has been found in association with actin filaments mostly, while less frequently with vimentin and microfilaments (Bassell, Powers et al. 1994). These interactions between mRNA (generally, the 3'UTR), motor proteins, and cytoskeleton have been shown to drive the

localization of mRNAs in various model systems, such as yeast (Takizawa, Sil et al. 1997; Beach, Salmon et al. 1999), Drosophila oogenesis (Theurkauf, Smiley et al. 1992; Shulman, Benton et al. 2000), and neurons (Bassell, Zhang et al. 1998; Wu, Hengst et al. 2005). In both human dermal fibroblasts (HDF) and A549 cells, an epithelial cell line, *β-actin* mRNAs exhibit processive, active transport along the microtubules using kinesin and dynein, while they likely are anchored on the actin filaments (Lifland, Zurla et al. 2011), facilitating translation (Hesketh and Pryme 1991; Condeelis and Singer 2005).

Many experiments for detecting mRNA-cytoskeleton interactions and identifying the *cis*- and *trans*-acting factors have been performed using biochemical assays (Jansen 2001; Jambhekar and Derisi 2007), such as electrophoretic mobility shift (Raju, Fukuda et al. 2011) and immunoprecipitation (Ling, Fahrner et al. 2004; Jonson, Vikesaa et al. 2007; Swanger, Bassell et al. 2011), or imaging methods, such as *in situ* hybridization (Bassell, Powers et al. 1994; Swanger, Bassell et al. 2011). For RNA detection, these methods often use exogenously expressed RNAs with MS2, which may be imaged, isolated, and analyzed for binding factors (Bertrand, Chartrand et al. 1998; Zimyanin, Belaya et al. 2008; Slobodin and Gerst 2010).

While these are useful in identifying RNA-binding proteins (RBP) and whether they bind to the RNA of interest, we describe here a new technology that can study native mRNAs and proteins at their endogenous levels, observe the spatial distribution of the interactions within the cell, and may be performed at high-throughput. Although the *in situ* hybridization EM data (Bassell, Powers et al. 1994) conclusively described the frequency of interactions between *poly(A)+* mRNA and cytoskeletal elements, this approach is low-throughput, laborious, and expensive. It also may introduce sampling

errors due to the evaluation of thin sections of few cells. The ability to image and quantify interactions between mRNAs and cytoskeleton with single interaction sensitivity on a per cell basis will allow us to better understand the significance of these interactions in regulating mRNA localization and gene expression.

Detecting mRNA-cytoskeleton interactions

Using both flag-tagged multiply-labeled tetravalent RNA imaging probes (FMTRIP) (Santangelo, Lifland et al. 2009) and proximity ligation assay (PLA) (Soderberg, Gullberg et al. 2006), *poly(A)+* and *β-actin* mRNA interactions with β-tubulin, vimentin, and filamentous-actin (F-actin) were detected in HDFs and A549s. Cy3B-labeled FMTRIP targeting *poly(A)+* or *β-actin* were delivered into live cells using streptolysin O (SLO), and post-hybridization, the cells were fixed. Using PLA, interactions between the flag tag on FMTRIP-hybridized mRNA and the cytoskeletal elements, β-tubulin, vimentin, or F-actin, were detected in fixed cells. Each interaction between the probe and the cytoskeleton produced a PLA product, a Cy5-equivalent labeled DNA punctae, which can easily be identified and counted. (**Figure 3.1**)

Since the mRNA-cytoskeleton interactions were observed after fixation, we examined the effect of various fixatives. Specifically, we compared paraformaldehyde (PFA) diluted in PBS or in BRB80 (a tubulin retaining fixative) and methanol. Methanol fixation generally provided the best immunofluorescence (IF) images and maintained the mRNA interactions with microtubules (**Figure 3.2**) and intermediate filaments (**Figure 3.3**). For vimentin, differences in the IF images for various fixatives were less obvious than in the microtubules. Still, we observed significant differences between the fixatives

in the percentage of FMTRIP colocalized with PLA and the frequency of PLA punctae, even though no difference was observed in the volume of probes in the cells, suggesting similar probe delivery and hybridization. (**Figure 3.3**) For phalloidin, PFA fixation proved to be optimal, confirming protocols provided by Molecular Probes (Invitrogen, Inc). Therefore, fixatives play an important role in imaging and detecting mRNA-cytoskeleton interactions. One clear advantage of delivering FMTRIPs to live cells is that various fixatives can be used. In conventional FISH assays, probe hybridization to RNAs occurs post-fixation using PFA, which may affect RNA-protein interactions.

Depolymerization of cytoskeletal elements disrupts their interactions with mRNA

To test whether this method accurately detects direct interactions between mRNAs and the cytokeleton rather than mere proximity of the two that might not be in a complex, we depolymerized the cytoskeleton, interrupted mRNA-cytoskeleton interactions, and performed PLA. Poly(A)-targeting FMTRIP were delivered into cells, and PLA was performed between *poly(A)+* mRNA and the cytoskeletal elements, after depolymerizing microtubules with nocodazole, vimentin with acrylamide, or actin with cytochalasin D (cytoD). Depolymerization in HDF and in A549 cells resulted in no PLA signal, although the mRNAs appeared near the depolymerized elements. (**Figure 3.4**) Clearly, this method can accurately detect interacting mRNA and cytoskeleton, not two that may be close together.

This experiment also revealed interesting differences in mRNA dispersal post-depolymerization of various cytoskeletal elements. Depolymerizing β-tubulin didn't change the distribution of the mRNA, as they remained widely dispersed throughout the cytoplasm. But disrupting vimentin and actin resulted in observable differences in the

mRNA localization. In vimentin-depolymerized cells, the mRNA generally clustered around the nucleus, but in actin-depolymerized cells, it moved toward the nucleus as well as the top of the cell. (**Figure 3.4**) This difference in vertical distribution of mRNAs was more apparent in the HDFs than the A549s. (**Figure 3.5**)

***Poly(A)+* mRNAs are bound predominantly to actin in HDF and A549 cells**

To describe how mRNAs generally interact with the cytoskeleton, we studied *poly(A)+* mRNAs in HDF and A549 cells. Poly(A)-targeting FMTRIPs were delivered to cells at 60nM concentration, which is less than the concentration that provide the maximum probe intensity (90nM). By under-sampling the mRNA, FMTRIPs likely bound to the mRNA randomly. This random sampling of mRNAs facilitates imaging individual RNA granules and quantifying relative changes in their interactions with the cytoskeleton. After hybridization and fixation, the interaction of *poly(A)+* mRNA with β-tubulin, vimentin, or actin (marked by phalloidin) were imaged and quantified.

HDFs generally were larger and more spread out with more mRNA (**Figure 3.6**) than the epithelial cells (**Figure 3.7**). The mean probe volume was greater in the HDFs than in the A549s. Despite this difference, the FMTRIP signal was well-dispersed throughout the cytoplasm of both cells, suggesting a broad, random sampling of the mRNAs. Additionally, no difference in the probe delivery and hybridization was observed for different experimental groups; similar volumes of probes were observed in different cytoskeleton groups for each cell types.

Contrastingly, the mean percentage of FMTRIP volume colocalized with PLA signal (PLA-FMTRIP) as well as the mean PLA frequency significantly differed between

mRNA interactions with various cytoskeletal elements. Although the *poly(A)+* mRNA and β-tubulin IF appeared colocalized, their interactions were less than 5% for both HDF and A549 cells. In the HDF, on average, 2.3% FMTRIP volume colocalized with PLA signal between the mRNA and β-tubulin (**Figure 3.6**). This was consistent in A549 cells (**Figure 3.7**). Similarly, the mean PLA frequency normalized by the cell's mRNA volume was minimal for the HDF and the A549 cells. The minimal percentage of mRNA bound to β-tubulin was due to the minimal number of interactions as detected by PLA, rather than smaller aggregates of mRNA bound to β-tubulin. Interactions between the mRNA and vimentin were more frequent in comparison. The mean percentage of PLA-FMTRIP was 11.5% in HDFs. This was similar in A549s (n=28). The mean PLA frequency also was greater in HDFs and A549s.

As previously observed by Bassell et al using EM (Bassell, Powers et al. 1994), we also observed significantly more *poly(A)+* mRNA (53.7%) was bound to F-actin in HDF. The mean *poly(A)+* mRNA and F-actin PLA frequency was consistently the greatest. (**Figure 3.6**) However, for A549, there was no significant difference ($p>0.05$) between vimentin and F-actin. In A549 cells, less mRNA colocalized with PLA between mRNA and F-actin compared to HDFs. The mean PLA frequency also was less. (**Figure 3.7**) Generally, the PLA punctae were localized to the branching points of actin filaments (**Figure 3.6** and **3.7**), as previously observed with EM (Bassell, Powers et al. 1994).

As a negative control, probes lacking the flag tag were delivered to HDF (**Figure 3.8**) and A549 cells (**Figure 3.9**). The delivery and hybridization of flag-less probes were similar to the flagged ones. Only a few interactions, likely due to non-specific interactions, were observed between the mRNA and cytoskeleton. In HDFs, the mean

percentage of PLA-MTRIP was minimal (<0.2%). (**Figure 3.8**) The mean PLA frequency also was insignificant. This was consistent in A549 cells. The mean percentage of PLA-MTRIP was <0.05%, and the mean PLA was minimal. (**Figure 3.9**)

***β-actin* mRNAs also are bound predominantly to actin**

Since we observed that *poly(A)*+ mRNAs predominantly bind to actin and minimally to microtubules, we wanted to see if this was also the case with *β-actin* mRNA. We delivered 50nM FMTRIP targeting *β-actin* mRNA (Jung, Lifland et al. 2013). As previously observed (Santangelo, Lifland et al. 2009; Lifland, Zurla et al. 2011), FMTRIP-bound *β-actin* mRNA was mostly localized in the perinuclear region and the leading edges of the cell. The range of FMTRIP volume was similar in both HDFs and A549s. No difference in the delivery and binding of FMTRIP was observed between the experimental groups. Similar to *poly(A)*+ mRNAs, most mRNAs interacted with F-actin than the other cytoskeletal elements. (**Figure 3.10** and **3.11**) In HDFs, on average, 3.9% of β-actin FMTRIP interacted with β-tubulin, 12.7% with vimentin, and 71.5% with F-actin. The mean frequency of PLA was consistent with the percentage of PLA-FMTRIP. (**Figure 3.10**) In A549 cells, 2.6% β-actin FMTRIP interacted with β-tubulin, 11.8% with vimentin, and 31.3% with F-actin. The mean PLA frequency also was consistent with the percentage of mRNA interacting with the cytoskeleton. (**Figure 3.11**) As with *poly(A)*+ mRNA, *β-actin* mRNAs were predominantly bound to F-actin.

As a negative control, we again delivered flag-less probes targeting *β-actin*. There was no difference in the probe delivery or hybridization between the probes with and without the flag tag (**Figure 3.12** and **3.13**). Minimal interaction was observed (**Figure**

3.12 and **3.13**). As additional negative controls, we used PLA to detect *β-actin* mRNA interactions with nuclear proteins, nucleolin and histone H1. Since the nuclear proteins are predominantly within the nucleus, they generally do not interact with the cytoplasmic *β-actin* mRNA. The probes only target the cytoplasmic mRNAs; therefore, we detected no PLA signal between *β-actin* mRNAs and the nuclear proteins (**Figure 3.14**).

Depolymerization of F-actin increases mRNA binding to the microtubules

Once we determined that depolymerization altered mRNA interactions with the depolymerized element and that we can accurately detect mRNA-cytoskeleton interactions, we asked whether depolymerization of one cytoskeleton altered mRNA interactions with the other, intact, cytoskeletal elements. When F-actin is depolymerized, the cell morphology was noticeably affected. The cytoplasm was reduced significantly with retracted edges, and the mRNA localized in the perinuclear region. Generally, the detected mRNA volume also decreased. However, when the interactions with F-actin were eliminated, the mean percentage of *poly(A)* + mRNA interacting with β-tubulin increased, while interactions with vimentin decreased. Consistently, the mean PLA frequency for interactions with β-tubulin increased, while interactions with vimentin decreased. Hence, changes in the percentage of mRNA interacting with β-tubulin or vimentin were due to changes in the number of PLA, rather than larger mRNA granules colocalizing with PLA. Considering the dramatic changes in the cell morphology, F-actin depolymerization might have also disrupted other cytoskeletal components, such as microtubules and intermediate filaments. However, since *poly(A)* + mRNA interactions with β-tubulin and vimentin resulted in PLA products, β-tubulin and vimentin likely were

not disrupted significantly by cytoD, since their depolymerization would have decreased the PLA signal to undetectable levels. (**Figure 3.4**)

The increase in *poly(A)*+ mRNA binding to β-tubulin and decrease in the binding to vimentin suggest that as mRNA granules separate from F-actin, due to its depolymerization, and likely bind to microtubules. Microtubules have been observed to transport mRNA granules (Lifland, Zurla et al. 2011; Zurla, Lifland et al. 2011), while F-actin has been thought to anchor and translate the mRNA. Moving mRNA granules are unlikely to undergo translation; hence, once the mRNAs separate from F-actin and vimentin, they may bind to microtubules to be transported elsewhere. This will be explored in future experiments. From these experiments, it is clear that depolymerization of F-actin leads to altered mRNA localization, specifically to the microtubules.

Arsenite-induced oxidative stress decreased mRNA binding to F-actin and increased binding to microtubules

In order to further investigate the relationship between mRNA binding to various cytoskeletal components, we examined interactions between *poly(A)*+ mRNA and the cytoskeletal elements at various time points during arsenite-induced oxidative stress. Arsenite is known to induce stress granule formation and alter mRNA localization and translational potential; therefore, a relevant perturbation to the cell. After 5-10 min of arsenite exposure, the *poly(A)* + mRNA interactions with β-tubulin increased significantly. Interactions significantly decreased at 20 min and remained minimal until 40 min. Contrastingly, interactions with F-actin decreased significantly at 5 min and remained low throughout the experiment. Changes in the interactions with vimentin were

not as dramatic. Generally, they remained similar until 40 min, when the percentage mRNAs interacting with vimentin reached their minimum. (**Figure 3.15**)

Zurla et al observed that 15 min after arsenite exposure, the *β-actin* mRNA granules began to accumulate near the nucleus and microtubule-organizing center (MTOC). After 30 min, the cells' morphology changed dramatically with their edges retracted toward the nucleus. They also found that depolymerizing microtubules using nocodazole prevented *β-actin* mRNA from localizing to the MTOC. The increase in the *poly(A)+* mRNA interactions with β-tubulin and the decrease in the interactions with F-actin within the first 10 min of exposure are consistent with previous findings. mRNA granules anchored to F-actin likely separate and bind to microtubules for transport to the perinuclear region and MTOC.

Zurla et al found that within 10 min, the mRNA granules at the cell periphery were not recruited toward the MTOC possibly because they remained bound to the cytoskeleton. (Jung, Lifland et al. 2013) At 10 min after exposure, we also observed PLA signals around the periphery (**Figure 3.15**), which eventually disappeared with extended exposure. By 40 minutes, interactions with β-tubulin, vimentin, and F-actin all decreased to minimal levels. This was likely due to arsenite-induced cytoskeleton instability. Exposure to arsenite led to cell retraction and loss of actin filaments; at higher doses, loss of microtubules and intermediate filaments was observed as well as inhibition of cytoskeletal protein synthesis (Chou 1989; Li and Chou 1992). In these experiments, we found that arsenite altered mRNA localization with the cytoskeleton, promoting interactions with the microtubules over F-actin.

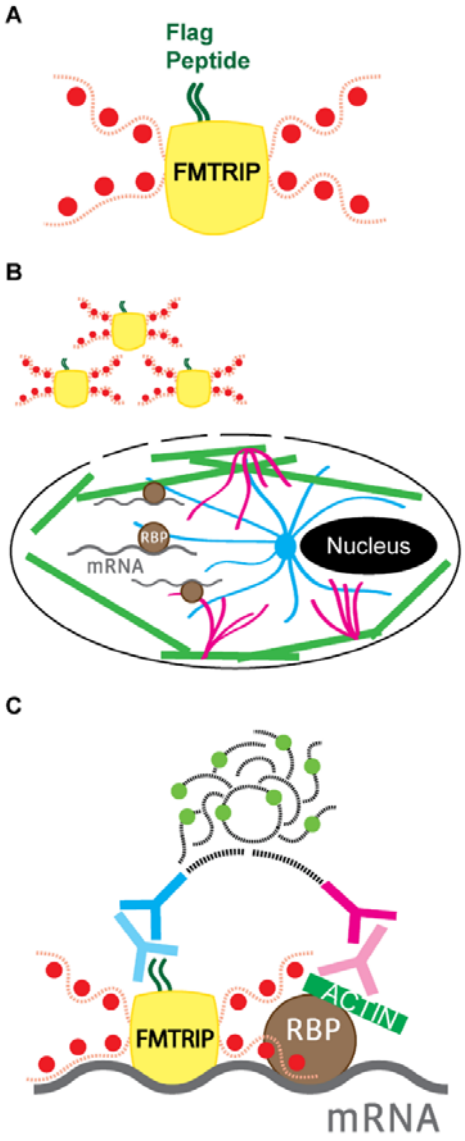

Figure 3.1: Detection of interactions between FMTRIP-hybridized mRNA and cytoskeletal elements using proximity ligation assay (PLA). (A) Flag (dark green) bound to a neutravidin (yellow) with Cy3B-conjugated (red) oligonucleotides (red dash) formed an FMTRIP. (B) Streptolysin O created entrance for FMTRIP in the cell membrane, allowing access to the mRNA (gray) bound to the β-tubulin (blue), vimentin (magenta), and F-actin (green), via RNA-binding proteins (RBP, brown). (C) Antibodies against the flag (light blue) and the cytoskeletal element (light magenta) in addition to the proximity probes against the antibodies (dark blue and magenta) attached to the FMTRIP-bound mRNA (gray) and the cytoskeleton (green); the oligonucleotides (black dash) on the proximity probes join to synthesize a Cy5-equivalent hybridized DNA product (light green and black dash) via rolling circle amplification. (Jung, Lifland et al. 2013)

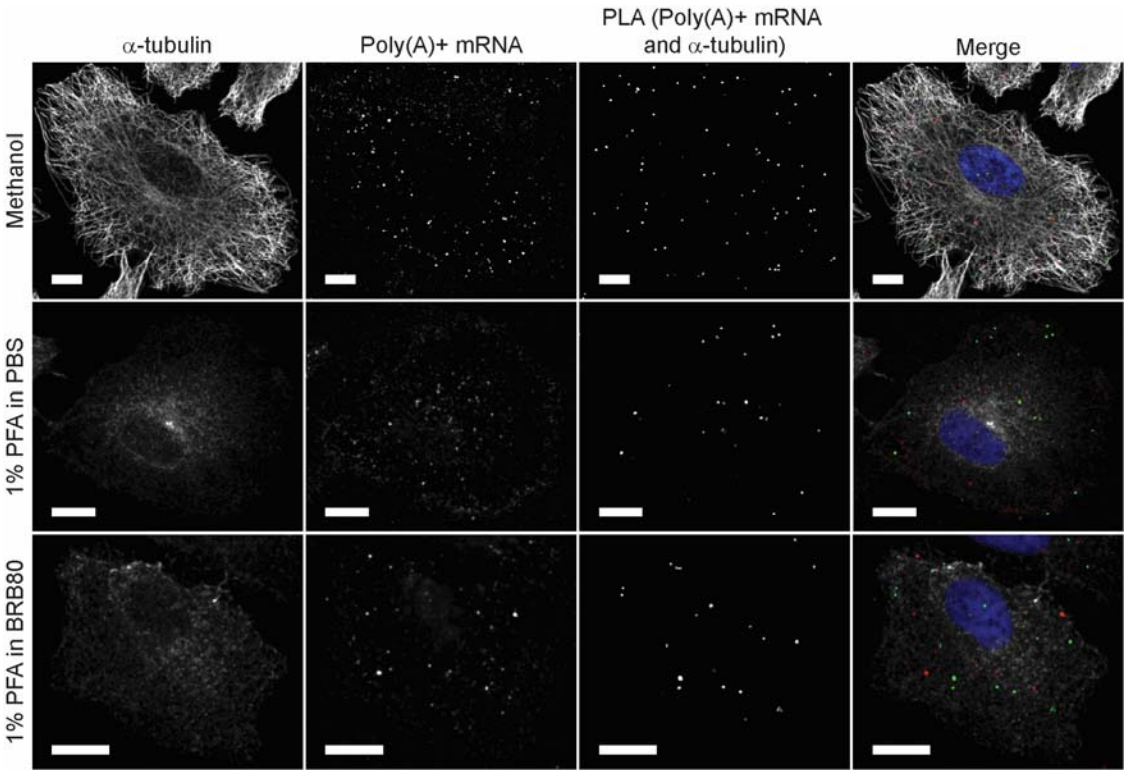

Figure 3.2: Interactions between *poly(A)*+ mRNA and α-tubulin in A549 cells fixed with methanol, 1% paraformaldehyde (PFA) in PBS, and 1% PFA in BRB80. α-tubulin immunofluorescence (IF), *poly(A)*+ mRNA, and proximity ligation assay (PLA) product between *poly(A)*+ mRNA and α-tubulin were imaged with a laser-scanning confocal microscope. Merged images of α-tubulin (white), *poly(A)*+ mRNA (red), PLA (green), and nuclei (blue) are shown. Single image plane is represented. Scale bar, 10μm. (Jung, Lifland et al. 2013)

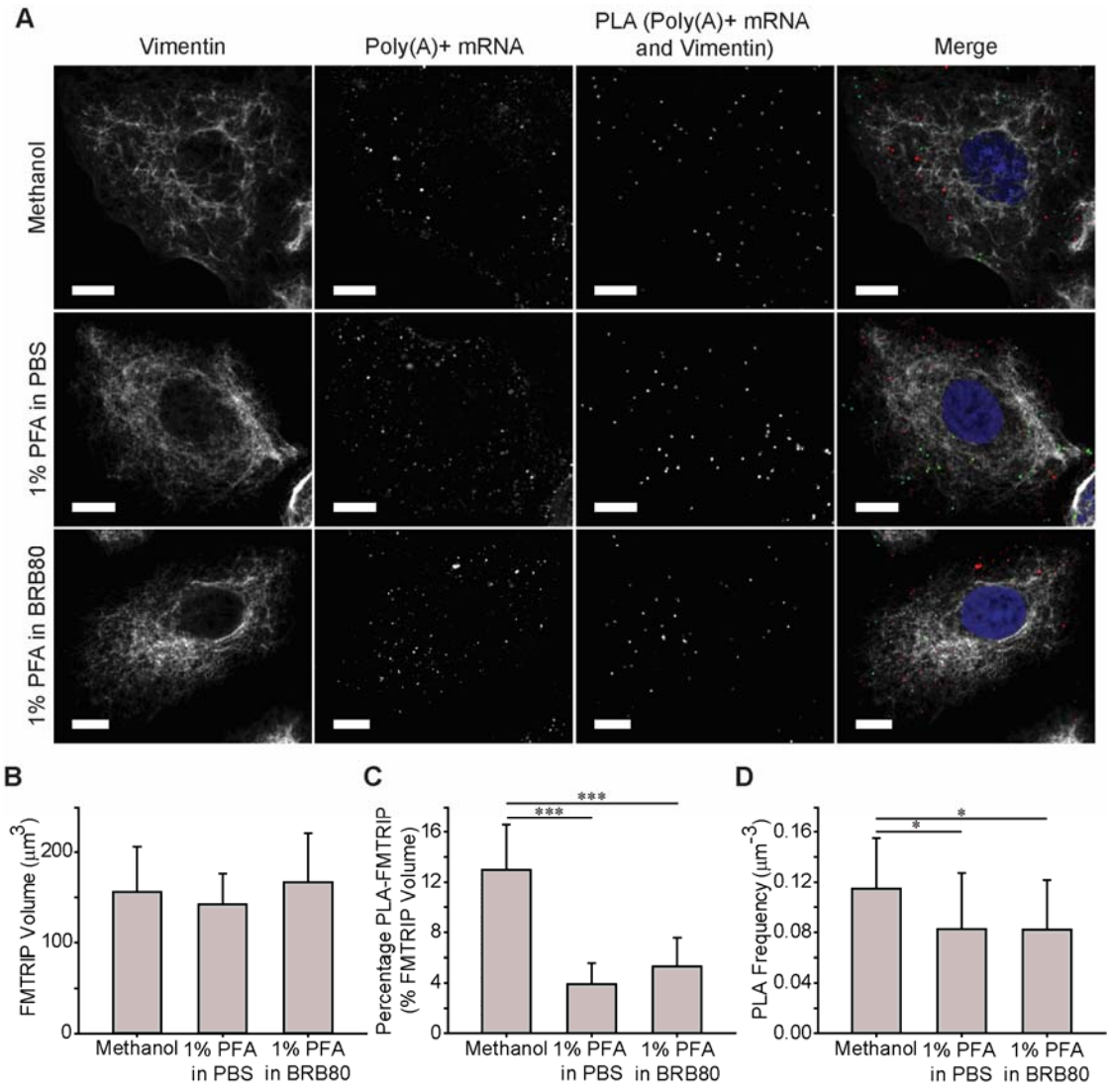

Figure 3.3: Interactions between *poly(A)*+ mRNA and vimentin in A549 cells fixed with methanol, 1% PFA in PBS, and 1% PFA in BRB80. (A) Vimentin IF, poly(A)+ mRNA, and PLA product between *poly(A)*+ mRNA and vimentin were imaged with a laser-scanning confocal microscope. Merged images of Vimentin (white), *poly(A)*+ mRNA (red), PLA (green), and nuclei (blue) are shown. Single image plane is represented. Scale bar, 10 μm. (B) The mean FMTRIP volume was similar (Kruskal-Wallis One Way ANOVA on Ranks, p=0.5) in all fixatives, methanol (n=20), 1% PFA in PBS (n=20), and 1% PFA in BRB80 (n=21). (C) The mean percentage of FMTRIP colocalized with PLA (PLA-FMTRIP) in cells fixed with methanol (n=20) was greater (Kruskal-Wallis One Way ANOVA on Ranks with Dunn's method, ***, $p<0.001$) than those fixed with 1% PFA in PBS (n=20) or 1% PFA in BRB80 (n=21). (D) The mean PLA frequency was greater (Kruskal-Wallis One Way ANOVA on Ranks with Dunn's method, *, $p<0.02$) in methanol fixation (n=20) than in 1% PFA in PBS (n=20) or 1% PFA in BRB80 (n=21). (Jung, Lifland et al. 2013)

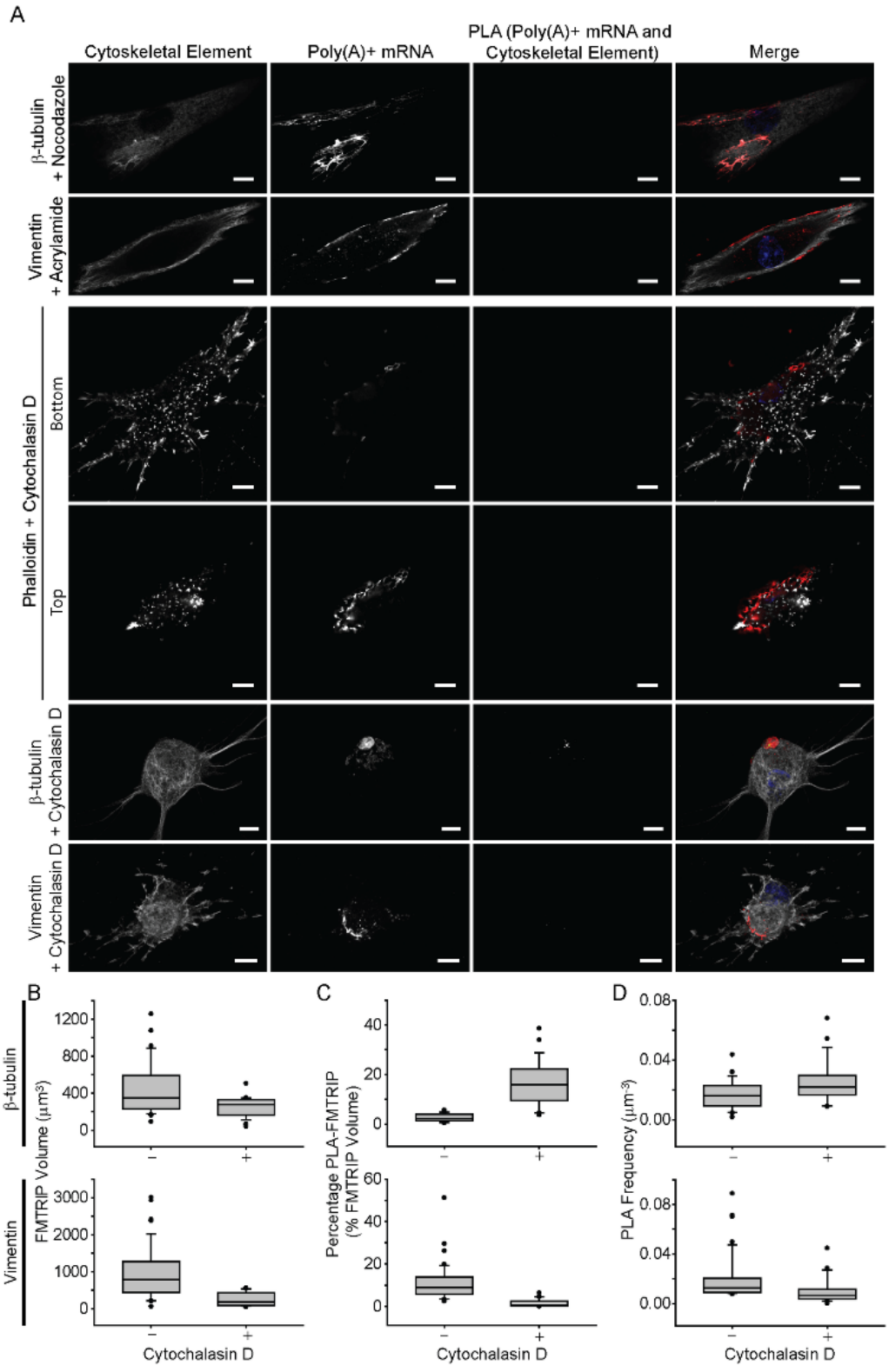

Figure 3.4: Interactions between *poly(A)*+ mRNA and cytoskeletal elements in HDF post-depolymerization of microtubules using nocodazole, intermediate filaments

using acrylamide, and actin using cytochalasin D. (A) β-tubulin, vimentin, and phalloidin immunofluorescence (IF), *poly(A)+* mRNA, and PLA between *poly(A)+* mRNA and the cytoskeletal elements in HDF were imaged with a laser-scanning confocal microscope. Merged images of the cytoskeleton (white), *poly(A)+* mRNA (red), PLA (green) and nuclei (blue) are shown. Single image plane is represented. Scale bar, 10 μm. (B) The mean FMTRIP volume decreased after 90 min exposure to cytochalasin D (Mann-Whitney rank sum test, β-tubulin, $p<0.01$; vimentin, $p<0.01$) in experiments quantifying interactions with β-tubulin (n=21, mean=254μm^3, s.d.=110μm^3) and vimentin (n=16, mean=253μm^3, s.d.=188μm^3). (C) The mean percentage of FMTRIP (PLA-FMTRIP) bound to β-tubulin increased after depolymerization (Mann-Whitney rank sum test, $p<0.001$; n=21, mean=16.3%, s.d.=9.5%) but decreased for vimentin (Mann-Whitney rank sum test, $p<0.001$; n=16, mean=1.5%, s.d.=1.9%). (D) The mean PLA frequency detecting interactions with β-tubulin also increased (Mann-Whitney rank sum test, $p=0.015$; n=21, mean=0.03μm^{-3}, s.d.=0.02μm^{-3}) and decreased for vimentin (Mann-Whitney rank sum test, $p<0.001$; n=16, mean=0.01μm^{-3}, s.d.=0.01μm^{-3}). Error bars, s.d. (Jung, Lifland et al. 2013)

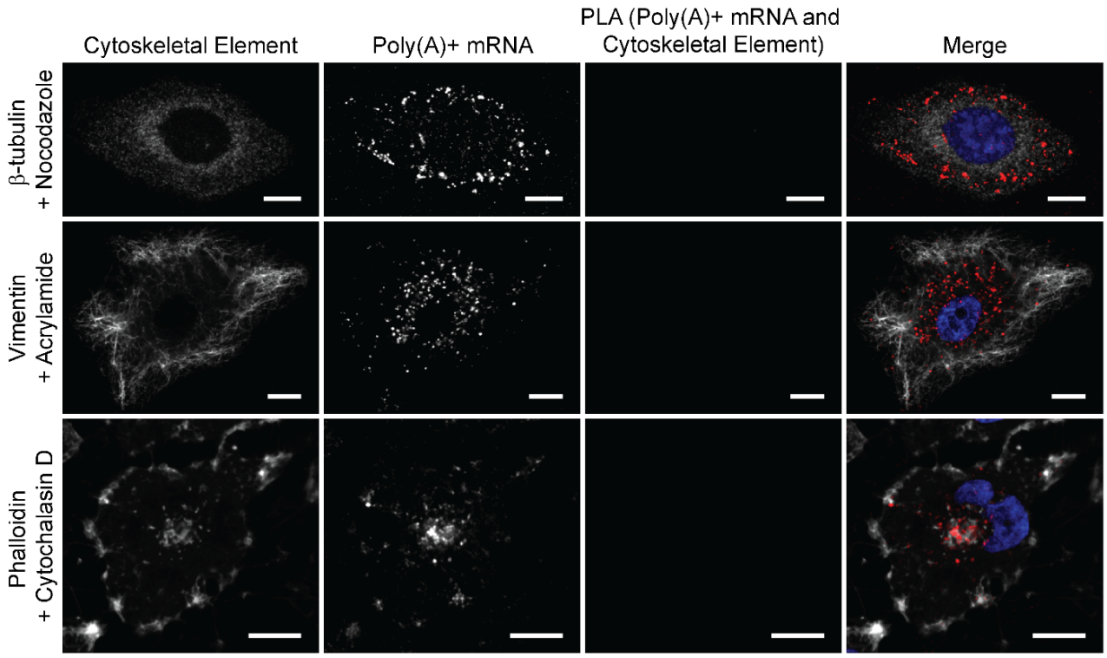

Figure 3.5: Interactions between *poly(A)*+ mRNA and cytoskeletal elements in A549 cells post-depolymerization of microtubules using nocodazole, intermediate filaments using acrylamide, and actin using cytochalasin D. β-tubulin, vimentin, and phalloidin immunofluorescence (IF), *poly(A)*+ mRNA, and PLA between *poly(A)*+ mRNA and the cytoskeletal elements in HDF were imaged with a laser-scanning confocal microscope. Merged images of the cytoskeleton (white), *poly(A)*+ mRNA (red), PLA (green) and nuclei (blue) are shown. Single image plane is represented. Scale bar, 10 µm. (Jung, Lifland et al. 2013)

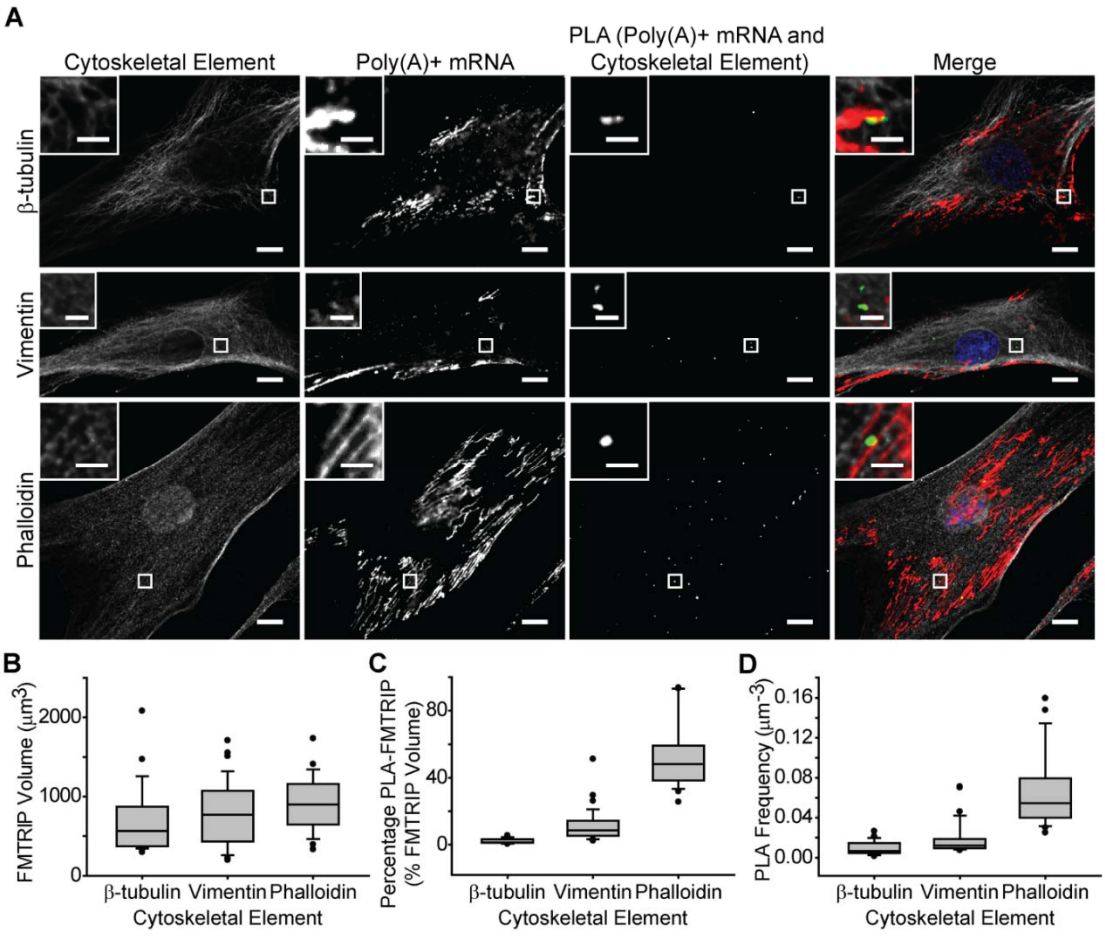

Figure 3.6: Interactions between *poly(A)*+ mRNA and cytoskeletal elements in HDF. (A) β-tubulin, vimentin and phalloidin IF, *poly(A)*+ mRNA, and PLA between *poly(A)*+ mRNA and the cytoskeletal elements in HDF were imaged with a laser-scanning confocal microscope. Merged images of the cytoskeleton (white), *poly(A)*+ mRNA (red), PLA (green) and nuclei (blue) are shown. Single image plane is represented. Inset, images of boxed regions. Scale bar, 10 μm (2 μm in insets). (B) The mean FMTRIP volume was similar (Kruskal-Wallis One Way ANOVA on Ranks, p=0.5) in cells, where the interactions between *poly(A)*+ mRNA and β-tubulin (n=25, mean=706μm^3, s.d.=427μm^3), vimentin (n=33, mean=780μm^3, s.d.=405μm^3), or phalloidin (n=23, mean=916μm^3, s.d.=346μm^3) were quantified. (C) The mean percentage of FMTRIP colocalized with PLA (PLA-FMTRIP) was significantly different between interactions of *poly(A)*+ mRNA with β-tubulin (n=25, mean=2.3%, s.d.=1.5%), vimentin (n=33, mean=11.5%, s.d.=9.7%), and phalloidin (n=23, mean=53.7%, s.d.=19.9%). (**Table 3.1**) (D) The mean PLA frequency was significantly different between the interactions of *poly(A)*+ mRNA with β-tubulin (n=25, mean=0.010μm^{-3}, s.d.=0.007μm^{-3}), vimentin (n=33, mean=0.019μm^{-3}, s.d.=0.016μm^{-3}), or phalloidin (n=23, mean=0.069μm^{-3}, s.d.=0.039μm^{-3}). (**Table 3.2**) Error bars, s.d. (Jung, Lifland et al. 2013)

Table 3.1: Comparisons of the mean percentage of FMTRIP colocalized with PLA (PLA-FMTRIP) in human dermal fibroblasts (HDF). Interactions between *poly(A)+* mRNA and β-tubulin (n=25, mean=2.3%, SD=1.5%), vimentin (n=33, mean=11.5%, SD=9.7%), or phalloidin (n=23, mean=53.7%, SD=19.9%) were compared using Kruskal-Wallis one-way ANOVA on ranks with Dunn's method for multiple comparison ($p < 0.001$). (Jung, Lifland et al. 2013)

Comparison	Diff of Ranks	Q	P<0.05
β-tubulin vs Vimentin	26.7	4.3	Yes
β-tubulin vs Phalloidin	54.8	8.0	Yes
Vimentin vs Phalloidin	28.1	4.4	Yes

Table 3.2: Comparisons of the mean PLA frequency in HDF. Interactions between *poly(A)+* mRNA and β-tubulin (n=25, mean=0.010μm^{-3}, s.d.=0.007μm^{-3}), vimentin (n=33, mean=0.019μm^{-3}, s.d.=0.016μm^{-3}), or phalloidin (n=23, mean=0.069μm^{-3}, s.d.=0.039μm^{-3}) were compared using Kruskal-Wallis one-way ANOVA on ranks with Dunn's method for multiple comparison ($p < 0.001$). (Jung, Lifland et al. 2013)

Comparison	Diff of Ranks	Q	P<0.05
β-tubulin vs Vimentin	15.1	2.4	Yes
β-tubulin vs Phalloidin	45.9	6.8	Yes
Vimentin vs Phalloidin	30.8	4.8	Yes

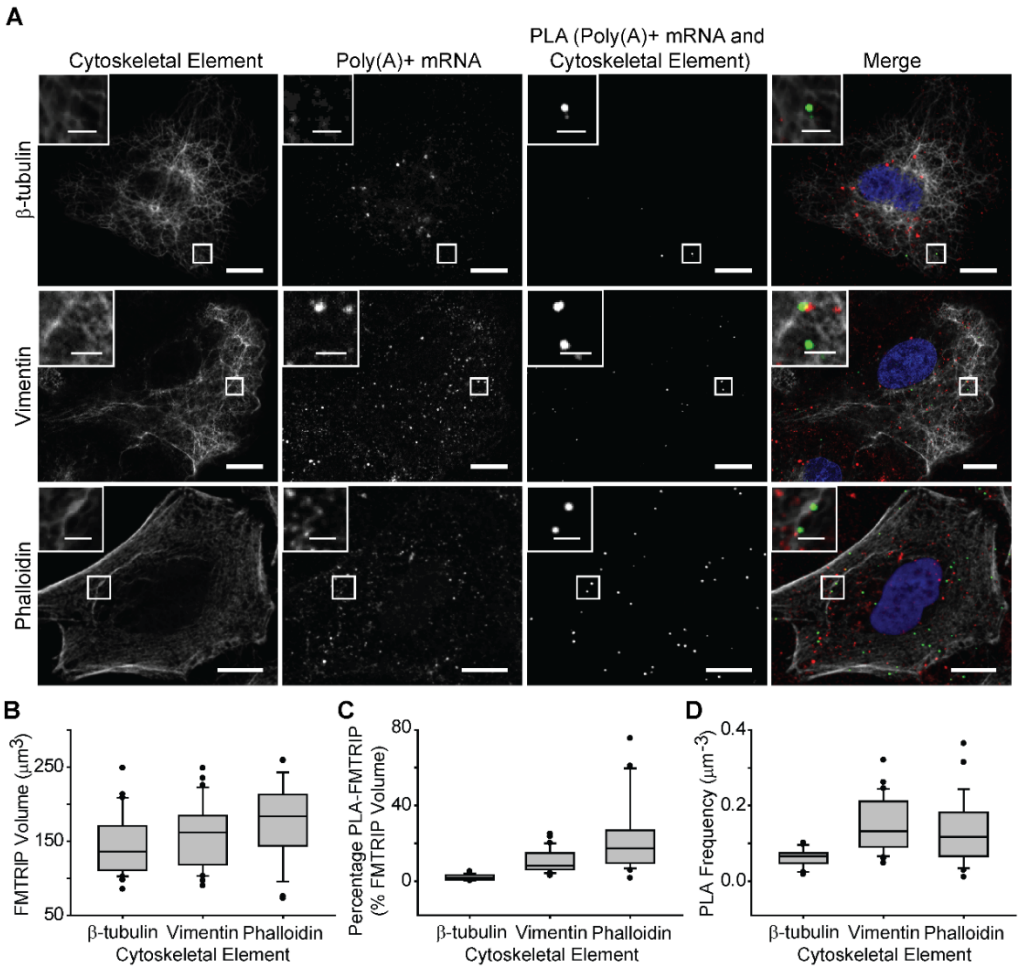

Figure 3.7: Interactions between *poly(A)*+ mRNA and cytoskeletal elements in A549 cells. (A) β-tubulin, vimentin and phalloidin IF, *poly(A)*+ mRNA, and PLA between *poly(A)*+ mRNA and the cytoskeletal elements in A549 cells were imaged with a laser-scanning confocal microscope. Merged images of the cytoskeleton (white), *poly(A)*+ mRNA (red), PLA (green) and nuclei (blue) are shown. Single image plane is represented. Inset, images of boxed regions. Scale bar, 10 μm (2 μm in insets). (B) The mean FMTRIP volume was similar (One Way ANOVA with normal distribution, p=0.7) in cells, where the interactions between *poly(A)*+ mRNA and β-tubulin (n=26, mean=146μm^3, s.d.=42μm^3), vimentin (n=28, mean=160μm^3, s.d.=43μm^3), or phalloidin (n=24, mean=177μm^3, s.d.=51μm^3) were quantified. (C) The mean percentage of FMTRIP colocalized with PLA (PLA-FMTRIP) was different between the interactions of *poly(A)*+ mRNA with β-tubulin (n=26, mean=2.1%, s.d.=1.4%), vimentin (n=28, mean=10.5%, s.d.=6.1%), and phalloidin (n=24, mean=22.9%, s.d.=18.6%). (**Table 3.3**) (D) The mean PLA frequency was significantly different between the interactions of *poly(A)*+ mRNA with β-tubulin (n=26, mean=0.063μm^{-3}, s.d.=0.023μm^{-3}), vimentin (n=28, mean=0.15μm^{-3}, s.d.=0.07μm^{-3}), or phalloidin (n=24, mean=0.13μm^{-3}, s.d.=0.09μm^{-3}). (**Table 3.4**) Error bars, s.d. (Jung, Lifland et al. 2013)

Table 3.3: Comparisons of the mean percentage of FMTRIP colocalized with PLA (PLA-FMTRIP) in A549 cells. Interactions between *poly(A)*+ mRNA and β-tubulin (n=26, mean=2.1%, s.d.=1.4%), vimentin (n=28, mean=10.5%, s.d.=6.1%), or phalloidin (n=24, mean=22.9%, s.d.=18.6%) were compared using Kruskal-Wallis one-way ANOVA on ranks with Dunn's method for multiple comparison ($p < 0.001$). (Jung, Lifland et al. 2013)

Comparison	Diff of Ranks	Q	P<0.05
β-tubulin vs Vimentin	30.8	5.0	Yes
β-tubulin vs Phalloidin	44.6	7.0	Yes
Vimentin vs Phalloidin	13.8	2.2	No

Table 3.4: Comparisons of the mean PLA frequency in A549 cells. Interactions between *poly(A)*+ mRNA and β-tubulin (n=26, mean=0.063μm^{-3}, s.d.=0.023μm^{-3}), vimentin (n=28, mean=0.15μm^{-3}, s.d.=0.07μm^{-3}), or phalloidin (n=24, mean=0.13μm^{-3}, s.d.=0.09μm^{-3}) were compared using Kruskal-Wallis one-way ANOVA on ranks with Dunn's method for multiple comparison ($p < 0.001$). (Jung, Lifland et al. 2013)

Comparison	Diff of Ranks	Q	P<0.05
β-tubulin vs Vimentin	29.1	4.7	Yes
β-tubulin vs Phalloidin	21.4	3.3	Yes
Vimentin vs Phalloidin	7.8	1.2	No

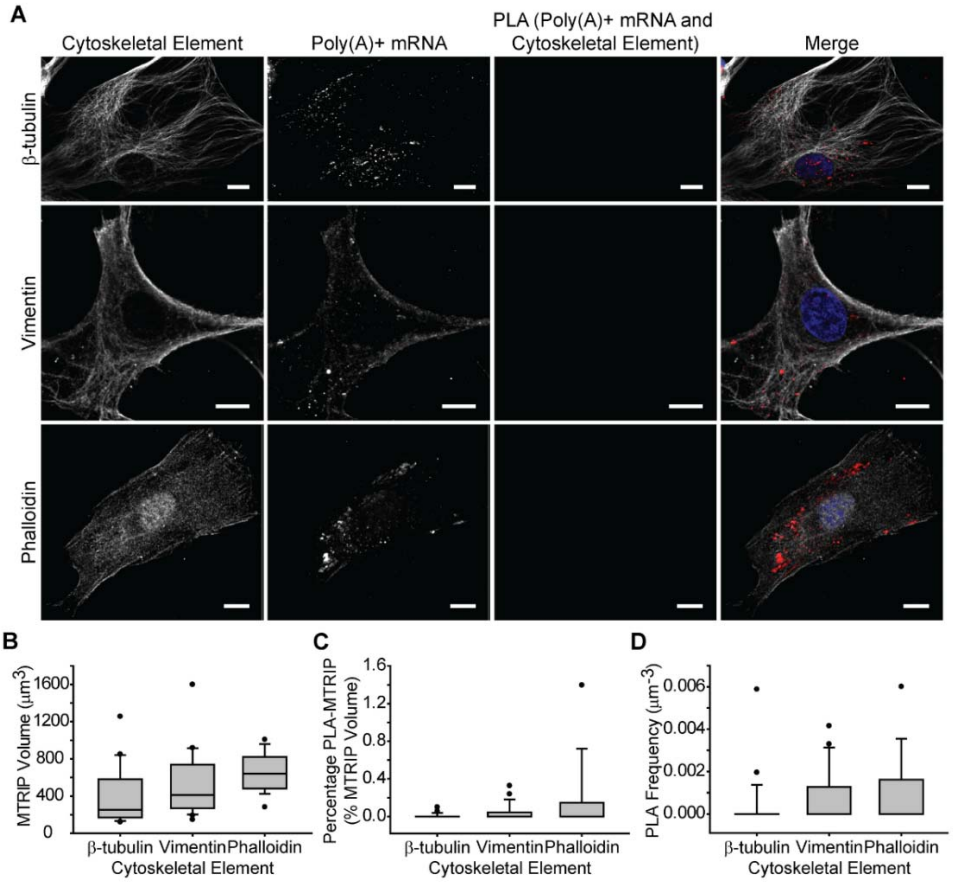

Figure 3.8: Interactions between *poly(A)*+ mRNA bound to MTRIP lacking flag tag and cytoskeletal elements in human dermal fibroblasts (HDF). (A) β-tubulin, vimentin and phalloidin IF, *poly(A)*+ mRNA, and PLA between *poly(A)*+ mRNA, and the cytoskeletal elements in HDF were imaged with a laser-scanning confocal microscope. Merged images of the cytoskeleton (white), poly(A)+ mRNA (red), PLA (green), and nuclei (blue) are shown. Single image plane is represented. Scale bar, 10 μm. (B) The mean MTRIP volume was similar (Kruskal-Wallis One Way ANOVA on Ranks, p=0.08) in cells, where the interactions between *β-actin* mRNA and β-tubulin (n=18, mean=404μm^3, s.d.=317μm^3), vimentin (n=19, mean=518μm^3, s.d.=362μm^3), or phalloidin (n=15, mean=653μm^3, s.d.=211μm^3) were quantified. (C) The mean percentage of MTRIP colocalized with PLA (PLA-MTRIP) was similarly minimal (Kruskal-Wallis One Way ANOVA on Ranks, p=0.15) in β-tubulin (n=18, mean=0.01%, s.d.=0.03%), vimentin (n=19, mean=0.04%, s.d.=0.1%), or phalloidin (n=15, mean=0.20%, s.d.=0.41%). (D) The mean PLA frequency was also minimal (Kruskal-Wallis One Way ANOVA on Ranks, p=0.23) in β-tubulin (n=18, mean=0.0004μm^{-3}, s.d.=0.001μm^{-3}), vimentin (n=19, mean=0.0008μm^{-3}, s.d.=0.0001μm^{-3}), or phalloidin (n=15, mean=0.001μm^{-3}, s.d.=0.002μm^{-3}). Error bars, s.d. (Jung, Lifland et al. 2013)

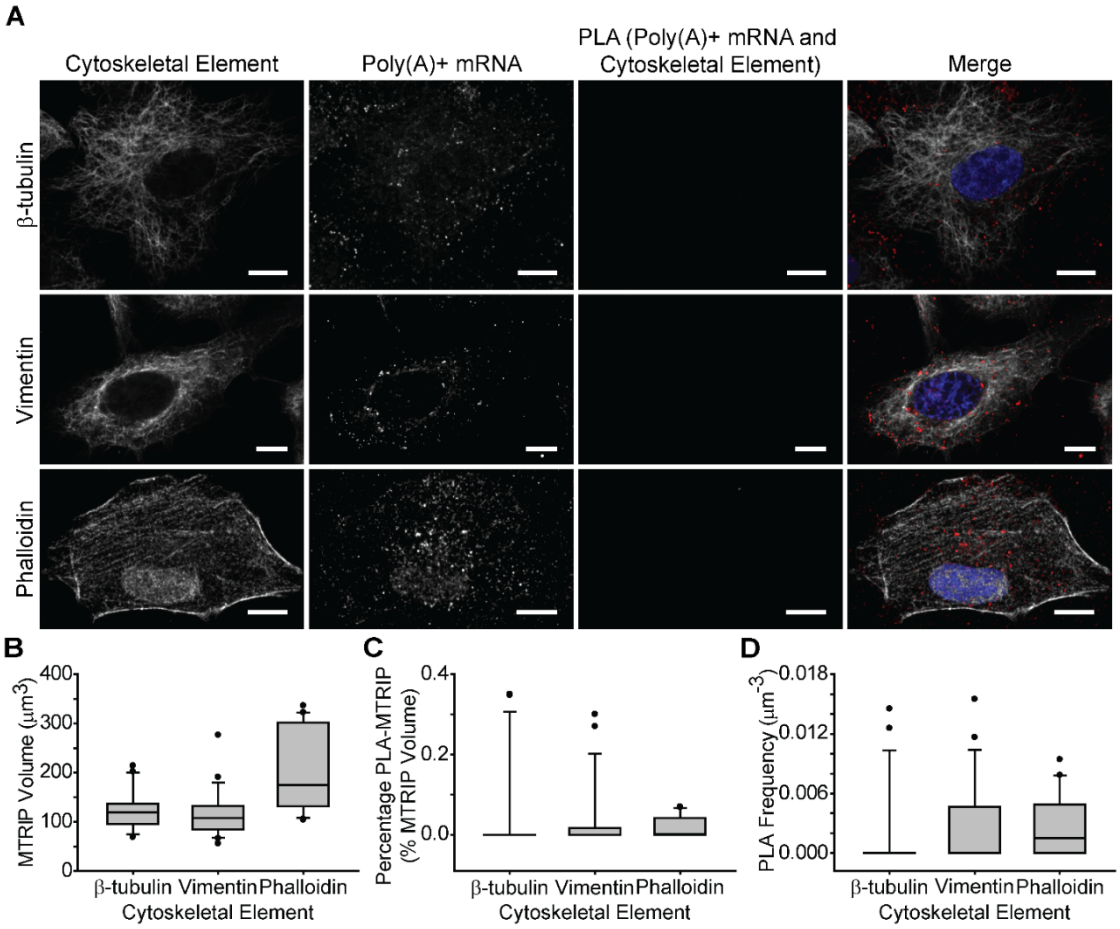

Figure 3.9: Interactions between *poly(A)+* mRNA bound to MTRIP lacking flag tag and cytoskeletal elements in A549 cells. (A) β-tubulin, vimentin and phalloidin IF, *poly(A)+* mRNA, and PLA between *poly(A)+* mRNA and the cytoskeletal elements in HDF were imaged with a laser-scanning confocal microscope. Merged images of the cytoskeleton (white), *poly(A)+* mRNA (red), PLA (green) and nuclei (blue) are shown. Single image plane is represented. Scale bar, 10 μm. (B) The mean MTRIP volume was similar (Kruskal-Wallis One Way ANOVA on Ranks, p=0.08) in cells, where the interactions between *β-actin* mRNA and β-tubulin (n=18, mean=404μm^3, s.d.=317μm^3), vimentin (n=19, mean=518μm^3, s.d.=362μm^3), or phalloidin (n=15, mean=653μm^3, s.d.=211μm^3) were quantified. (C) The mean percentage of MTRIP colocalized with PLA (PLA-MTRIP) was similarly minimal (Kruskal-Wallis One Way ANOVA on Ranks, p=0.15) in β-tubulin (n=18, mean=0.01%, s.d.=0.03%), vimentin (n=19, mean=0.04%, s.d.=0.1%), or phalloidin (n=15, mean=0.20%, s.d.=0.41%). (D) The mean PLA frequency was also minimal (Kruskal-Wallis One Way ANOVA on Ranks, p=0.23) in β-tubulin (n=18, mean=0.0004μm^{-3}, s.d.=0.001μm^{-3}), vimentin (n=19, mean=0.0008μm^{-3}, s.d.=0.0001μm^{-3}), or phalloidin (n=15, mean=0.001μm^{-3}, s.d.=0.002μm^{-3}). Error bars, s.d. (Jung, Lifland et al. 2013)

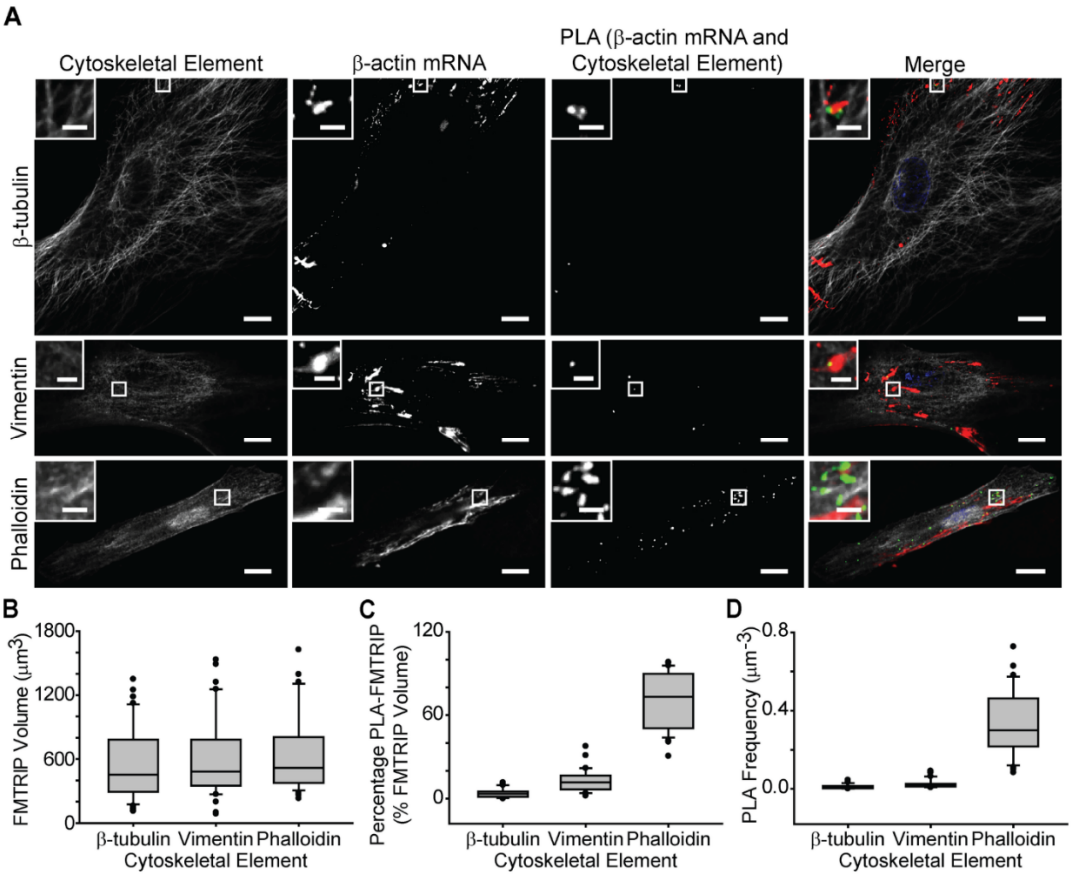

Figure 3.10: Interactions between *β-actin* mRNA and cytoskeletal elements in HDF. (A) β-tubulin, vimentin and phalloidin IF, β-actin mRNA, and PLA between *β-actin* mRNA and the cytoskeletal elements in HDF were imaged with a laser-scanning confocal microscope. Merged images of the cytoskeleton (white), β-actin mRNA (red), PLA (green), and nuclei (blue) are shown. Single image plane is represented. Inset, images of boxed regions. Scale bar, 10 μm (2 μm in insets). (B) The mean FMTRIP volume was similar (Kruskal-Wallis One Way ANOVA on Ranks, p=0.5) in cells, where the interactions between *β-actin* mRNA and β-tubulin (n=40, mean=567μm^3, s.d.=355μm^3), vimentin (n=36, mean=607μm^3, s.d.=385μm^3), or phalloidin (n=30, mean=660μm^3, s.d.=389μm^3) were quantified. (C) The mean percentage of FMTRIP colocalized with PLA (PLA-FMTRIP) was significantly different (**Table 3.5**) between the interactions of *β-actin* mRNA with β-tubulin (n=40, mean=3.9%, s.d.=3.2%), vimentin (n=36, mean=12.7%, s.d.=7.9%), or phalloidin (n=30, mean=71.5%, s.d.=20.1%). (D) The mean PLA frequency was significantly different (**Table 3.6**) between the interactions of *β-actin* mRNA with β-tubulin (n=40, mean=0.012μm^{-3}, s.d.=0.011μm^{-3}), vimentin (n=36, mean=0.027μm^{-3}, s.d.=0.023μm^{-3}), or phalloidin (n=30, mean=0.33μm^{-3}, s.d.=0.17μm^{-3}). Error bars, s.d. (Jung, Lifland et al. 2013)

Table 3.5: Comparisons of the mean percentage of FMTRIP colocalized with PLA (PLA-FMTRIP) in HDF. Interactions between *β-actin* mRNA and β-tubulin (n=40, mean=3.9%, s.d.=3.2%), vimentin (n=36, mean=12.7%, s.d.=7.9%), or phalloidin (n=30, mean=71.5%, s.d.=20.1%) were compared using Kruskal-Wallis one-way ANOVA on ranks with Dunn's method for multiple comparison ($p < 0.001$). (Jung, Lifland et al. 2013)

Comparison	Diff of Ranks	Q	P<0.05
β-tubulin vs Vimentin	29.4	4.2	Yes
β-tubulin vs Phalloidin	66.8	9.0	Yes
Vimentin vs Phalloidin	37.4	4.9	Yes

Table 3.6: Comparisons of the mean PLA frequency in HDF. Interactions between *β-actin* mRNA and β-tubulin (n=40, mean=0.012μm^{-3}, s.d.=0.011μm^{-3}), vimentin (n=36, mean=0.027μm^{-3}, s.d.=0.023μm^{-3}), or phalloidin (n=30, mean=0.33μm^{-3}, s.d.=0.17μm^{-3}) were compared using Kruskal -Wallis one-way ANOVA on ranks with Dunn's method for multiple comparison ($p < 0.001$). (Jung, Lifland et al. 2013)

Comparison	Diff of Ranks	Q	P<0.05
β-tubulin vs Vimentin	20.9	3.0	Yes
β-tubulin vs Phalloidin	62.8	8.5	Yes
Vimentin vs Phalloidin	41.9	5.5	Yes

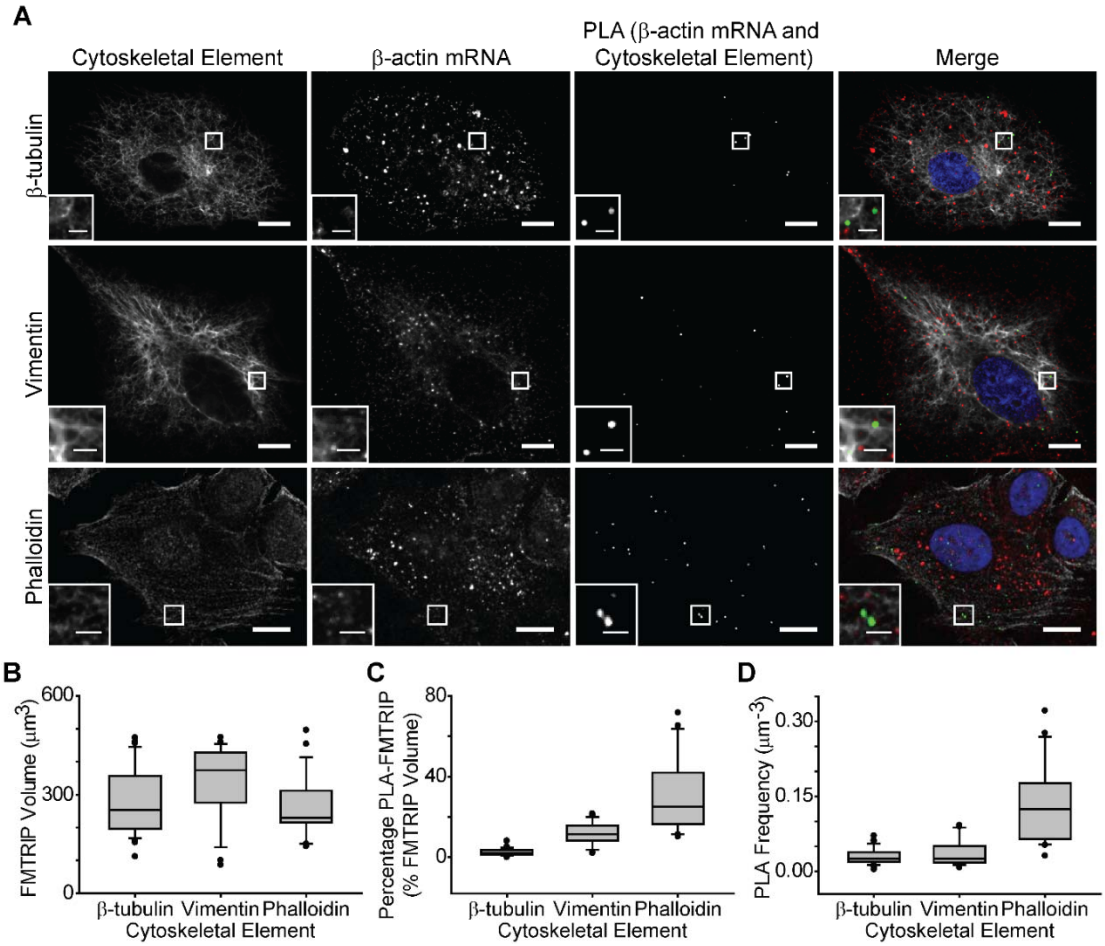

Figure 3.11: Interactions between *β-actin* mRNA and cytoskeletal elements in A549 cells. (A) β-tubulin, vimentin and phalloidin IF, *β-actin* mRNA, and PLA between *β-actin* mRNA and the cytoskeletal elements in A549 cells were imaged with a laser-scanning confocal microscope. Merged images of the cytoskeleton (white), *β-actin* mRNA (red), PLA (green) and nuclei (blue) are shown. Single image plane is represented. Inset, images of boxed regions. Scale bar, 10 μm (2 μm in insets). (B) The mean FMTRIP volume was similar (One Way ANOVA with normal distribution, p=0.08) in cells, where the interactions between *β-actin* mRNA and β-tubulin (n=31, mean=281μm^3, s.d.=104μm^3), vimentin (n=19, mean=336μm^3, s.d.=114μm^3), or phalloidin (n=20, mean=263μm^3, s.d.=96μm^3) were quantified. (C) The mean percentage of FMTRIP colocalized with PLA (PLA-FMTRIP) was significantly different (**Table 3.7**) between the interactions of *β-actin* mRNA with β-tubulin (n=31, mean=2.6%, s.d.=1.7%), vimentin (n=19, mean=11.8%, s.d.=5.7%), or phalloidin (n=20, mean=31.3%, s.d.=19.6%). (D) The mean PLA frequency for interactions between *β-actin* mRNA and phalloidin (n=20, mean=0.14μm^{-3}, s.d.=0.08μm^{-3}) was significantly greater (**Table 3.8**) than the interactions between *β-actin* mRNA and β-tubulin (n=31, mean=0.030μm^{-3}, s.d.=0.016μm^{-3}) or vimentin (n=19, mean=0.04μm^{-3}, s.d.=0.03μm^{-3}). Error bars, s.d. (Jung, Lifland et al. 2013)

Table 3.7: Comparisons of the mean percentage of FMTRIP colocalized with PLA (PLA-FMTRIP) in A549 cells. Interactions between *β-actin* mRNA and β-tubulin (n=31, mean=2.6%, s.d.=1.7%), vimentin (n=19, mean=11.8%, s.d.=5.7%), or phalloidin (n=20, mean=31.3%, s.d.=19.6%) were compared using Kruskal-Wallis one-way ANOVA on ranks with Dunn's method for multiple comparison ($p < 0.001$). (Jung, Lifland et al. 2013)

Comparison	Diff of Ranks	Q	P<0.05
β-tubulin vs Vimentin	25.0	4.2	Yes
β-tubulin vs Phalloidin	40.8	7.0	Yes
Vimentin vs Phalloidin	15.8	2.4	Yes

Table 3.8: Comparisons of the mean PLA frequency in A549 cells. Interactions between *β-actin* mRNA and β-tubulin (n=31, mean=0.030μm^{-3}, s.d.=0.016μm^{-3}), vimentin (n=19, mean=0.04μm^{-3}, s.d.=0.03μm^{-3}), or phalloidin (n=20, mean=0.14μm^{-3}, s.d.=0.08μm^{-3}) were compared using Kruskal-Wallis one-way ANOVA on ranks with Dunn's method for multiple comparison ($p < 0.001$). (Jung, Lifland et al. 2013)

Comparison	Diff of Ranks	Q	P<0.05
β-tubulin vs Vimentin	2.3	0.4	No
β-tubulin vs Phalloidin	31.7	5.4	Yes
Vimentin vs Phalloidin	29.4	4.5	Yes

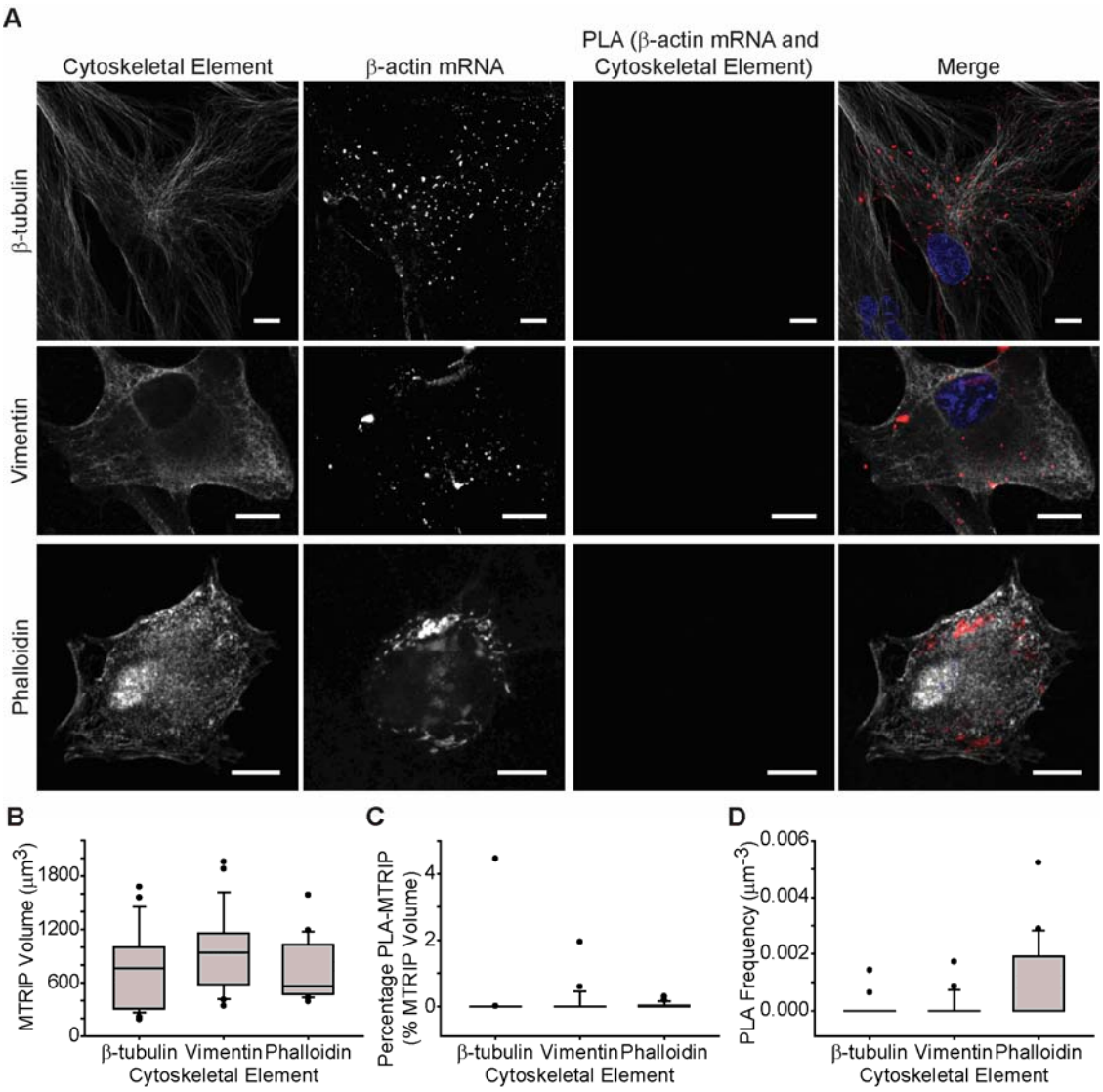

Figure 3.12: Interactions between *β-actin* mRNA bound to MTRIP lacking flag tags and cytoskeletal elements in human dermal fibroblasts (HDF). (A) β-tubulin, vimentin, and phalloidin IF, *β-actin* mRNA, and PLA between *β-actin* mRNA and the cytoskeletal elements in HDF were imaged with a laser-scanning confocal microscope. Merged images of the cytoskeleton (white), *β-actin* mRNA (red), PLA (green), and nuclei (blue) are shown. Single image plane is represented. Scale bar, 10μm. (B) The mean MTRIP volume was similar (Kruskal-Wallis One Way ANOVA on Ranks, p=0.12) in cells, where the interactions between *β-actin* mRNA and β-tubulin (n=25, mean=750μm^3, s.d.=460μm^3), vimentin (n=22, mean=980μm^3, s.d.=470μm^3), or phalloidin (n=17, mean=710μm^3, s.d.=340μm^3) were quantified. (C) The mean percentage of MTRIP colocalized with PLA (PLA-MTRIP) was similarly minimal (Kruskal-Wallis One Way ANOVA on Ranks, p>0.05) in β-tubulin (n=25, mean=0.2%, s.d.=0.9%), vimentin (n=22, mean=0.1%, s.d.=0.4%), or phalloidin (n=17, mean=0.04%,

s.d.=0.08%). (D) The mean PLA frequency was also minimal (Kruskal-Wallis One Way ANOVA on Ranks, $p>0.05$) in β-tubulin (n=25, mean=0.0001μm^{-3}, 0.0003μm^{-3}), vimentin (n=22, mean=0.0002μm^{-3}, 0.0004μm^{-3}), or phalloidin (n=17, mean=0.001μm^{-3}, 0.002μm^{-3}). Error bars, s.d. (Jung, Lifland et al. 2013)

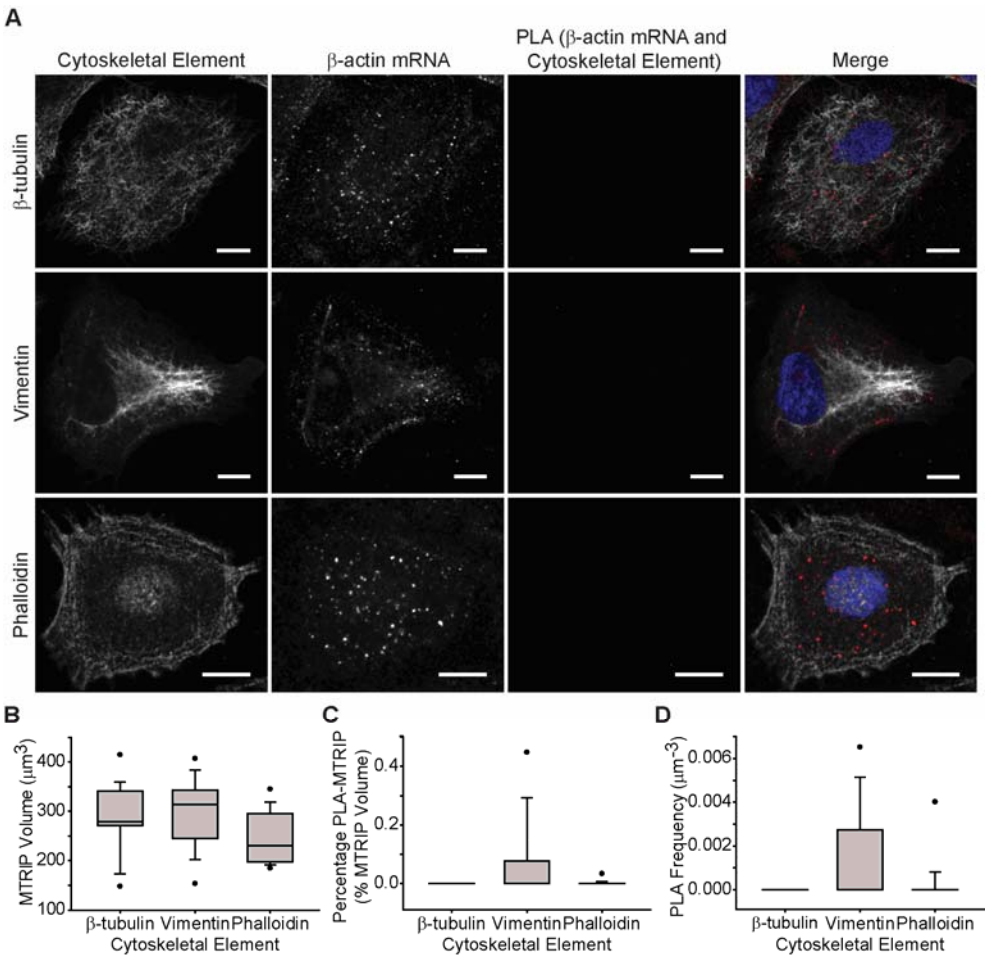

Figure 3.13: Interactions between *β-actin* mRNA bound to MTRIP lacking flag tags and cytoskeletal elements in A549 cells. (A) β-tubulin, vimentin, and phalloidin IF, *β-actin* mRNA, and PLA between *β-actin* mRNA and the cytoskeletal elements in A549 cells were imaged with a laser-scanning confocal microscope. Merged images of the cytoskeleton (white), *β-actin* mRNA (red), PLA (green), and nuclei (blue) are shown. Single image plane is represented. Scale bar, 10μm. (B) The mean MTRIP volume was similar (Kruskal-Wallis One Way ANOVA on Ranks, p=0.08) in cells, where the interactions between *β-actin* mRNA and β-tubulin (n=15, mean=289μm^3, s.d.=68μm^3), vimentin (n=11, mean=299μm^3, s.d.=71μm^3), or phalloidin (n=13, mean=243μm^3, s.d.=53μm^3) were quantified. (C) The mean percentage of MTRIP colocalized with PLA (PLA-MTRIP) was similarly minimal (Kruskal-Wallis One Way ANOVA on Ranks, p>0.05) in β-tubulin (n=15, mean=0.0%, s.d.=0.0%), vimentin (n=11, mean=0.07%, s.d.=0.14%), or phalloidin (n=13, mean=0.003%, s.d.=0.009%). (D) The mean PLA frequency was also minimal (Kruskal-Wallis One Way ANOVA on Ranks, p>0.05) in β-tubulin (n=15, mean=0.00μm^{-3}, s.d.=0.00μm^{-3}), vimentin (n=11, mean=0.001μm^{-3}, s.d.=0.002μm^{-3}), or phalloidin (n=13, mean=0.0003μm^{-3}, s.d.=0.0011μm^{-3}). Error bars, s.d. (Jung, Lifland et al. 2013)

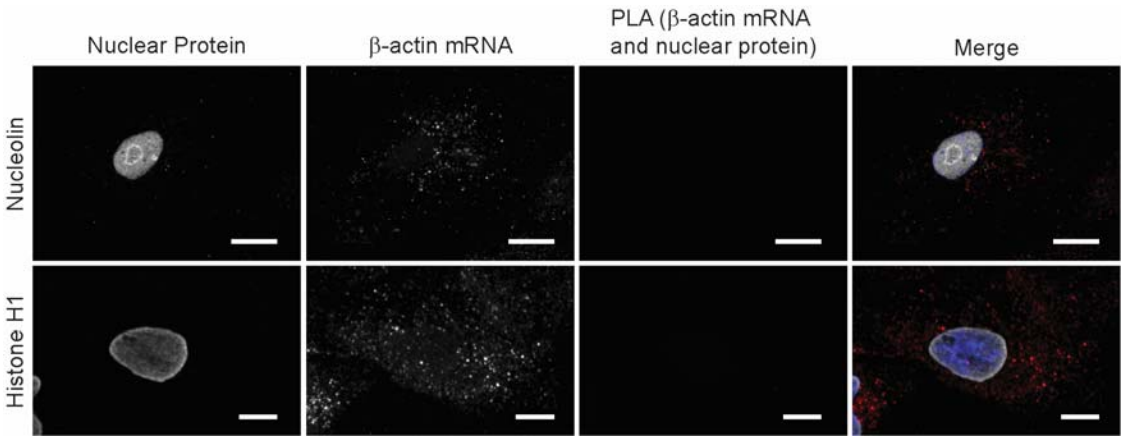

Figure 3.14: Interactions between *β-actin* mRNA and nuclear proteins in A549 cells. Nucleolin (C23) and Histone H1 IF, *β-actin* mRNA, and PLA between *β-actin* mRNA and the nuclear proteins in A549 cells were imaged with a laser-scanning confocal microscope. Merged images of the nuclear protein (white), *β-actin* mRNA (red), PLA (green), and nuclei (blue) are shown. All image planes are represented. Scale bar, 10μm. (Jung, Lifland et al. 2013)

Conclusion

In contrast to the 48 hours required to image and quantify interactions between *poly(A)+* mRNA and cytoskeleton in five to ten cells using EM (Bassell, Powers et al. 1994), using the combined FMTRIP and PLA method, this was achievable for two different mRNAs in 15-40 cells within eight hours using a widefield fluorescent microscope. Since single interactions lead to the production of single fluorescent puncta (Soderberg, Gullberg et al. 2006), mRNA-cytoskeleton interactions were easily identified and quantified on a per cell basis. With the mRNAs also hybridized to fluorescent probes that reflect their quantity (Zurla, Lifland et al. 2011; Jung, Lifland et al. 2013), the interactions were normalized by the mRNA signal, allowing quantification that can be compared between cells. Because probes were hybridized to the mRNA in live cells before fixation, they targeted mRNAs that were undistorted by fixatives. The ability to detect these interactions quantitatively using multiple fixatives post-probe delivery, allowed us to utilize the optimal fixative for each cytoskeletal element, ensuring accuracy; this was not possible with other methods.

In addition to these methodological advantages, our findings were consistent with the EM data (Bassell, Powers et al. 1994), both *poly(A)+* and *β-actin* mRNA were bound predominantly to actin, compared to microtubules and vimentin, in both A549 cells and HDF. In human diploid fibroblasts, Bassell et al. observed 72% *poly(A)+* mRNA was localized within 5nm of F-actin filaments (n=5); 29% with vimentin filaments (n=5); and less than 10% with microtubules (n=5) (Bassell, Powers et al. 1994). In human dermal fibroblasts, on average, we observed 54% *poly(A)+* mRNA interacting with F-actin (n=23); 12% with vimentin (n=33); and 2% with β-tubulin (n=25). For *β-actin* mRNA,

72% interacted with F-actin (n=30), 13% with vimentin (n=36), and 4% with β-tubulin (n=40).

The lower mean percentage of *poly(A)+* mRNA interaction using PLA compared to EM is likely because we under-labeled mRNA. Instead of using 90nM probes that produces the maximum intensity (Santangelo, Lifland et al. 2009; Lifland, Zurla et al. 2011), 60nM concentrations of probes were delivered in order to label a random portion of the mRNA population and to facilitate the imaging of individual mRNA granules and quantification of relative differences in their interactions with the cytoskeleton. In addition, the PLA reaction depends on the antibodies bound to the cytoskeleton and FMTRIP. Antibody concentrations that were less than that for maximal coverage were utilized, in order to sample a random portion of the protein population and to limit the detection of non-specific interactions. This is acceptable because the main purpose of using PLA for detection mRNA-protein interactions is to quantify and compare the relative change in the interactions, rather than to determine the absolute number of interactions. Slight differences between the EM data and our findings might be due to our larger sample size, methodological differences in data acquisition and analysis, and differences in the cell types used.

This work supports the idea that mRNAs are bound predominantly to actin, compared to microtubules and vimentin. mRNAs are likely anchored to actin (Condeelis and Singer 2005) and transported to specific areas in the cell by microtubules associated with motors (Lifland, Zurla et al. 2011). Similar to actin, vimentin likely serves to anchor the mRNA rather than to direct its motion. Vimentin depolymerization dramatically changed the mRNA localization for both mRNAs in both cell types, similar to actin

depolymerization. Contrastingly, microtubule depolymerization had little effect on the mRNA distribution.

On average, a greater percentage of mRNA was bound to F-actin in the HDFs compared to A549 cells, even though the percentage of mRNA bound to β-tubulin and vimentin was similar in both cell types. During epithelial to mesenchymal transition (EMT) in various cell types, translation of actin and vimentin increases along with actin rearrangement (Kalluri and Neilson 2003). One hypothesis may be that since A549 cells are an adenocarcinoma cell line and likely exhibit increased mesenchymal characteristics than normal epithelial cells, such as greater production of vimentin and actin (Mathias and Simpson 2009; Oyanagi, Ogawa et al. 2012). Still, since EMT can be induced in A549 cells using TGF-β (Pirozzi, Tirino et al. 2011), they likely express less actin than fibroblasts, which explains less F-actin interactions than HDFs. Additionally, considering their smaller size compared to the HDF, mRNA localization away from the nucleus and actin-anchoring may not be as crucial as in the HDF.

Using PLA, we detected changes in the *poly(A)*+ mRNA interactions with the cytoskeleton after F-actin depolymerization and arsenite-induced oxidative stress. We observed increased *poly(A)*+ mRNA binding to β-tubulin after F-actin depolymerization. Consistently, exposure to arsenite resulted in decreased *poly(A)*+ mRNA binding to F-actin and increased binding to β-tubulin within the first ten minutes. Interestingly, in both cytoD and arsenite exposure experiments, a complementary relationship between F-actin and β-tubulin was observed. When the mRNA granules separated from F-actin, their binding to microtubules increased. To date, a dynamic relationship between mRNA and

cytoskeletal components has not been reported. The mechanism for the similarity of these responses is unknown. Similar to cytoD, arsenite also disrupts actin filament formation (Chou 1989; Li and Chou 1992), but in a less direct and intense manner. With the arsenite exposure, mRNAs do not fall off of the F-actin, as with cytoD exposure, instead they may be moved onto microtubules predominantly and intermediate filaments to a lesser degree. This implies that the dynamic relationship between mRNA localization to F-actin and microtubules is likely a conserved response in both cytoD and arsenite exposure experiments, and not specific to F-actin depolymerization. The mechanism of this event will be explored in future publications.

In addition, these observations elicit a number of questions regarding mRNA control. The trans-acting factors controlling the mRNA localization to F-actin versus microtubules remain to be identified. The significance of mRNA binding to cytoskeleton in directing its function and fate toward translation or degradation also needs to be elucidated. Are the mRNAs switching from F-actin to microtubules so that they can be degraded? Or are they simply binding to microtubules randomly, because they are no longer bound to F-actin? Future studies, using the method discussed in this paper in conjunction with other methods, such as crosslinking and immunoprecipitation, should allow us to answer these questions.

Here, we present a powerful tool for imaging and quantifying mRNA-cytoskeleton interactions. It has shown to provide similar accuracy as EM but is easier to perform and is less labor-intensive. Unlike other methods, this technique can quantify the spatiotemporal asymmetry within an individual and population of cells as well as cell-to-

cell variations, which are valuable in numerous studies, such as viral infection (Heinlein, Epel et al. 1995; Bukrinskaya, Brichacek et al. 1998; Nemerow and Stewart 1999), stem cell differentiation (Suon, Jin et al. 2004; Ratti, Fallini et al. 2006; Hailesellasse Sene, Porter et al. 2007), and cancer pathophysiology (Zimber, Nguyen et al. 2004; Escuin, Kline et al. 2005; Greijer, van der Groep et al. 2005). This method, in future studies, will assist in improving our understanding of the effects of intracellular and extracellular signaling events on mRNA trafficking, localization, and translation via alterations in the interactions between the mRNA, RBPs, motor proteins, and cytoskeleton. Multiplexing this assay to detect multiple RNA-cytoskeleton and RNA-RBP interactions, simultaneously, will provide a more complete understanding of how these interactions are altered during infections, oxidative stress, or during the application of external forces. By combining this method with other assays, such as immunoprecipitation, that can identify RBPs that regulate mRNA-cytoskeleton interactions, we can elucidate the underlying mechanism that direct mRNA localization.

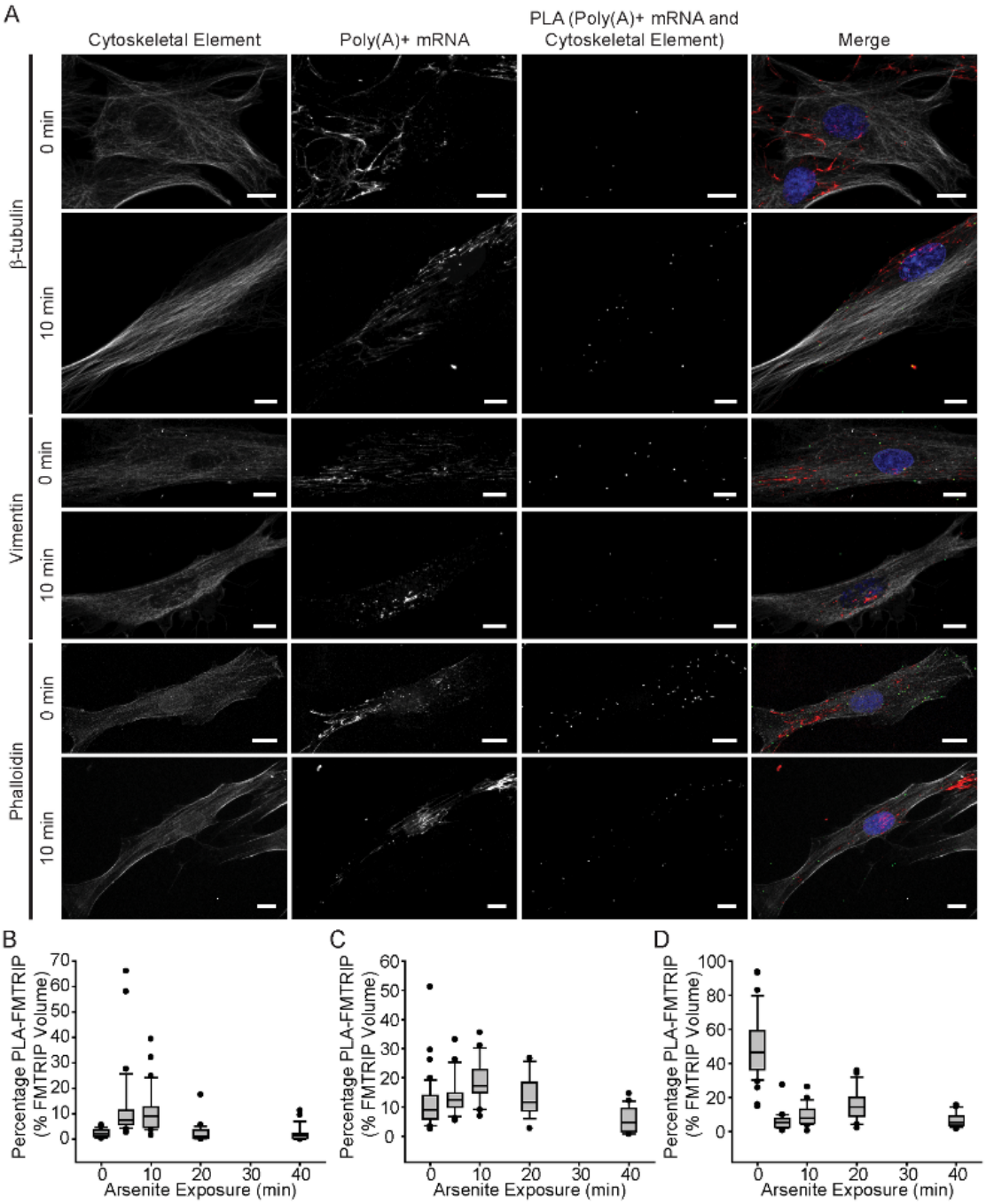

Figure 3.15: Arsenite-induced oxidative stress reduced *poly(A)*+ mRNA binding to F-actin and vimentin, while increasing interactions with β-tubulin. (A) β-tubulin, vimentin and phalloidin IF, *poly(A)*+ mRNA, and PLA between *poly(A)*+ mRNA and the cytoskeletal elements in HDF were imaged at 0 min (or no) and 10 min exposure to arsenite with a laser-scanning confocal microscope. Merged images of the cytoskeleton (white), *poly(A)*+ mRNA (red), PLA (green), and nuclei (blue) are shown. All image planes are represented. Scale bar, 10 µm. (B) The mean percentage of FMTRIP (PLA-

FMTRIP) bound to β-tubulin increased significantly from 0 min exposure (n=28, mean=2.5%, s.d.=1.6%) to 5 min exposure (Kruskal-Wallis One Way ANOVA on Ranks, $p<0.001$; n=31, mean=12.8%,s.d.=14.6%); remained high for 10 min exposure (n=26, mean=11.3%, s.d.=9.1%); and decreased to the pre-exposure level at 20 (Kruskal-Wallis One Way ANOVA on Ranks, $p<0.05$; n=22, mean=2.6%, s.d.=3.8%) and 40 min (n=20, mean=2.2%, s.d.=3.0%) (**Table 3.9**). (C) The mean percentage of FMTRIP (PLA-FMTRIP) bound to vimentin remained similar to 0 min exposure (n=42, mean=11.1%, s.d.=8.8%) for 5 (n=23, mean=13.9%,s.d.=6.5%),10 (n=19, mean=18.7%, s.d.=7.5%), and 20 min (n=13, mean=13.3%, s.d.=7.1%) exposure; it decreased at 40 min (n=17, mean=5.9%, s.d.=4.4%) (**Table 3.10**). (D) The mean percentage of FMTRIP (PLA-FMTRIP) bound to F-actin decreased significantly from 0 min exposure (n=38, mean=49.3%, s.d.=19.4%) to 5 min exposure (Kruskal-Wallis One Way ANOVA on Ranks, $p<0.001$; n=25, mean=6.0%,s.d.=5.2%); remained low for 10 (n=21, mean=9.6%, s.d.=6.4%), 20 (n=19, mean=15.4%, s.d.=9.4%), and 40 min (n=16, mean=6.8%, s.d.=4.4%) exposure (**Table 3.11)**. Error bars, s.d. (Jung, Lifland et al. 2013)

Table 3.9: Comparisons of the mean percentage of FMTRIP colocalized with PLA (PLA-FMTRIP) for *poly(A)*+ mRNA interactions with β-tubulin in HDF cells exposed to arsenite. At 0 (n=28, mean=2.5%, s.d.=1.6%), 5 (n=31, mean=12.8%,s.d.=14.6%), 10 (n=26, mean=11.3%, s.d.=9.1%), 20 (n=22, mean=2.6%, s.d.=3.8%), and 40 min (n=20, mean=2.2%, s.d.=3.0%), PLA-FMTRIP were compared using Kruskal-Wallis one-way ANOVA on ranks with Dunn's method for multiple comparison ($p<0.001$). (Jung, Lifland et al. 2013)

Comparison	Diff of Ranks	Q	P<0.05
0 min vs 5 min	49.2	5.1	Yes
0 min vs 10 min	48.3	4.8	Yes
0 min vs 20 min	7.5	0.7	No
0 min vs 40 min	9.3	0.9	No
5 min vs 10 min	0.9	0.09	No
5 min vs 20 min	56.7	5.5	Yes
5 min vs 40 min	58.5	5.5	Yes
10 min vs 20 min	55.9	5.2	Yes
10 min vs 40 min	57.6	5.3	Yes
20 min vs 40 min	1.8	0.2	No

Table 3.10: Comparisons of the mean percentage of FMTRIP colocalized with PLA (PLA-FMTRIP) for *poly(A)*+ mRNA interactions with vimentin in HDF cells exposed to arsenite. At 0 (n=42, mean=11.1%, s.d.=8.8%), 5 (n=23, mean=13.9%,s.d.=6.5%), 10 (n=19, mean=18.7%, s.d.=7.5%), 20 (n=13, mean=13.3%, s.d.=7.1%), and 40 min (n=17, mean=5.9%, s.d.=4.4%), PLA-FMTRIP were compared using Kruskal-Wallis one-way ANOVA on ranks with Dunn's method for multiple comparison ($p<0.001$). (Jung, Lifland et al. 2013)

Comparison	Diff of Ranks	Q	P<0.05
0 min vs 5 min	18.5	2.1	No
0 min vs 10 min	48.3	4.8	Yes
0 min vs 20 min	14.4	1.4	No
0 min vs 40 min	22.0	2.3	No
5 min vs 10 min	18.4	1.8	No
5 min vs 20 min	4.0	0.4	No
5 min vs 40 min	40.4	3.8	Yes
10 min vs 20 min	22.4	1.9	No
10 min vs 40 min	58.8	5.3	Yes
20 min vs 40 min	36.4	3.0	Yes

Table 3.11: Comparisons of the mean percentage of FMTRIP colocalized with PLA (PLA-FMTRIP) for *poly(A)*+ mRNA interactions with F-actin in HDF cells exposed to arsenite. At 0 (n=38, mean=49.3%, s.d.=19.4%), 5 (n=25, mean=6.0%,s.d.=5.2%), 10 (n=21, mean=9.6%, s.d.=6.4%), 20 (n=19, mean=15.4%, s.d.=9.4%), and 40 min (n=16, mean=6.8%, s.d.=4.4%), PLA-FMTRIP were compared using Kruskal-Wallis one-way ANOVA on ranks with Dunn's method for multiple comparison ($p<0.001$). (Jung, Lifland et al. 2013)

Comparison	Diff of Ranks	Q	P<0.05
0 min vs 5 min	69.6	7.8	Yes
0 min vs 10 min	55.0	5.9	Yes
0 min vs 20 min	39.3	4.1	Yes
0 min vs 40 min	65.2	6.3	Yes
5 min vs 10 min	14.6	1.4	No
5 min vs 20 min	30.3	2.9	Yes
5 min vs 40 min	4.4	0.4	No
10 min vs 20 min	15.7	1.4	No
10 min vs 40 min	10.3	0.9	No
20 min vs 40 min	1.8	0.2	No

Materials and methods

Flag-tagged neutravidin was synthesized by first conjugating flag tag-hyNic (Solulink) to neutravidin (Thermo) modified with 4FB (Solulink) using the manufacturer's protocol. The concentration of flag tag-hyNic and 4FB-modified neutravidin were adjusted to produce a molar ratio of two flags per neutravidin. After flag labeling, FMTRIPs were assembled as previously described (Santangelo, Lifland et al. 2009). Briefly, 2′-O-methyl RNA-DNA oligonucleotide chimeras were designed with a 5′-biotin and dT-C6-NH2 internal modifications (Biosearch Technologies). Cy3B-NHS ester fluorophores (GE Healthcare) were conjugated to the oligonucleotide amine groups using the manufacturer's protocol. Free dye was removed using 3 kDa Amicon spin columns (Millipore). The purified, labeled oligonucleotides were then tetramerized by incubation for 1 h at RT with flag-tagged neutravidin at molar ratio of 5:1. Free ligands were removed using 30 kDa Amicon spin columns (Millipore). The FMTRIP targeting different mRNA sequences (**Table 3.12**) were assembled separately prior to delivery. Neutravidin lacking the flag tag was used to assemble MTRIPs for a negative control.

Primary human dermal fibroblasts (Lonza, Basel, Switzerland) and A549 lung carcinoma cells (ATCC CCL-185) were maintained in High Glucose DMEM (Lonza) with 10% FBS (Hyclone), 100 U/ml penicillin (Invitrogen), and 100 µg/ml streptomycin (Invitrogen). Cells were plated on No. 1.5 glass coverslips (Ted Pella) one day prior to infection, transfection or imaging.

For probe delivery, cells were washed in Dulbecco's Phosphate Buffered Saline (DPBS) without Ca^{2+} and Mg^{2+} (Lonza), and then incubated with 0.2 U/ml activated

streptolysin O (Sigma) in OptiMEM (Invitrogen) containing FMTRIP (60 nM poly(A) or 10 nM each of 5 β-actin-targeting probes) for 10 min at 37°C. Delivery media were replaced with growth media for 15 min to restore membrane integrity before fixation.

After probe delivery and recovery, cells were fixed with either methanol or 1% paraformaldehyde (Electron Microscopy Science) in PBS, unless noted otherwise, for 10 min; permeabilized using acetone for 2 min (post-methanol fixation) or 0.2% triton X-100 (Sigma) for 5 min (post-PFA fixation); and blocked for 45 min with a modified blocking solution, which consists of 0.5% Tween 20 (CalBioChem), 0.1% Triton X-100, 0.1% gelatin (Aurion), 2% donkey serum (VWR) and 1% bovine serum albumin (BSA) (EMD) in PBS. Cells were washed with PBS for 5 min. Then they were incubated for 30 min at 37°C in each of two primary antibodies (Ab) diluted in 0.25% gelatin, 0.5% Triton X-100, 0.5% donkey serum and 1% BSA in PBS, and then corresponding oligonucleotide-labeled PLA probes (Olink Bioscience) diluted in 0.05% Tween-20 in PBS. They were washed with Duolink wash solution (Olink Bioscience) after each Ab incubation. The ligation and RCA reactions (Olink Bioscience) were performed as instructed in the manufacturer's protocol. Then the cells were immunostained or DAPI-stained (Invitrogen) and mounted on slides using Prolong (Invitrogen).

Primary Ab were mouse monoclonal anti-flag (1:500 for IF, 1:1000 for PLA, Sigma), rabbit polyclonal anti-flag (1:500 for IF, 1:1000 for PLA, Sigma), mouse monoclonal anti-β-tubulin (1:100 for IF, 1:1000 for PLA, Developmental Studies Hybridoma Bank), rabbit polyclonal anti-α-tubulin (1:200 for IF, 1:1500 for PLA, Abcam), mouse monoclonal anti-vimentin (1:50 for IF, 1:1000 for PLA, Developmental Studies Hybridoma Bank), rabbit anti-alexa fluor 488 (1:100 for IF, 1:2000 for PLA,

Molecular Probes). Rabbit polyclonal anti-flag Ab was used with mouse anti-β-tubulin and mouse anti-vimentin Ab. Mouse monoclonal anti-flag Ab was used with rabbit anti-alexa fluor 488 Ab. Alexa fluor 488 Phalloidin (Molecular Probes) was used to stain actin fibers, which were then targeted with rabbit anti-alexa fluor 488 Ab for PLA. Goat polyclonal anti-nucleolin antibody (1:200 for IF, 1:500 for PLA, Santa Cruz) and mouse monoclonal anti-histone H1 antibody (1:200 for IF, 1:500 for PLA, Santa Cruz) were used as negative controls.

After probe delivery, cells were incubated for 90 min at 37°C in glucose free DMEM (Invitrogen) containing 1μM cytochalasin D (Sigma) for actin depolymerization, for 90 min with 4μM nocodazole (Sigma) for microtubule depolymerization, and for 4 hr with 6mM acrylamide (Sigma) for vimentin depolymerization (Sager 1989). For oxidative stress, cells were incubated for 5, 10, 20, and 40 min at 37°C in 0.5mM sodium arsenite. The cells were fixed after incubation.

Unless specified otherwise, all the images were taken using a laser scanning confocal microscope, Zeiss LSM 700 using a 63×, NA 1.4 Plan-Apochromat objective. Resolution was set to 1036 × 1036. Files were imported into Volocity and linearly contrast enhanced for display. Widefield images were taken on an Axiovert 200M microscope (Zeiss) with a 63× numerical aperture (NA) 1.4 Plan-Apochromat objective, and an ORCA-ER AG camera (Hamamatsu). The imaging was performed using the Volocity acquisition software (PerkinElmer). Image stacks were recorded at 200 nm intervals to adequately sample volumes for iterative deconvolution.

Widefield images were deconvolved using Volocity's deconvolution algorithms. Probe and PLA signal quantification were computed in Volocity and imported into Excel (Microsoft) or Sigma Plot (Systat) for further analysis and plotting. Images presented have been linearly contrast enhanced for clarity. All calculations were performed directly on raw, deconvolved widefield data.

The volume of RNA, volume of PLA-colocalized RNA, and PLA frequency/RNA volume were measured using Volocity. Each cell was analyzed individually as follows. Each cell was identified by cytoskeletal immunostaining. The RNA volume was determined based on the SD intensity. The PLA signal initially was identified as PLA objects by their SD intensity then separated into individual punctae using the "separate touching objects" tool. The objects were further filtered based on size and maximum intensity. The RNA volume colocalized with PLA signal was determined selecting the RNA volume with PLA fluorescence intensity greater than the minimum intensity or one SD intensity below the average intensity of the PLA objects detected in the cell, whichever value was greater. For each experiment, we analyzed at least 30 representative cells; experiments were repeated at least twice. In Sigma Plot, Kruskal-Wallis one-way ANOVA was used to compare the mean probe volume, the mean percentage of probe colocalized with PLA, and the mean PLA frequency. Multiple pairwise comparisons were performed with Dunn's method.

Table 3.12: *Poly(A)+* and *β-actin* mRNA targeting probe sequences and modifications. (Jung, Lifland et al. 2013)

Target	Ligand	Location within transcript
Poly(A)	5'-biotin-TXTTTT**UXUUUUUUXUUUUUUXUU**-3'	
β-actin 1	5'-biotin-TXTTTX**AXAGCACAGCCXGGAXA**-3'	494-478
β-actin 2	5'-biotin-TTTTTTX**AUUXCCCGCXCGGCCGXG**-3'	696-679
β-actin 3	5'-biotin-TXTTTTX**UCCUGXAACAAXGCAUCXC**-3'	1479-1461
β-actin 4	5'-biotin-TXTTTTX**AAGCCCXGGCXGCCXCCA**-3'	1748-1730
β-actin 5	5'-biotin-TXTTTT**GXCACCUXCACCGUXCCA G**-3'	1377-1359
	Boldface: 2'-O-Methyl RNA; X: dT-C6-NH_2; all others are DNA; underline: binding region	

References

Bassell, G. J., C. M. Powers, et al. (1994). "Single mRNAs visualized by ultrastructural in situ hybridization are principally localized at actin filament intersections in fibroblasts." J Cell Biol **126**(4): 863-876.

Bassell, G. J., H. Zhang, et al. (1998). "Sorting of beta-actin mRNA and protein to neurites and growth cones in culture." J Neurosci **18**(1): 251-265.

Beach, D. L., E. D. Salmon, et al. (1999). "Localization and anchoring of mRNA in budding yeast." Curr Biol **9**(11): 569-578.

Bertrand, E., P. Chartrand, et al. (1998). "Localization of ASH1 mRNA particles in living yeast." Mol Cell **2**(4): 437-445.

Bukrinskaya, A., B. Brichacek, et al. (1998). "Establishment of a functional human immunodeficiency virus type 1 (HIV-1) reverse transcription complex involves the cytoskeleton." J Exp Med **188**(11): 2113-2125.

Chen, C. Y., R. Gherzi, et al. (2001). "AU binding proteins recruit the exosome to degrade ARE-containing mRNAs." Cell **107**(4): 451-464.

Chou, I. N. (1989). "Distinct cytoskeletal injuries induced by As, Cd, Co, Cr, and Ni compounds." Biomed Environ Sci **2**(4): 358-365.

Condeelis, J. and R. H. Singer (2005). "How and why does beta-actin mRNA target?" Biol Cell **97**(1): 97-110.

Escuin, D., E. R. Kline, et al. (2005). "Both microtubule-stabilizing and microtubule-destabilizing drugs inhibit hypoxia-inducible factor-1alpha accumulation and activity by disrupting microtubule function." Cancer Res **65**(19): 9021-9028.

Glotzer, J. B., R. Saffrich, et al. (1997). "Cytoplasmic flows localize injected oskar RNA in Drosophila oocytes." Curr Biol **7**(5): 326-337.

Greijer, A. E., P. van der Groep, et al. (2005). "Up-regulation of gene expression by hypoxia is mediated predominantly by hypoxia-inducible factor 1 (HIF-1)." J Pathol **206**(3): 291-304.

Hailesellasse Sene, K., C. J. Porter, et al. (2007). "Gene function in early mouse embryonic stem cell differentiation." BMC Genomics **8**: 85.

Heinlein, M., B. L. Epel, et al. (1995). "Interaction of tobamovirus movement proteins with the plant cytoskeleton." Science **270**(5244): 1983-1985.

Hesketh, J. E., G. P. Campbell, et al. (1991). "c-myc mRNA in cytoskeletal-bound polysomes in fibroblasts." Biochem J **274 (Pt 2)**: 607-609.

Hesketh, J. E. and I. F. Pryme (1991). "Interaction between mRNA, ribosomes and the cytoskeleton." Biochem J **277 (Pt 1)**: 1-10.

Hill, M. A. and P. Gunning (1993). "Beta and gamma actin mRNAs are differentially located within myoblasts." J Cell Biol **122**(4): 825-832.

Hill, M. A., L. Schedlich, et al. (1994). "Serum-induced signal transduction determines the peripheral location of beta-actin mRNA within the cell." J Cell Biol **126**(5): 1221-1229.

Jambhekar, A. and J. L. Derisi (2007). "Cis-acting determinants of asymmetric, cytoplasmic RNA transport." RNA **13**(5): 625-642.

Jansen, R. P. (2001). "mRNA localization: message on the move." Nat Rev Mol Cell Biol **2**(4): 247-256.

Jonson, L., J. Vikesaa, et al. (2007). "Molecular composition of IMP1 ribonucleoprotein granules." Mol Cell Proteomics **6**(5): 798-811.
Jung, J., A. W. Lifland, et al. (2013). "Characterization of mRNA-cytoskeleton interactions in situ using FMTRIP and proximity ligation." PLoS One **8**(9): e74598.
Jung, J., A. W. Lifland, et al. (2013). "Quantifying RNA-protein interactions in situ using modified-MTRIPs and proximity ligation." Nucleic Acids Res **41**(1): e12.
Kalluri, R. and E. G. Neilson (2003). "Epithelial-mesenchymal transition and its implications for fibrosis." J Clin Invest **112**(12): 1776-1784.
Kedersha, N., G. Stoecklin, et al. (2005). "Stress granules and processing bodies are dynamically linked sites of mRNP remodeling." J Cell Biol **169**(6): 871-884.
Li, W. and I. N. Chou (1992). "Effects of sodium arsenite on the cytoskeleton and cellular glutathione levels in cultured cells." Toxicol Appl Pharmacol **114**(1): 132-139.
Lifland, A. W., C. Zurla, et al. (2011). "Dynamics of native beta-actin mRNA transport in the cytoplasm." Traffic **12**(8): 1000-1011.
Ling, S. C., P. S. Fahrner, et al. (2004). "Transport of Drosophila fragile X mental retardation protein-containing ribonucleoprotein granules by kinesin-1 and cytoplasmic dynein." Proc Natl Acad Sci U S A **101**(50): 17428-17433.
Martin, K. C. and A. Ephrussi (2009). "mRNA localization: gene expression in the spatial dimension." Cell **136**(4): 719-730.
Mathias, R. A. and R. J. Simpson (2009). "Towards understanding epithelial-mesenchymal transition: a proteomics perspective." Biochim Biophys Acta **1794**(9): 1325-1331.
Nemerow, G. R. and P. L. Stewart (1999). "Role of alpha(v) integrins in adenovirus cell entry and gene delivery." Microbiol Mol Biol Rev **63**(3): 725-734.
Oyanagi, J., T. Ogawa, et al. (2012). "Epithelial-mesenchymal transition stimulates human cancer cells to extend microtubule-based invasive protrusions and suppresses cell growth in collagen gel." PLoS One **7**(12): e53209.
Pillai, R. S., S. N. Bhattacharyya, et al. (2007). "Repression of protein synthesis by miRNAs: how many mechanisms?" Trends Cell Biol **17**(3): 118-126.
Pirozzi, G., V. Tirino, et al. (2011). "Epithelial to mesenchymal transition by TGFbeta-1 induction increases stemness characteristics in primary non small cell lung cancer cell line." PLoS One **6**(6): e21548.
Raju, C. S., N. Fukuda, et al. (2011). "In neurons, activity-dependent association of dendritically transported mRNA transcripts with the transacting factor CBF-A is mediated by A2RE/RTS elements." Mol Biol Cell **22**(11): 1864-1877.
Ratti, A., C. Fallini, et al. (2006). "A role for the ELAV RNA-binding proteins in neural stem cells: stabilization of Msi1 mRNA." J Cell Sci **119**(Pt 7): 1442-1452.
Rodriguez, A. J., S. M. Shenoy, et al. (2006). "Visualization of mRNA translation in living cells." J Cell Biol **175**(1): 67-76.
Sager, P. R. (1989). "Cytoskeletal effects of acrylamide and 2,5-hexanedione: selective aggregation of vimentin filaments." Toxicol Appl Pharmacol **97**(1): 141-155.
Santangelo, P. J., A. W. Lifland, et al. (2009). "Single molecule-sensitive probes for imaging RNA in live cells." Nat Methods **6**(5): 347-349.

Shulman, J. M., R. Benton, et al. (2000). "The Drosophila homolog of C. elegans PAR-1 organizes the oocyte cytoskeleton and directs oskar mRNA localization to the posterior pole." Cell **101**(4): 377-388.
Slobodin, B. and J. E. Gerst (2010). "A novel mRNA affinity purification technique for the identification of interacting proteins and transcripts in ribonucleoprotein complexes." RNA **16**(11): 2277-2290.
Soderberg, O., M. Gullberg, et al. (2006). "Direct observation of individual endogenous protein complexes in situ by proximity ligation." Nat Methods **3**(12): 995-1000.
Sundell, C. L. and R. H. Singer (1991). "Requirement of microfilaments in sorting of actin messenger RNA." Science **253**(5025): 1275-1277.
Suon, S., H. Jin, et al. (2004). "Transient differentiation of adult human bone marrow cells into neuron-like cells in culture: development of morphological and biochemical traits is mediated by different molecular mechanisms." Stem Cells Dev **13**(6): 625-635.
Swanger, S. A., G. J. Bassell, et al. (2011). "High-resolution fluorescence in situ hybridization to detect mRNAs in neuronal compartments in vitro and in vivo." Methods Mol Biol **714**: 103-123.
Takizawa, P. A., A. Sil, et al. (1997). "Actin-dependent localization of an RNA encoding a cell-fate determinant in yeast." Nature **389**(6646): 90-93.
Theurkauf, W. E., S. Smiley, et al. (1992). "Reorganization of the cytoskeleton during Drosophila oogenesis: implications for axis specification and intercellular transport." Development **115**(4): 923-936.
Wu, K. Y., U. Hengst, et al. (2005). "Local translation of RhoA regulates growth cone collapse." Nature **436**(7053): 1020-1024.
Xing, L. and G. J. Bassell (2013). "mRNA localization: an orchestration of assembly, traffic and synthesis." Traffic **14**(1): 2-14.
Zimber, A., Q. D. Nguyen, et al. (2004). "Nuclear bodies and compartments: functional roles and cellular signalling in health and disease." Cell Signal **16**(10): 1085-1104.
Zimyanin, V. L., K. Belaya, et al. (2008). "In vivo imaging of oskar mRNA transport reveals the mechanism of posterior localization." Cell **134**(5): 843-853.
Zurla, C., A. W. Lifland, et al. (2011). "Characterizing mRNA interactions with RNA granules during translation initiation inhibition." PLoS One **6**(5): e19727.

CHAPTER 4

DETECTING HuR-mRNA INTERACTIONS USING PLA

The work presented here is an excerpt from Jung, J, Lifland, AW, Zurla, C, Alonas, EJ, Santangelo, PJ (2013). "Quantifying RNA-protein interactions in situ using modified-MTRIPs and proximity ligation." Nucleic Acids Res **41**(1): e12.

Background

Post-transcriptional processes are critical to ensure the proper gene expression in a cell. A myriad of RNA binding proteins and noncoding RNAs, such as micro RNAs (miRNAs), mediate these post-transcriptional events and are, therefore, key factors in modulating gene expression (Keene 2007; Cech and Steitz 2014). Highlighting the importance of these events, there are a growing number of examples in which the dysregulation of RNA binding proteins or miRNAs and, in turn, the post-transcriptional processing events they mediate are associated with various types of cancer (Lukong, Chang et al. 2008; Srikantan and Gorospe 2012; Blackinton and Keene 2014; Chan, Hieter et al. 2014).

The 3′ untranslated region (UTR) of an mRNA transcript is the site of binding and regulation for many post-transcriptional factors. The AU-Rich Element Binding Proteins represent one class of RNA binding proteins that mediate their post-transcriptional function by binding to AU- or U-rich RNA elements (AREs) located primarily within the 3′UTRs of target mRNAs. This protein family which includes the mRNA stability factor,

Human antigen R (HuR), plays a role in the post-transcriptional regulation of a number of biologically important mRNAs (Abdelmohsen and Gorospe 2010; Khabar 2010).

HuR is the ubiquitously expressed member of the embryonic lethal abnormal vision (ELAV) family of RNA binding proteins (Ma, Cheng et al. 1996). Two N-terminal RNA Recognition Motifs (RRMs) within HuR mediate recognition of AREs located primarily within the 3′UTR of target mRNA transcripts (Uren, Burns et al. 2011; Wang, Zeng et al. 2013). A third RRM in the C-terminus of HuR has affinity for polyadenosine RNA and is thought to bind to the poly(A) tail of target mRNAs (Abe, Sakashita et al. 1996; Ma, Chung et al. 1997). HuR localizes to the nucleus at steady-state but can shuttle out of the nucleus when the cell experiences stress such as oxidative stress (Anderson and Kedersha 2002) or transcriptional inhibition (Fan and Steitz 1998). For the majority of HuR target transcripts, association with HuR in the cytoplasm leads to increased stability of the HuR-bound target mRNA, ultimately resulting in an increase in steady-state protein level (Brennan and Steitz 2001). In addition to this conventional role of HuR in stabilizing RNA, recent work has revealed that HuR can increase the expression of target transcripts without affecting their stability (Mazan-Mamczarz, Galban et al. 2003; Lal, Kawai et al. 2005).

Recent transcriptome-wide analyses of HuR binding reveal a large number of candidate mRNA targets that could be bound and regulated by these RNA binding proteins. These studies suggest HuR binding to approximately 10% of the transcriptome, specifically within the 3′UTRs and introns of these candidate target transcripts. Further analyses of these sequencing studies reveal a robust preference of HuR for U-rich sequences, which challenges the previously held belief that HuR is an exclusively AU-

rich RNA binding protein. (Lebedeva, Jens et al. 2011; Mukherjee, Corcoran et al. 2011; Uren, Burns et al. 2011) Secondary structural predictions of the candidate HuR binding sites suggest a preference for single-stranded RNA for binding to HuR, specifically within the context of a loop (Lopez de Silanes, Zhan et al. 2004; Uren, Burns et al. 2011).

HuR is an important stabilizing RNA-binding protein that usually binds to the 3'UTR. Its localization in the cytoplasm is important in its function and binding to the mRNA. It is difficult to visualize HuR-mRNA interactions and the location of these interactions *in situ* in cells using conventional biochemical assays. Here, we used flag-tagged multiply labeled tetravalent RNA imaging probes (FMTRIPs) and proximity ligation assay (PLA) to image interactions between HuR and mRNAs. We examined *poly(A)+* and *β-actin* mRNAs under varying levels of HuR and actinomycin D (actD) induced transcription inhibition. PLA successfully detected HuR-mRNA complexes with good specificity and sensitivity. Exogenous RNAs with and without the HuR binding site were used to test for the specificity of this method in detecting HuR RNA interactions *in situ*. Changes in the interactions under different levels of HuR and actD exposure demonstrated the sensitivity.

HuR-mRNA interactions can be imaged and quantified by PLA

In order to test the specificity of proximity ligation assay (PLA) to detect interactions between HuR and mRNAs, HuR interactions with plasmid-derived mRNAs with and without HuR binding site in varying levels of HuR were studied. We used plasmids that encode RNAs spanning the green fluorescent protein (GFP) coding region and the *c-Myc* 3'UTR (referred to as *c-Myc*) with and without the HuR binding site (*c-*

Myc AB and *c-Myc A*, respectively). The 3'UTR A segment precedes the HuR binding site in the B segment. (Kim, Kuwano et al. 2009) We designed RNA imaging probes to target three sites on the *c-Myc* 3'UTR A region, which are proximal to the HuR binding site in the B region. The probes are not complementary to any native mRNA in Vero cells, which were used for all the experiments.

In cells transfected with c-Myc A, the plasmid lacking the HuR binding site, we observed no PLA signal between *c-Myc* and HuR, as expected (**Figure 4.1**). To further test the specificity, we increased HuR by transfecting Vero cells with both c-Myc A and HuR-GFP. With this increased HuR, there was a small increase in the mean PLA frequency, likely due to increased random interactions between *c-Myc* and HuR. In contrast, c-Myc AB transfection resulted in PLA signal between *c-Myc* and HuR (**Figure 4.1**). The difference in the mean PLA frequency between cells expressing c-Myc A or c-Myc AB was statistically significant ($p<0.001$). In cells expressing both c-Myc AB and increased HuR via HuR-GFP co-transfection, the frequency of interactions also increased, similar to the increase observed in cells expressing both c-Myc A and HuR-GFP. But the difference in the frequency of interactions between cells expressing c-Myc A or c-Myc AB was statistically significant ($p=0.028$), still. Again, the increase is probably due to increased non-specific interactions with increased levels of HuR. Clearly, PLA can accurately detect HuR interactions only with the RNA containing the HuR binding site.

HuR-mRNA interactions increase with HuR overexpression and actD exposure

With the specificity of the PLA method established, we wanted to test how sensitive this method is at detecting varying levels of HuR. We examined HuR interactions with *poly(A)+* or *β-actin* mRNA in HeLa cells transfected with HuR-GFP to overexpress HuR. After 36 hours of transfection, the cells were delivered RNA imaging probes and fixed after 15 minutes of recovery. Considering that different number of probes may bind to each mRNA, we tested whether the number of probes bound per mRNA affected the number of PLA punctae per mRNA. We delivered three probes targeting the coding region of *β-actin*, three targeting the 3'-UTR, or all six (**Figure 4.2**). Hence, PLA detected the occurrence of single interaction between HuR and the closest probe bound to *β-actin* mRNA; therefore, the presence of additional probes on the mRNA did not increase the number of detected interactions.

In addition to the variability in transfection efficiency, which contributed to varying amounts of HuR, we observed cell-to-cell variability in mRNA amounts and HuR-mRNA interactions as measured by PLA punctae (**Figure 4.3**). It is important to note that because the difference between the nuclear and cytoplasmic concentrations of HuR is beyond the imageable dynamic range using immunofluorescence ((Fan and Steitz 1998; Peng, Chen et al. 1998), the cytoplasmic HuR fraction could not be imaged without saturating the nuclear signal. Hence, even though HuR may not be observable in the photomicrographs, PLA occurred in the cytoplasm where HuR and mRNA interact due to the greater sensitivity of PLA.

In order to produce meaningful statistical data, for each transfection condition, we analyzed only the cells expressing similar levels of nuclear HuR as measured using the mean IF intensity (600–1000 a.u.). It should also be noted that the concentration of

poly(A) FMTRIPs used (60 nM) was less than the concentration that resulted in the maximum intensity (90 nM). By under-sampling, we were able to label a random portion of the mRNA population, which facilitated the imaging of individual granules and detection of relative changes in HuR interactions. β-actin FMTRIPs were delivered at a concentration (20nM for each of three FMTRIPs) such that they bind to >80% of the *β-actin* mRNA (Lifland, Zurla et al. 2011).

First, we quantified how the mRNA signal varied under our experimental conditions. Under normal growth conditions, cytoplasmic mRNAs, as detected using poly(A) FMTRIPs, were found to be more abundant in untransfected HeLa cells than in the transfected ones (**Figure 4.4** and **Table 4.3**). The large, observed standard deviation was likely due to the heterogeneity in the population. Whereas HuR overexpression did not increase the overall cytoplasmic mRNA amount, we found that it dramatically slowed the effect of actD in reducing mRNA number, after 30 min of exposure. (**Figure 4.4**; **Table 4.3** and **4.4**) ActD treatment on HuR-transfected cells had more dramatic effects on *β-actin* mRNA, both as detected by using 3'-UTR FMTRIPs and analyzed by qRT–PCR. HuR overexpression stabilized the *β-actin* mRNA and increased its quantity in the cytoplasm, consistent with the findings by Dormoy-Raclet et al. (Dormoy-Raclet, Menard et al. 2007) (**Figure 4.4**). With 60 min exposure to actD, the *β-actin* mRNA decreased to similar levels in transfected and untransfected cells.

In order to demonstrate the specificity and sensitivity of PLA, we compared PLA signal in cells containing untargeted or targeted FMTIRPs and with varying levels of HuR (**Figure 4.5**). In cells with untargeted probes, the PLA signal was minimal (**Figure 4.5**). However, in HuR-GFP transfected cells with increased levels of HuR, the mean

PLA frequency increased to a level similar to the untransfected cells with poly(A) FMTRIPs, but significantly less than the HuR-GFP transfected cells delivered poly(A) FMTRIPs (**Figure 4.5**). This was likely due to increased random interactions between FMTRIP and HuR with a greater amount of HuR in the cytoplasm. When the HuR level was decreased using HuR siRNA, the PLA signal fell to a minimal level, similar to the untransfected cells containing untargeted probes (**Figure 4.5**). In contrast, in cells transfected with a control siRNA that had no effect on HuR, the mean PLA frequency was similar to that of the untransfected cells delivered poly(A) FMTRIPs (**Figure 4.5**). Here, we showed that PLA specifically detected interactions between the *poly(A)+* mRNA and HuR. The mean PLA frequency quantifiably demonstrated changes in the frequency of interactions between mRNA and HuR, as the amount of HuR decreased and increased.

Next, given that actD exposure has been shown to increase HuR binding to mRNA in the cytoplasm (Peng, Chen et al. 1998), we quantified the HuR–mRNA interactions via PLA but selected cells with a similar range of FMTRIP signal volume (poly(A), 60 ± 40 μm^3; β-actin, 160 ± 90 μm^3). The mean PLA frequency increased with HuR overexpression and longer exposure to actD (**Figure 4.5**). Specifically, in transfected cells and in the absence of actD, the frequency of HuR interactions increased 99% with poly(A)+ mRNA (**Figure 4.5**) and 255% with *β-actin* mRNA (**Figure 4.6**) greater than in untransfected cells. In transfected cells and in the presence of actD, the frequency of HuR interactions increased 184% with *poly(A)+* mRNA (**Figure 4.5**) and 250% with *β-actin* mRNA (**Figure 4.6**). No PLA was observed in transfected, MTRIP-delivered (no flag tag) cells (**Figure 4.5**). Although these changes in mRNA stability and

interactions resulting from changes in HuR localization may seem less than those reported using UV-cross-linking (Lebedeva, Jens et al. 2011; Mukherjee, Corcoran et al. 2011) and gel shift assay (Peng, Chen et al. 1998), our findings show changes in individual cells, not in cell lysates.

Conclusion

We imaged and quantified interactions between *poly(A)+* mRNA (Zurla, Lifland et al. 2011) or *β-actin* mRNA (Lifland, Zurla et al. 2011) and an RBP, HuR, whose interactions with mRNAs have been implicated in tumorigenesis (Yeap, Voon et al. 2002; Mazan-Mamczarz, Galban et al. 2003; Lal, Kawai et al. 2005). HuR binds to the poly(A) tail (Ma, Chung et al. 1997) and the 3'UTR of many genes, including *β-actin* (Misquitta, Iyer et al. 2001; Dormoy-Raclet, Menard et al. 2007; Lopez de Silanes, Quesada et al. 2007). Although predominately within the nucleus, HuR has been shown to shuttle between the nucleus and the cytoplasm through its nucleocytoplasmic shuttling domain, when cells are exposed to specific stimuli, such as actD (Fan and Steitz 1998). Although we observed cell-to-cell variability in the amount of HuR and mRNA, as well as in the frequency of their interactions, HuR–mRNA interactions generally increased as the amount of HuR increased in the cytoplasm, whereas the amount of mRNA decreased with actD exposure. One clear advantage of this methodology is that it allowed us to quantify the cell-to-cell variability in RNA expression and interactions simultaneously, which is challenging with other methods, such as biochemical assays and imaging methods.

With normal HuR regulation of mRNAs disrupted in various cancer types (Mazan-Mamczarz, Galban et al. 2003; Abdelmohsen and Gorospe 2010; Blackinton and

Keene 2014), applying this method to investigate changes in HuR interactions in cancerous cells and tissues may offer numerous advantages. For example, a deeper understanding of gene expression can be gained from examining changes in RBP and mRNA interactions in both space and time on a per cell basis (Pelkmans 2012). Addressing this challenge can be difficult with conventional biochemical methods and imaging tools (Welch, Elliott et al. 2011). Although an averaged view of the interaction network may provide valuable information, the spatiotemporal and cell-to-cell variation of RNA–protein interactions are important for investigating their role in a variety of cellular events, such as identifying oncogenic, aberrant RNA–protein interactions that precede the synthesis of cancer-causing proteins among a heterogeneous population of cancerous and healthy cells.

The FMTRIP-based PLA method is a powerful tool that meets this challenge. It provides accurate, easily detectable, quantifiable spatiotemporal information from which causal inference and hypothesis-driven statistics can be derived about the post-transcriptional regulation of RNA. This technique allows collection of large, high-throughput data that are necessary for mapping the RNA–protein interactome *in situ* and for rapid identification of interactions between a series of RNA sequences and their potential RBPs. It has potential to serve as a valuable diagnostic tool for disorders involving abnormal post-transcriptional regulations.

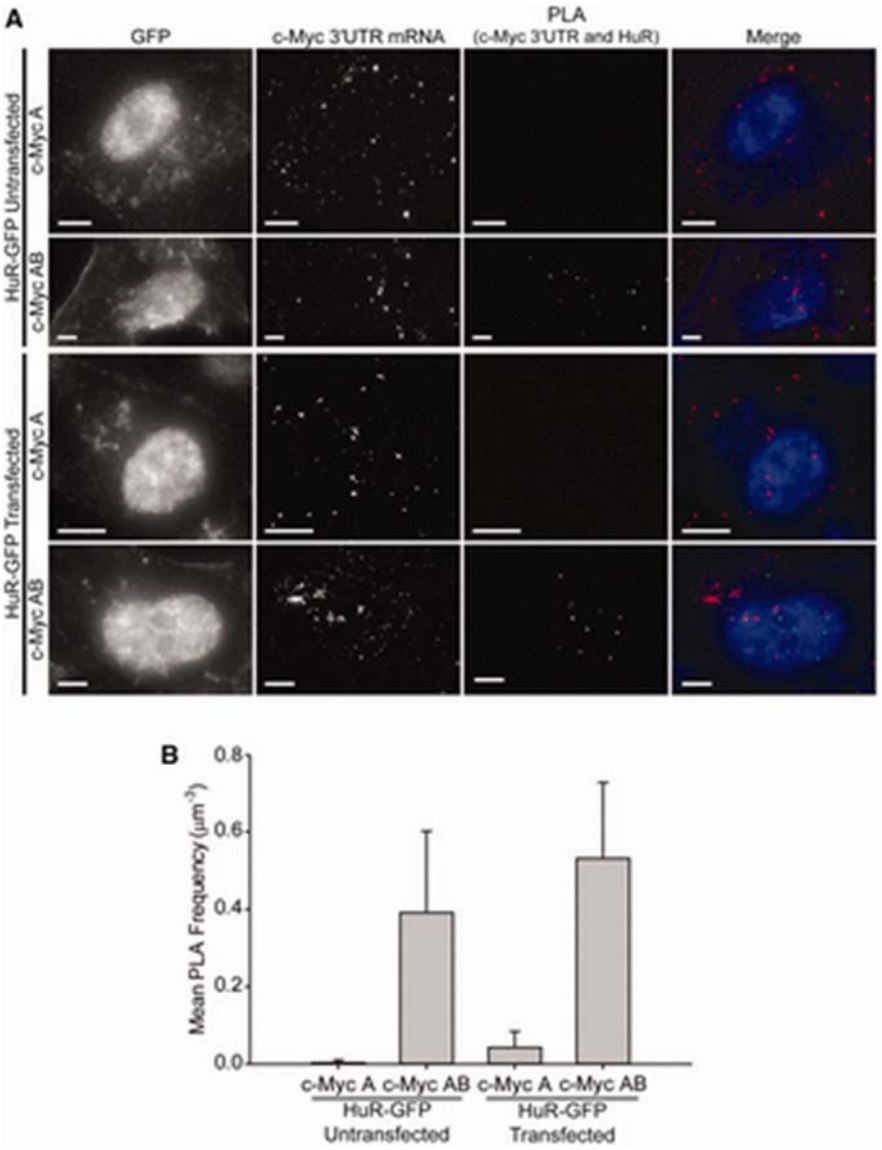

Figure 4.1: Imaging and quantification of PLA between HuR and *c-Myc* 3′-UTR mRNA containing the HuR-binding site (c-Myc AB) or lacking it (c-Myc A) in Vero cells with varying levels of HuR. (A) GFP IF, *c-Myc* 3′-UTR mRNA, PLA between *c-Myc* 3′-UTR and HuR were imaged in untransfected and HuR-GFP transfected Vero cells co-transfected with either GFP-c-Myc A or GFP-c-Myc AB. Merged images of GFP IF (blue), *c-Myc* 3′-UTR mRNA (red) and PLA (green) are shown. All the images were deconvolved, except for GFP and PLA. All image planes are represented. Scale bar: 5 μm. (B) The mean PLA frequency was minimal in cells transfected with c-Myc A, lacking the HuR-binding site. It was significantly greater in the presence of HuR-binding site with c-Myc AB transfection. (**Table 4.1** for two-way ANOVA with Holm–Sidak method and **Table 4.2** for Kruskal–Wallis one-way ANOVA with Dunn's method for multiple comparisons) Error bars, SD. (Jung, Lifland et al. 2013)

Table 4.1: Comparisons of the mean PLA frequency detecting interactions between *c-Myc* and HuR in Vero cells with varying HuR levels using two-way ANOVA with Holm-Sidak method. There was no significant interaction between HuR and c-Myc transfection (p=0.210). (HuR-GFP Untransfected: c-Myc A, n = 15, mean = 0.00, s.d. = 0.00; c-Myc AB, n = 19, mean = 0.39, s.d. = 0.21; HuR-GFP Transfected: c-Myc A, n = 12, mean = 0.04, s.d. = 0.04; c-Myc AB, n = 15, mean = 0.53, s.d. = 0.20). (Jung, Lifland et al. 2013)

Comparison	P	P<0.05
c-Myc A vs c-Myc AB	<0.001	Yes
HuR-GFP Untransfected vs Transfected	0.028	Yes

Table 4.2: Comparisons of the mean PLA frequency detecting interactions between *c-Myc* and HuR in Vero cells with varying HuR levels using Kruskal-Wallis one-way ANOVA with Dunn's method for multiple comparisons. (HuR-GFP Untransfected: c-Myc A, n = 15, mean = 0.00, s.d. = 0.00; c-Myc AB, n = 19, mean = 0.39, s.d. = 0.21; HuR-GFP Transfected: c-Myc A, n = 12, mean = 0.04, s.d. = 0.04; c-Myc AB, n = 15, mean = 0.53, s.d. = 0.20) (Jung, Lifland et al. 2013)

Comparison	Diff of Ranks	Q	P<0.05
c-Myc A vs c-Myc AB	30.2	3.6	Yes
HuR-GFP, c-Myc A vs HuR-GFP c-Myc AB	30.9	4.5	Yes
c-Myc A vs HuR-GFP, c-Myc A	6.8	1.0	No
c-Myc A vs HuR-GFP, c-Myc AB	37.7	5.8	Yes
c-Myc AB vs HuR-GFP, c-Myc A	23.5	3.6	Yes
c-Myc AB vs HuR-GFP, c-Myc AB	7.5	1.2	No

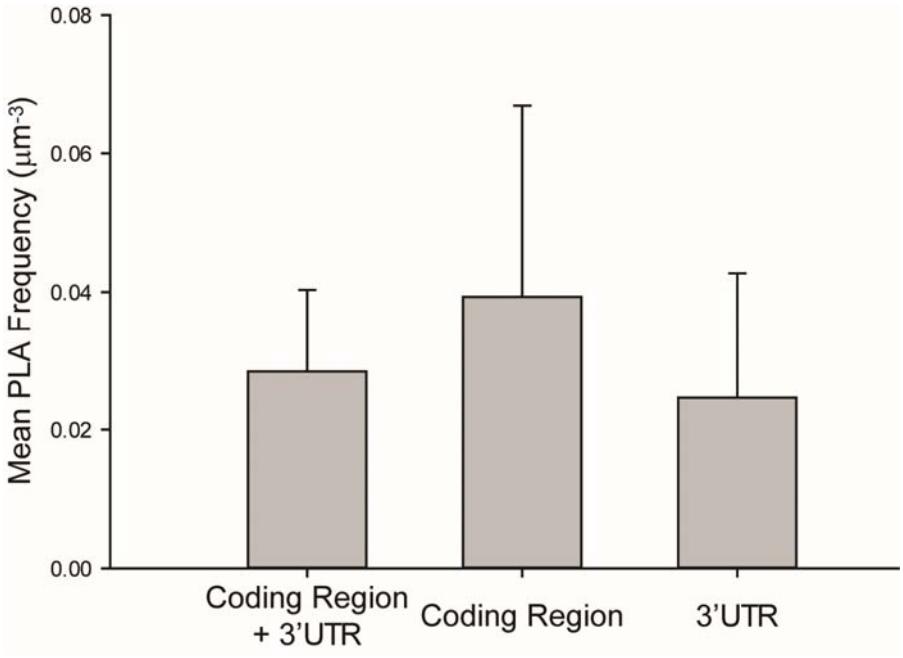

Figure 4.2: Quantification of the mean HuR-*βactin* PLA frequency in cells delivered FMTRIPs targeting the coding region of *β-actin*, its 3′UTR or both. Three FMTRIPs targeting the coding regions and three targeting 3′UTR were used. All six were used to detect both. No significant difference was observed with varying number of FMTRIPs (p=0.3, Kruskal-Wallis one-way ANOVA on ranks) (Coding region+3'UTR: n=14, mean=0.03, s.d.= 0.01; Coding region: n=12, mean=0.04, s.d.=0.03; 3′UTR: n=14, mean=0.02, s.d.=0.02). Error bars, s.d. (Jung, Lifland et al. 2013)

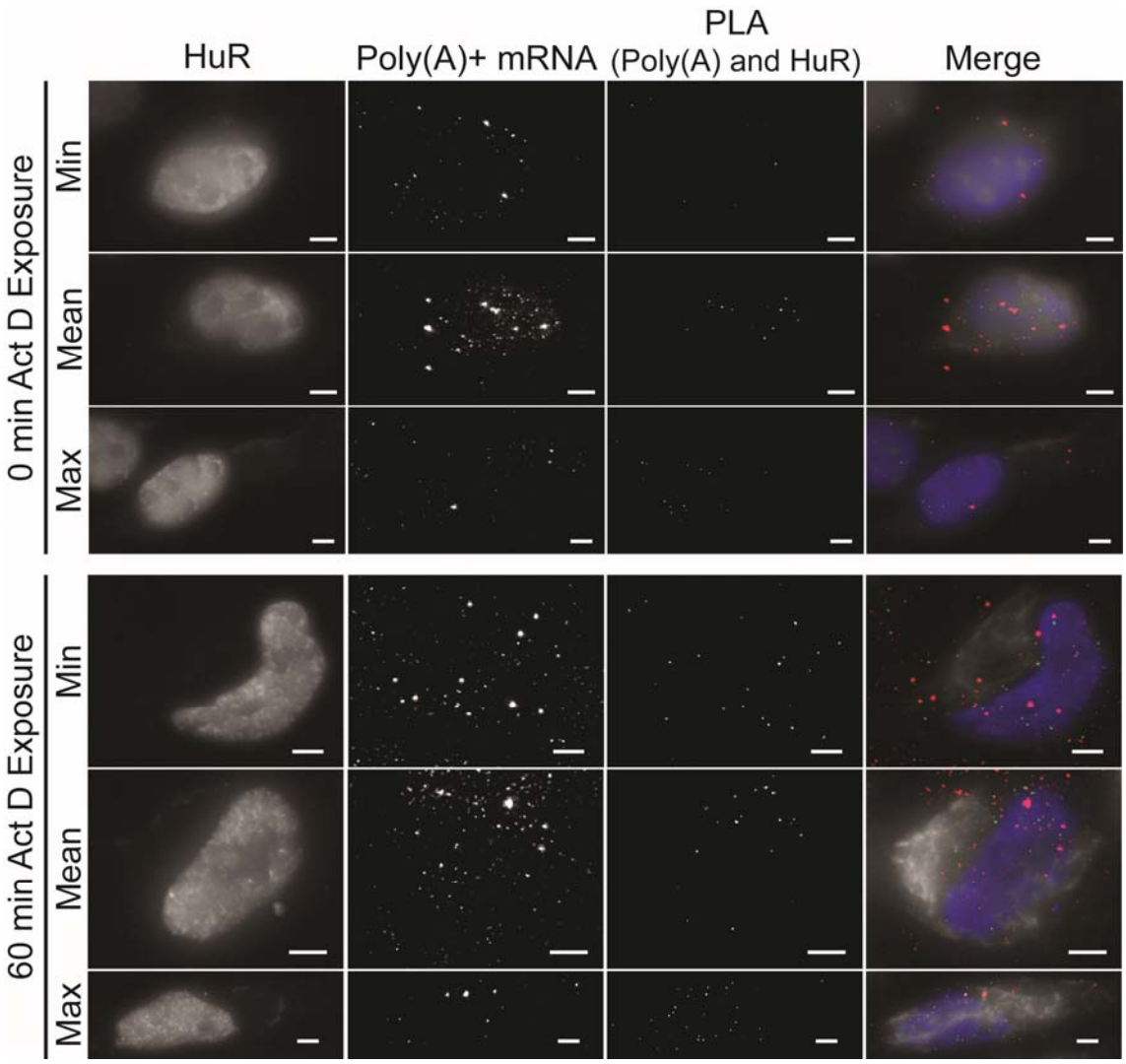

Figure 4.3: Imaging and quantification of cell-to-cell variability in HuR interactions with *poly(A)*. HuR IF, *poly(A)*+ mRNA, PLA between *poly(A)* and HuR were imaged in transfected HeLa cells with the mean HuR IF intensity and volume within 1 s.d. after 0 and 60 min Actinomycin D (actD) exposure. Those with the minimum (min), mean and maximum (max) PLA frequency imaged using a widefield microscope are shown. Merged images of vimentin IF (white), *poly(A)*+ mRNA (red), PLA (green) and HuR IF (blue) are shown. All the images were deconvolved, except for HuR and vimentin IF. All image planes are represented. Scale bar, 5 μm. (Jung, Lifland et al. 2013)

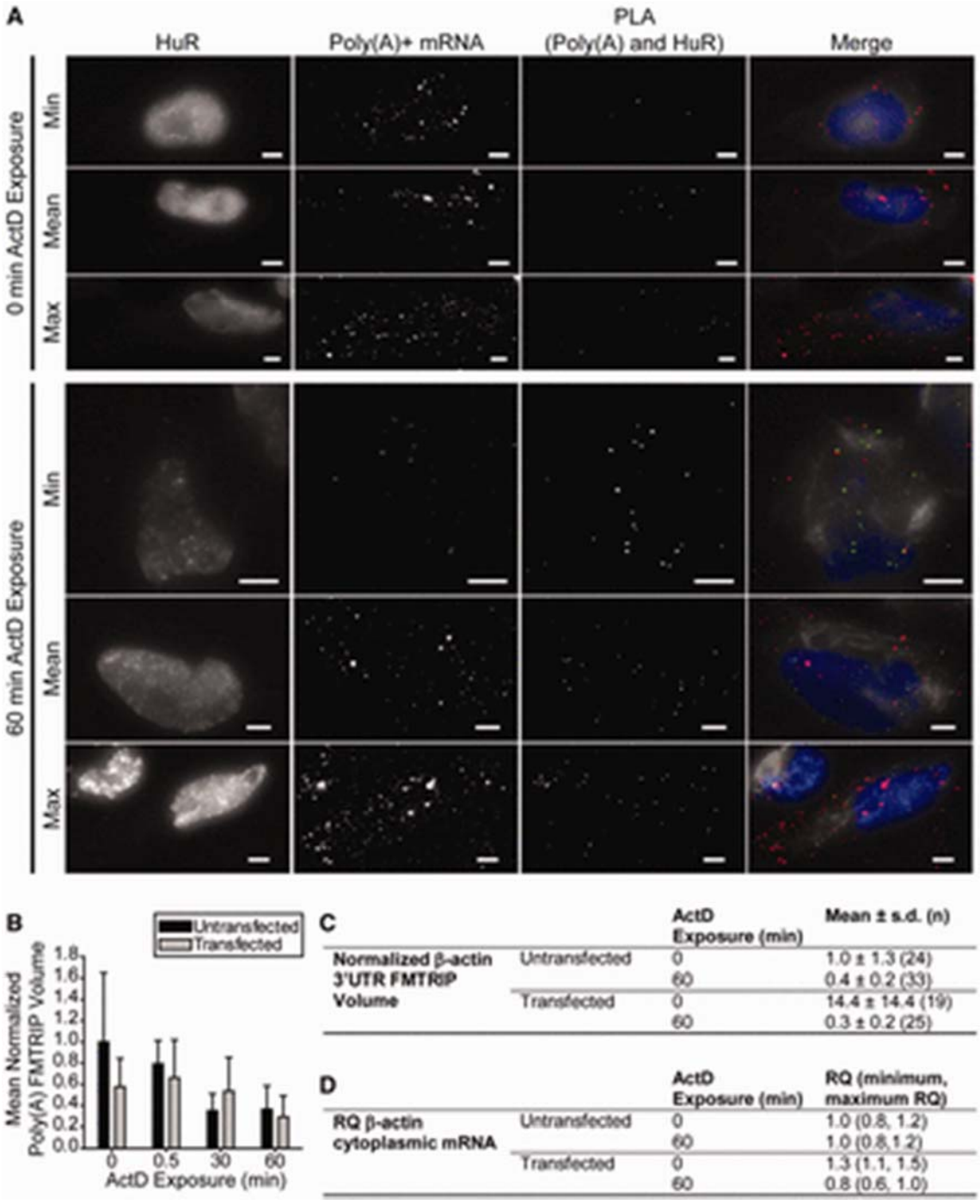

C

		ActD Exposure (min)	Mean ± s.d. (n)
Normalized β-actin 3'UTR FMTRIP Volume	Untransfected	0	1.0 ± 1.3 (24)
		60	0.4 ± 0.2 (33)
	Transfected	0	14.4 ± 14.4 (19)
		60	0.3 ± 0.2 (25)

D

		ActD Exposure (min)	RQ (minimum, maximum RQ)
RQ β-actin cytoplasmic mRNA	Untransfected	0	1.0 (0.8, 1.2)
		60	1.0 (0.8,1.2)
	Transfected	0	1.3 (1.1, 1.5)
		60	0.8 (0.6, 1.0)

Figure 4.4: Imaging and quantification of cell-to-cell variability in *poly(A)*+ and *β-actin* mRNA. (A) HuR IF, *poly(A)*+ mRNA, PLA between *poly(A)* and HuR were imaged in transfected HeLa cells with the mean HuR IF intensity and volume within 1 SD after 0 and 60 min actD exposure. Those with the minimum (min), mean and maximum (max) mRNA volume and PLA frequency imaged using a widefield microscope are shown. Merged images of vimentin IF (white), *poly(A)*+ mRNA (red), PLA (green) and HuR IF (blue) are shown. All the images were deconvolved, except for

HuR and vimentin IF. All image planes are represented. Scale bar, 5 μm. (B) Comparison of the mean normalized poly(A) FMTRIP volume in HuR-GFP transfected and untransfected HeLa cells exposed to actD for 0–60 min. The values were normalized to the mean of untransfected cells with 0 min actD exposure. FMTRIP volume decreased with longer actD (5 μg/ml) exposure. (**Table 4.3-4.5** for two-way ANOVA with Holm–Sidak method) (C) Comparison of the mean normalized *β-actin* 3′-UTR FMTRIP volume in HuR-GFP transfected and untransfected HeLa cells exposed to actD for 0 and 60 min. The values were normalized to the mean of untransfected cells with 0 min actD exposure. Generally, FMTRIP volume decreased with longer actD exposure. Without actD, the mean FMTRIP volume in transfected cells was significantly greater than that of untransfected cells. (**Tables 4.6-4.8** for two-way ANOVA with Holm–Sidak method) (D) Comparison of the RQ of *β-actin* cytoplasmic mRNA determined using qRT–PCR of RNA collected from HuR-GFP transfected and untransfected HeLa cells exposed to actD for 0 and 60 min. (**Tables 4.9-4.11** for two-way ANOVA with Bonferroni *post-hoc* method). (Jung, Lifland et al. 2013)

Table 4.3: Comparisons of the mean normalized poly(A) FMTRIP volume between untransfected and transfected HeLa cells at each actD exposure time from 0 to 60 min using two-way ANOVA Holm-Sidak method (Untransfected: 0 min, n = 36, mean = 1.0, s.d. = 0.6; 0.5 min, n = 33, mean = 0.8, s.d. = 0.2; 30 min, n = 35, mean = 0.4, s.d. = 0.2; 60 min, n = 33, mean = 0.4, s.d. = 0.2; Transfected: 0 min, n = 70, mean = 0.6, s.d. = 0.3; 0.5 min, n = 70, mean = 0.7, s.d. = 0.3; 30 min, n = 29, mean = 0.5, s.d. = 0.3; 60 min, n = 41, mean = 0.3, s.d. = 0.2). (Jung, Lifland et al. 2013)

Actinomycin D Exposure (min)	Comparison	P	P<0.05
0	Untransfected vs Transfected	<0.001	Yes
0.5	Untransfected vs Transfected	0.056	No
30	Untransfected vs Transfected	0.027	Yes
60	Untransfected vs Transfected	0.350	No

Table 4.4: Comparisons of the mean normalized poly(A) FMTRIP volume in untransfected HeLa cells between different actD exposure times from 0 to 60 min using two-way ANOVA Holm-Sidak method (Untransfected: 0 min, n = 36, mean = 1.0, s.d. = 0.6; 0.5 min, n = 33, mean = 0.8, s.d. = 0.2; 30 min, n = 35, mean = 0.4, s.d. = 0.2; 60 min, n = 33, mean = 0.4, s.d. = 0.2). (Jung, Lifland et al. 2013)

Comparison	P	P<0.05
60 min vs 0 min	<0.001	Yes
60 min vs 0.5 min	<0.001	Yes
60 min vs 30 min	0.864	No
30 min vs 0.5 min	<0.001	Yes
30 min vs 0 min	<0.001	Yes
0 min vs 0.5 min	0.019	Yes

Table 4.5: Comparisons of the mean normalized poly(A) FMTRIP volume in transfected HeLa cells between different actD exposure times from 0 to 60 min using two-way ANOVA Holm-Sidak method (Transfected: 0 min, n = 70, mean = 0.6, s.d. = 0.3; 0.5 min, n = 70, mean = 0.7, s.d. = 0.3; 30 min, n = 29, mean = 0.5, s.d. = 0.3; 60 min, n = 41, mean = 0.3, s.d. = 0.2). (Jung, Lifland et al. 2013)

Comparison	P	P<0.05
60 min vs 0 min	<0.001	Yes
60 min vs 0.5 min	<0.001	Yes
60 min vs 30 min	0.010	Yes
30 min vs 0.5 min	0.243	No
30 min vs 0 min	0.576	No
0 min vs 0.5 min	0.251	No

Table 4.6: Comparisons of the mean β-actin 3′UTR FMTRIP volume between untransfected and transfected HeLa cells at 0 and 60 min actD exposure using two-way ANOVA Holm-Sidak method (Untransfected: 0 min, n = 24, mean = 1.0, s.d. = 1.3; 60 min, n = 33, mean = 0.4, s.d. = 0.2; Transfected: 0 min, n = 19, mean = 14.4, s.d. = 14.4; 60 min, n = 25, mean = 0.3, s.d. = 0.2). (Jung, Lifland et al. 2013)

Actinomycin D Exposure (min)	Comparison	P	P<0.05
0	Untransfected vs Transfected	<0.001	Yes
60	Untransfected vs Transfected	0.939	No

Table 4.7: Comparisons of the mean β-actin 3′UTR FMTRIP volume in untransfected HeLa cells between 0 and 60 min actD exposure using two-way ANOVA Holm-Sidak method (Untransfected: 0 min, n = 24, mean = 1.0, s.d. = 1.3; 60 min, n = 33, mean = 0.4, s.d. = 0.2). (Jung, Lifland et al. 2013)

Comparison	P	P<0.05
60 min vs 0 min	0.736	No

Table 4.8: Comparisons of the mean β-actin 3′UTR FMTRIP volume in transfected HeLa cells between 0 and 60 min actD exposure using two-way ANOVA Holm-Sidak method (Transfected: 0 min, n = 19, mean = 14.4, s.d. = 14.4; 60 min, n = 25, mean = 0.3, s.d. = 0.2). (Jung, Lifland et al. 2013)

Comparison	P	P<0.05
60 min vs 0 min	<0.001	Yes

Table 4.9: **Comparisons of the mean normalized *β-actin* cytoplasmic mRNA threshold cycle (ΔC_T) between untransfected and transfected HeLa cells at 0 and 60 min actD exposure using two-way ANOVA with Bonferroni post-hoc test.** (Jung, Lifland et al. 2013)

Actinomycin D Exposure (min)	Comparison	P	P<0.05
0	Untransfected vs Transfected	0.1107	No
60	Untransfected vs Transfected	0.0745	No

Table 4.10: Comparisons of the mean normalized *β-actin* cytoplasmic mRNA threshold cycle (ΔC_T) in untransfected HeLa cells between 0 and 60 min actD exposure using two-way ANOVA with Bonferroni post-hoc test. (Jung, Lifland et al. 2013)

Comparison	P	P<0.05
60 min vs 0 min	0.198	No

Table 4.11: Comparisons of the mean normalized *β-actin* cytoplasmic mRNA ΔC_T in transfected HeLa cells between 0 and 60 min actD exposure using two-way ANOVA with Bonferroni post-hoc test. (Jung, Lifland et al. 2013)

Comparison	P	P<0.05
60 min vs 0 min	0.0179	Yes

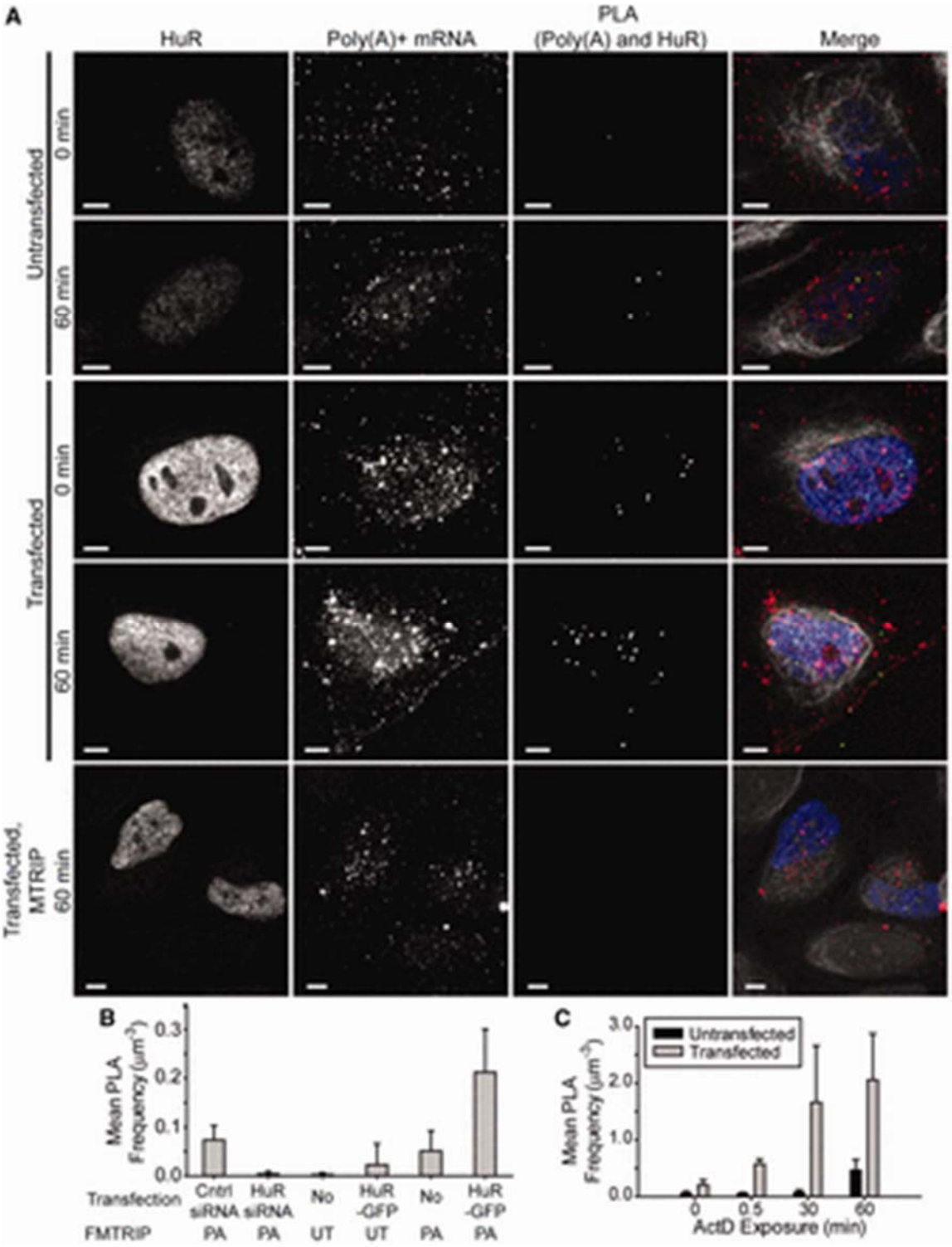

Figure 4.5: Imaging and quantification of interactions between HuR and *poly(A)*+ mRNA in HuR-GFP transfected and untransfected HeLa cells exposed to actD for 0–60 min. (A) HuR IF, poly(A)+ mRNA, PLA between *Poly(A)* and HuR were imaged in untransfected and transfected HeLa cells exposed to actD for 0 and 60 min, using a

laser-scanning confocal microscope. Untagged-MTRIP delivered transfected cells after 60 min actD exposure are shown as a negative control. Merged images of vimentin IF (white), *poly(A)+* mRNA (red), PLA (green) and HuR IF (blue) are shown. All image planes are represented. Scale bar, 5 μm. (B) The mean HuR-*poly(A)* PLA frequency in HeLa cells transfected with 200 nM HuR siRNA (Transfection = HuR siRNA, MTRIP = PA) was minimal, whereas it was similar in cells transfected with 200 nM control siRNA (Transfection = control siRNA, MTRIP = PA) and the untransfected cells (Transfection = No, MTRIP = PA). In cell-delivered untargeted MTRIPs (UT), the mean HuR-UT PLA frequency (Transfection = No, MTRIP = UT) was minimal. With HuR-GFP transfection (Transfection = HuR-GFP, MTRIP = UT), it increased but remained less than the mean HuR-poly(A) PLA frequency of untransfected (Transfection = No, MTRIP = PA) and transfected (Transfection = HuR-GFP, MTRIP = PA) cells. (**Tables 4.12-4.16**) (C) The mean HuR-*poly(A)* PLA frequency increased with longer exposure to actD (5 μg/ml) in untransfected and transfected HeLa cells. (**Tables 4.17-4.19** for two-way ANOVA with Holm–Sidak method) Error bars, standard deviation. (Jung, Lifland et al. 2013)

Table 4.12: Comparison between the mean HuR-*poly(A)* and HuR-untargeted FMTRIP PLA frequency in untransfected and transfected HeLa cells using two-way ANOVA Holm-Sidak method. (Jung, Lifland et al. 2013)

Transfection	Comparison	P	P<0.05
Untransfected	HuR-poly(A) vs HuR-untargeted	0.02	Yes
HuR-GFP	HuR-poly(A) vs HuR-untargeted	<0.001	Yes

Table 4.13: Comparison of the mean HuR-*poly(A)* or HuR-untargeted FMTRIP PLA frequency between untransfected and HuR-GFP transfected HeLa cells using two-way ANOVA Holm-Sidak method. (Jung, Lifland et al. 2013)

PLA	Comparison	P	P<0.05
HuR-poly(A)	Untransfected vs HuR-GFP Transfected	<0.001	Yes
HuR-untargeted	Untransfected vs HuR-GFP Transfected	0.388	No

Table 4.14: Comparison of the mean HuR-*poly(A)* or HuR-untargeted FMTRIP PLA frequency between untransfected and HuR-GFP transfected HeLa cells using Kruskal-Wallis one-way ANOVA on ranks with Dunn's method for multiple comparisons. (Jung, Lifland et al. 2013)

Comparison	Diff of Ranks	Q	P<0.05
HuR-GFP, poly(A) vs Untransfected, untargeted	45.5	6.4	Yes
HuR-GFP, poly(A) vs HuR-GFP, untargeted	38.4	5.4	Yes
HuR-GFP, poly(A) vs Untransfected, poly(A)	22.5	3.8	Yes
Untransfected, poly(A) vs Untransfected, untargeted	23.0	3.3	Yes
Untransfected, poly(A) vs HuR-GFP, untargeted	15.9	2.3	No
Transfected, untargeted vs Untransfected, untargeted	7.1	0.9	No

Table 4.15: Comparisons of the mean HuR-*poly(A)* PLA frequency at varying HuR levels in HeLa cells using Kruskal-Wallis one-way ANOVA on ranks with Dunn's method for multiple comparisons. (Jung, Lifland et al. 2013)

Comparison	Diff of Ranks	Q	P<0.05
HuR-GFP (↑ HuR) vs HuR siRNA (↓ HuR)	61.6	8.1	Yes
HuR-GFP (↑ HuR) vs Untransfected	34.3	4.7	Yes
HuR-GFP (↑ HuR) vs Control siRNA	24.0	3.1	Yes
Untransfected vs HuR siRNA (↓ HuR)	27.3	3.6	Yes
Control siRNA vs HuR siRNA (↓ HuR)	37.7	4.9	Yes
Control siRNA vs Untransfected	10.3	1.4	No

Table 4.16: Comparisons of the mean HuR-*poly(A)* or HuR-untargeted FMTRIP PLA frequency at varying HuR levels in HeLa cells using two-way ANOVA Holm-Sidak method. (Jung, Lifland et al. 2013)

Comparison	P	P<0.05
HuR-poly(A) vs HuR-untargeted	<0.001	Yes
HuR-GFP (↑ HuR) vs HuR siRNA (↓ HuR)	<0.001	Yes
HuR-GFP (↑ HuR) vs Untransfected	<0.001	Yes
HuR-GFP (↑ HuR) vs Control siRNA	<0.001	Yes
Untransfected vs HuR siRNA (↓ HuR)	<0.001	Yes
Control siRNA vs HuR siRNA (↓ HuR)	0.001	Yes
Control siRNA vs Untransfected	0.934	No

Table 4.17: Comparisons of the mean HuR-*poly(A)* PLA frequency between untransfected and transfected HeLa cells at each actD exposure time from 0 to 60 min using two-way ANOVA Holm-Sidak method (Untransfected: 0 min, n=23, mean=0.05, s.d.=0.04, 0.5 min, n=22, mean=0.05, s.d.=0.03, 30 min, n=21, mean=0.08, s.d.=0.05, 60 min, n=20, mean=0.50, s.d.=0.19; Transfected: 0 min, n=23, mean=0.21, s.d.=0.09, 0.5 min, n=26, mean=0.58, s.d.=0.09, 30 min, n=21, mean=1.66, s.d.=1.0, 60 min, n=32, mean=2.06, s.d.=0.81). (Jung, Lifland et al. 2013)

Actinomycin D Exposure (min)	Comparison	P	P<0.05
0	Untransfected vs Transfected	0.275	No
0.5	Untransfected vs Transfected	<0.001	Yes
30	Untransfected vs Transfected	<0.001	Yes
60	Untransfected vs Transfected	<0.001	Yes

Table 4.18: Comparisons of the mean HuR-*poly(A)* PLA frequency in untransfected HeLa cells between 0, 0.5, 30 and 60 min actD exposure using two-way ANOVA Holm-Sidak method (Untransfected: 0 min, n=23, mean=0.05, s.d.=0.04, 0.5 min, n=22, mean=0.05, s.d.=0.03, 30 min, n=21, mean=0.08, s.d.=0.05, 60 min, n=20, mean=0.50, s.d.=0.19). (Jung, Lifland et al. 2013)

Comparison	P	P<0.05
60 min vs 0 min	0.031	Yes
60 min vs 0.5 min	0.028	Yes
60 min vs 30 min	0.039	Yes
30 min vs 0.5 min	0.998	No
30 min vs 0 min	0.983	No
0 min vs 0.5 min	0.992	No

Table 4.19: Comparisons of the mean HuR-*poly(A)* PLA frequency in transfected HeLa cells between 0, 0.5, 30 and 60 min actD exposure using two-way ANOVA Holm-Sidak method (Transfected: 0 min, n=23, mean=0.21, s.d.=0.09, 0.5 min, n=26, mean=0.58, s.d.=0.09, 30 min, n=21, mean=1.66, s.d.=1.0, 60 min, n=32, mean=2.06, s.d.=0.81). (Jung, Lifland et al. 2013)

Comparison	P	P<0.05
60 min vs 0 min	<0.001	Yes
60 min vs 0.5 min	<0.001	Yes
60 min vs 30 min	<0.001	Yes
30 min vs 0.5 min	<0.001	Yes
30 min vs 0 min	0.007	Yes
0 min vs 0.5 min	0.008	Yes

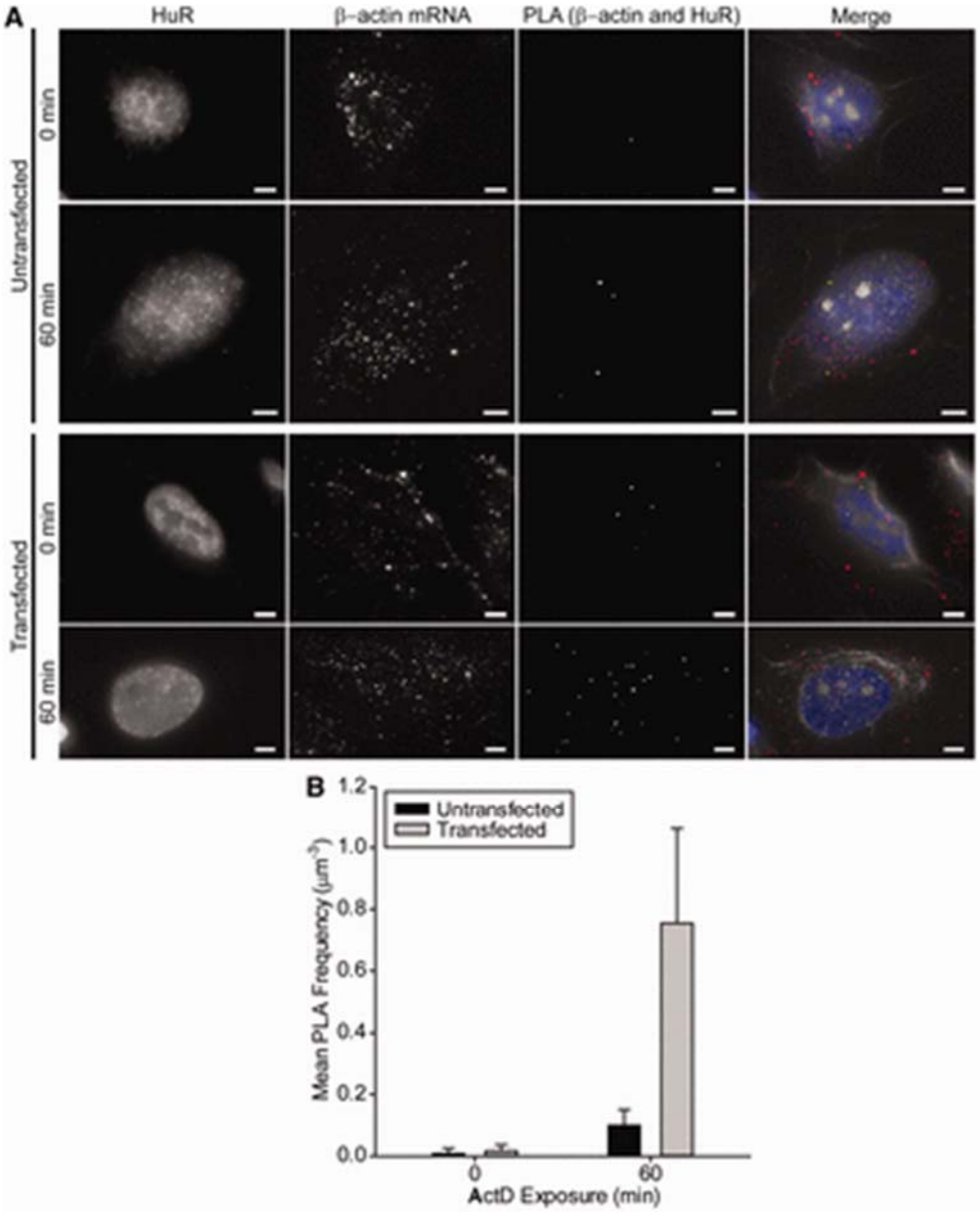

Figure 4.6: Imaging and quantification of interactions between HuR and *β-actin* 3′-UTR in HuR-GFP transfected and untransfected HeLa cells exposed to actD for 0 and 60 min. (A) HuR IF, *β-actin* mRNA and PLA between *β-actin* 3′-UTR and HuR were imaged in untransfected and transfected HeLa cells exposed to actD for 0 and 60 min, using a widefield microscope. Merged images of vimentin IF (white), *β-actin* mRNA (red), PLA (green) and HuR IF (blue) are shown. The images have been deconvolved, except for HuR and vimentin IF. Scale bar, 5 μm. (B) The mean HuR-*β-actin* 3′-UTR PLA frequency increased with longer exposure to actD in untransfected and transfected HeLa cells (Tables 4.20-4.22 for two-way ANOVA test with Holm–Sidak method) Error bars, SD. (Jung, Lifland et al. 2013)

Table 4.20: Comparisons of the mean HuR-*β-actin* 3′UTR PLA frequency between untransfected and transfected HeLa cells at 0 and 60 min actD exposure using two-way ANOVA Holm-Sidak method (Untransfected: 0 min, n=24, mean=0.008, s.d.=0.018, 60 min, n=27, mean=0.100, s.d.=0.052; Transfected: 0 min, n=19, mean=0.017, s.d.=0.020, 60 min, n=23, mean=0.755, s.d.=0.308). (Jung, Lifland et al. 2013)

Actinomycin D Exposure (min)	Comparison	P	P<0.05
0	Untransfected vs Transfected	0.858	No
60	Untransfected vs Transfected	<0.001	Yes

Table 4.21: Comparisons of the mean HuR-*β-actin* 3′UTR PLA frequency in untransfected HeLa cells between 0 and 60 min actD exposure using two-way ANOVA Holm-Sidak method (Untransfected: 0 min, n=24, mean=0.008, s.d.=0.018, 60 min, n=27, mean=0.100, s.d.=0.052). (Jung, Lifland et al. 2013)

Comparison	P	P<0.05
60 min vs 0 min	0.040	Yes

Table 4.22: Comparisons of the mean HuR-*β-actin* 3′UTR PLA frequency in untransfected HeLa cells between 0 and 60 min actD exposure using two-way ANOVA Holm-Sidak method (Transfected: 0 min, n=19, mean=0.017, s.d.=0.020, 60 min, n=23, mean=0.755, s.d.=0.308). (Jung, Lifland et al. 2013)

Comparison	P	P<0.05
60 min vs 0 min	<0.001	Yes

Materials and methods

Flag-tagged neutravidin was synthesized by first conjugating flag tag-hyNic (Solulink) to neutravidin (Thermo) modified with 4FB (Solulink) using the manufacturer's protocol. The concentration of flag tag-hyNic and 4FB-modified neutravidin were adjusted to produce molar ratio (MR) of 1-2 flag/neutravidin. After flag labelling, FMTRIPs were assembled as previously described (Santangelo, Lifland et al. 2009). Briefly, 2′-*O*-methyl RNA–DNA oligonucleotide chimeras were designed with a 5′-biotin and dT-C6-NH2 internal modifications (Biosearch Technologies). Cy3B-NHS ester fluorophores (GE Healthcare) were conjugated to the oligonucleotide amine groups using the manufacturer's protocol. Free dye was removed using 3 kD Amicon spin columns (Millipore). The purified, labelled oligonucleotides were then tetramerized by incubation for 1 h at RT with flag-tagged neutravidin at molar ratio of 5:1. The FMTRIP targeting different mRNA sequences (**Table 4.23**) were assembled separately prior to delivery. Each neutravidin, tetramerized oligonucleotides that target the same sequence. For example, in order to deliver 20 nM FMTRIP for each of three targets in β-actin 3′-UTR, 20 nM FMTRIP was incubated with 100 nM fluorophore-labelled oligonucleotide that encodes one of three sequences. Free ligands were removed using 30 kD Amicon spin columns (Millipore). Three 20 nM FMTRIP, each neutravidin bound to four of the same oligonucleotide sequences, were combined to form a 60 nM FMTRIP mixture.

HeLa cells (ATCC CCL-2) were maintained in High Glucose Dulbecco's modified Eagle's medium (DMEM) (Lonza) with 10% FBS (Hyclone), 100 U/ml penicillin (Invitrogen) and 100 μg/ml streptomycin (Invitrogen). Cells were plated on No 1.5 glass coverslips (Ted Pella) 1 day prior to infection, transfection or imaging.

Cells were transfected using Lipofectamine 2000 Transfection Reagent (Invitrogen) according to the manufacturer's protocol. For each well in a 24-well plate, Vero cells were transfected with 1.0 μg of N-GFP plasmid (a gift from Dr James E. Crowe Jr, Vanderbilt Univ.) and 2 μl Lipofectamine 2000. After 36 h of transfection, FMTRIPs were delivered into cells. For experiments using c-Myc 3′-UTR plasmids, Vero cells were transfected with 0.8 μg GFP-c-Myc plasmid and 1.6 μl Lipofectamine 2000, and 0.4 μg of HuR-GFP plasmid and 0.8 μl Lipofectamine 2000 (the plasmids were gifts from Dr Myriam Gorospe, NIH/NIA). After 48 h of transfection, FMTRIPs were delivered into cells. HeLa cells were transfected with 0.4 μg of HuR-GFP plasmid (a gift from Dr Myriam Gorospe, NIH/NIA) and 0.8 μl Lipofectamine 2000. After 36 h of transfection, FMTRIPs were delivered into cells. For siRNA transfections, HeLa cells were transfected with 200 nM On-TARGETplus Non-targeting siRNA #1 or On-TARGET SMARTpool HuR siRNA (Thermo Scientific Dharmacon) and 1 μl Lipofectamine 2000. After 48 h of transfection, FMTRIPs were delivered into cells.

For probe delivery, cells were washed in Dulbecco's phosphate buffered saline (DPBS) without $Ca^{2+}$and Mg^{2+} (Lonza), and then incubated with 0.2 U/ml activated SLO (Sigma) in OptiMEM (Invitrogen) containing FMTRIP [30nM, 60 nM or 20nM flag-tagged neutravidin targeted to hRSV, poly(A) or each of 3 β-actin 3′-UTR, respectively] for 10 min at 37°C. Delivery media were replaced with growth media for 15 min to restore membrane integrity before actD exposure or fixation. For studying hRSV infection, FMTRIPs with a 1 flag MR were used, unless otherwise specified. For experiments investigating HuR–mRNA interactions in HeLa cells, FMTRIPs with a 2 MR were used to maximize the signal.

Cells were incubated for 0.5, 30 and 60 min at 37°C with 5 μg/ml actD (Sigma) in growth medium and fixed at the end of exposure.

After probe delivery and recovery, cells were fixed with 1% paraformaldehyde (Electron Microscopy Science) in PBS for 10 min, permeabilized using 0.2% Triton X-100 (Sigma) for 5 min and blocked for 1 h with the standard Duolink II blocking solution (Olink Bioscience) or a modified blocking solution, which consists of 0.5% Tween-20 (CalBioChem), 0.1% Triton X-100, 0.1% gelatin (Aurion), 2% donkey serum (VWR) and 1% bovine serum albumin (BSA) (EMD) in PBS. Cells were washed with PBS for 5 min. Then they were incubated for 30 min at 37°C in each of two primary antibodies (Ab) diluted in 0.25% gelatin, 0.5% Triton X-100, 0.5% donkey serum and 1% BSA in PBS and then corresponding oligonucleotide-labelled PLA probes (Olink Bioscience) diluted in 0.05% Tween-20 in PBS. They were washed with Duolink wash solution (Olink Bioscience) after each Ab incubation. The ligation and RCA reactions (Olink Bioscience) were performed as instructed in the manufacturer's protocol. Then the cells were immunostained or DAPI-stained (Invitrogen) and mounted on slides using Prolong (Invitrogen).

Primary antibodies used were mouse monoclonal anti-flag (1:500 for immunofluorescence (IF), 1:1000 for PLA, Sigma), rabbit polyclonal anti-flag (1:500 for IF, 1:1000 for PLA, Sigma), mouse monoclonal anti-HuR 3A2 (1:6000 for PLA, Santa Cruz), mouse monoclonal anti-HuR 19F12 (1:200 for IF, Santa Cruz) and mouse monoclonal anti-vimentin (1:50 for IF, Developmental Studies Hybridoma Bank). Rabbit polyclonal anti-flag Ab (Sigma) was used unless otherwise specified.

Unless specified otherwise, all the images were taken using a laser scanning confocal microscope, Zeiss LSM 510 Meta using a 63×, NA 1.4 Plan-Apochromat objective. Resolution was set to 1024 × 1024. Files were imported into Volocity and linearly contrast enhanced for display. Widefield images were taken on an Axiovert 200 M microscope (Zeiss) with a 63× numerical aperture (NA) 1.4 Plan-Apochromat objective, and an ORCA-ER AG camera (Hamamatsu). The imaging was performed using the Volocity acquisition software (PerkinElmer). Image stacks were recorded at 200 nm intervals to adequately sample volumes for iterative deconvolution.

Widefield images were deconvolved using Volocity's deconvolution algorithms. FMTRIP and PLA signal quantification, intensity quantification, as well as Mander's and Pearson's coefficients were computed in Volocity and imported into Excel (Microsoft) or Sigma Plot (Systat) for further analysis and plotting. Images presented have been linearly contrast enhanced for clarity. All calculations were performed directly on raw, deconvolved widefield data or raw confocal data.

The volume of RNA and the PLA frequency/RNA volume were measured using Volocity. Each cell was analysed individually as follows. Each cell was identified by MTRIP signal or vimentin immunostaining. The RNA volume was determined based on the SD intensity. The PLA signal initially was identified as PLA objects by their SD intensity, then separated into individual punctae using the 'separate touching objects' tool. The objects were further filtered based on size and maximum intensity. For each experiment, we analysed at least 30 representative cells; experiments were repeated at least twice. In Sigma Plot, Mann–Whitney rank sum test was used to compare FMTRIP volume and the Pearson's and Manders' coefficients; one-way and two-way ANOVA

statistical tests were performed to compare PLA frequency. For one-way ANOVA test, multiple pairwise comparisons were performed with Dunn's method for unequal number of samples and Tukey method for equal number of samples. For two-way ANOVA test, multiple pairwise comparisons were performed with Holm–Sidak.

HeLa cells were grown on six-well plates and transfected as described with 2 µg of HuR-GFP plasmid per well. After 36 h post-transfection, they were exposed to actD. At the end of the exposure, total RNA was extracted at the indicated time points using the PARIS kit (Ambion). Total RNA was quantified via UV-VIS spectroscopy. A quantity of 1 µg total RNA was used for cDNA synthesis using the RT^2 first strand kit (SA biosciences) according to the manufacturer's instructions. About 1 µl of the product then was used for Quantitative reverse transcriptase polymerase chain reaction (qRT–PCR) using the Real-time RT^2 qPCR primer assay (SYBR green) in the presence of gene-specific primers for ACTB and 18S rRNA (SA Biosciences). qRT–PCR was performed with three replicates using ABI StepOnePlus real-time PCR system (Applied Biosciences). The relative quantification (RQ) of gene expression and comparative threshold cycle (C_T) values were obtained using an ABI StepOnePlus real-time PCR system. The values were compared with the untransfected cells with no actD exposure. Here, 18S rRNA was used as the internal control (Student's *t*-test: $P = 0.0995$). These values and their summary statistics were used to compare the effects of actD exposure in the transfected and untransfected groups (Schmittgen and Livak 2008). Two-way ANOVA test was performed using the summary statistics provided, and the Bonferroni *post-hoc* method was used to compare the groups.

Table 4.23: FMTRIP sequences and modifications. (Jung, Lifland et al. 2013)

Target	Ligand	Location within transcript
hRSV gRNA	5′-biotin-**U**XTXTTX**AAAAAXGGGGCAAAXAA**-3′	39-55;590-606;2323-2339
c-Myc 3′UTR A 1	5′-biotin-TXTTTT**GAAXCGUXUUCCXUACUXUUC**-3′	1892-1912
c-Myc 3′UTR A 2	5′-biotin-TXTTTT**CAAGXUCAXAGGXGAUXGCUC**-3′	1932-1952
c-Myc 3′UTR A 3	5′-biotin-TXTTTT**GGXUGXGAGGXUGCAUXUG**-3′	1968-1986
Untargeted	5′-biotin-XTTXTTX**UAG**X**AGU**X**CC**X**GC**X**AUG**X**CAC**-3′	
Poly(A)	5′-biotin-TXTTTT**UXUUUUUUXUUUUUUXUU**-3′	
β-actin 3′UTR 1	5′-biotin-TXTTTTX**UCCUG**X**AACAA**X**GCAUC**XC-3′	1479-1461
β-actin 3′UTR 2	5′-biotin-TXTTTTX**AAGCCC**X**GGC**X**GCC**X**CCA**-3′	1748-1730
β-actin 3′UTR 3	5′-biotin-TXTTTT**GXCACCU**X**CACCGU**X**CC**A**G**-3′	1377-1359
	Boldface: 2′-O-Methyl RNA; X: dT-C6-NH_2; all others are DNA; underline: binding region	

References

Abdelmohsen, K. and M. Gorospe (2010). "Posttranscriptional regulation of cancer traits by HuR." Wiley Interdiscip Rev RNA **1**(2): 214-229.

Abe, R., E. Sakashita, et al. (1996). "Two different RNA binding activities for the AU-rich element and the poly(A) sequence of the mouse neuronal protein mHuC." Nucleic Acids Res **24**(24): 4895-4901.

Anderson, P. and N. Kedersha (2002). "Visibly stressed: the role of eIF2, TIA-1, and stress granules in protein translation." Cell Stress Chaperones **7**(2): 213-221.

Blackinton, J. G. and J. D. Keene (2014). "Post-transcriptional RNA regulons affecting cell cycle and proliferation." Semin Cell Dev Biol.

Brennan, C. M. and J. A. Steitz (2001). "HuR and mRNA stability." Cell Mol Life Sci **58**(2): 266-277.

Cech, T. R. and J. A. Steitz (2014). "The noncoding RNA revolution-trashing old rules to forge new ones." Cell **157**(1): 77-94.

Chan, Y. A., P. Hieter, et al. (2014). "Mechanisms of genome instability induced by RNA-processing defects." Trends Genet **30**(6): 245-253.

Dormoy-Raclet, V., I. Menard, et al. (2007). "The RNA-binding protein HuR promotes cell migration and cell invasion by stabilizing the beta-actin mRNA in a U-rich-element-dependent manner." Mol Cell Biol **27**(15): 5365-5380.

Fan, X. C. and J. A. Steitz (1998). "HNS, a nuclear-cytoplasmic shuttling sequence in HuR." Proc Natl Acad Sci U S A **95**(26): 15293-15298.

Fan, X. C. and J. A. Steitz (1998). "Overexpression of HuR, a nuclear-cytoplasmic shuttling protein, increases the in vivo stability of ARE-containing mRNAs." EMBO J **17**(12): 3448-3460.

Jung, J., A. W. Lifland, et al. (2013). "Quantifying RNA-protein interactions in situ using modified-MTRIPs and proximity ligation." Nucleic Acids Res **41**(1): e12.

Keene, J. D. (2007). "RNA regulons: coordination of post-transcriptional events." Nat Rev Genet **8**(7): 533-543.

Khabar, K. S. (2010). "Post-transcriptional control during chronic inflammation and cancer: a focus on AU-rich elements." Cell Mol Life Sci **67**(17): 2937-2955.

Kim, H. H., Y. Kuwano, et al. (2009). "HuR recruits let-7/RISC to repress c-Myc expression." Genes Dev **23**(15): 1743-1748.

Lal, A., T. Kawai, et al. (2005). "Antiapoptotic function of RNA-binding protein HuR effected through prothymosin alpha." EMBO J **24**(10): 1852-1862.

Lebedeva, S., M. Jens, et al. (2011). "Transcriptome-wide analysis of regulatory interactions of the RNA-binding protein HuR." Mol Cell **43**(3): 340-352.

Lifland, A. W., C. Zurla, et al. (2011). "Dynamics of native beta-actin mRNA transport in the cytoplasm." Traffic **12**(8): 1000-1011.

Lopez de Silanes, I., M. P. Quesada, et al. (2007). "Aberrant regulation of messenger RNA 3'-untranslated region in human cancer." Cell Oncol **29**(1): 1-17.

Lopez de Silanes, I., M. Zhan, et al. (2004). "Identification of a target RNA motif for RNA-binding protein HuR." Proc Natl Acad Sci U S A **101**(9): 2987-2992.

Lukong, K. E., K. W. Chang, et al. (2008). "RNA-binding proteins in human genetic disease." Trends Genet **24**(8): 416-425.

Ma, W. J., S. Cheng, et al. (1996). "Cloning and characterization of HuR, a ubiquitously expressed Elav-like protein." J Biol Chem **271**(14): 8144-8151.
Ma, W. J., S. Chung, et al. (1997). "The Elav-like proteins bind to AU-rich elements and to the poly(A) tail of mRNA." Nucleic Acids Res **25**(18): 3564-3569.
Mazan-Mamczarz, K., S. Galban, et al. (2003). "RNA-binding protein HuR enhances p53 translation in response to ultraviolet light irradiation." Proc Natl Acad Sci U S A **100**(14): 8354-8359.
Misquitta, C. M., V. R. Iyer, et al. (2001). "The role of 3'-untranslated region (3'-UTR) mediated mRNA stability in cardiovascular pathophysiology." Mol Cell Biochem **224**(1-2): 53-67.
Mukherjee, N., D. L. Corcoran, et al. (2011). "Integrative regulatory mapping indicates that the RNA-binding protein HuR couples pre-mRNA processing and mRNA stability." Mol Cell **43**(3): 327-339.
Pelkmans, L. (2012). "Cell Biology. Using cell-to-cell variability--a new era in molecular biology." Science **336**(6080): 425-426.
Peng, S. S., C. Y. Chen, et al. (1998). "RNA stabilization by the AU-rich element binding protein, HuR, an ELAV protein." EMBO J **17**(12): 3461-3470.
Santangelo, P. J., A. W. Lifland, et al. (2009). "Single molecule-sensitive probes for imaging RNA in live cells." Nat Methods **6**(5): 347-349.
Schmittgen, T. D. and K. J. Livak (2008). "Analyzing real-time PCR data by the comparative C(T) method." Nat Protoc **3**(6): 1101-1108.
Srikantan, S. and M. Gorospe (2012). "HuR function in disease." Front Biosci (Landmark Ed) **17**: 189-205.
Uren, P. J., S. C. Burns, et al. (2011). "Genomic analyses of the RNA-binding protein Hu antigen R (HuR) identify a complex network of target genes and novel characteristics of its binding sites." J Biol Chem **286**(43): 37063-37066.
Wang, H., F. Zeng, et al. (2013). "The structure of the ARE-binding domains of Hu antigen R (HuR) undergoes conformational changes during RNA binding." Acta Crystallogr D Biol Crystallogr **69**(Pt 3): 373-380.
Welch, C. M., H. Elliott, et al. (2011). "Imaging the coordination of multiple signalling activities in living cells." Nat Rev Mol Cell Biol **12**(11): 749-756.
Yeap, B. B., D. C. Voon, et al. (2002). "Novel binding of HuR and poly(C)-binding protein to a conserved UC-rich motif within the 3'-untranslated region of the androgen receptor messenger RNA." J Biol Chem **277**(30): 27183-27192.
Zurla, C., A. W. Lifland, et al. (2011). "Characterizing mRNA interactions with RNA granules during translation initiation inhibition." PLoS One **6**(5): e19727.

CHAPTER 5

POST-TRANSCRIPTIONAL REGULATION OF *PDCD4* mRNA BY HuR AND TIA1

This work has been adapted from Wigington, CP*, Jung, J*, Rye, EA, Belauret, SL, Philpot, AM, Santangelo, PJ, Corbett, AH (2014). "Post-transcriptional regulation of programmed cell death 4 (PDCD4) mRNA by the RNA binding proteins human antigen R (HuR) and T-cell intracellular antigen 1 (TIA1)." J Biol Chem, *Under revision*. *These authors contributed equally to this work.

Background

The 3′ untranslated region (3'UTR) of an mRNA transcript is the site of binding and regulation for many post-transcriptional factors. The AU-Rich Element Binding Proteins are RNA binding proteins (RBP) that bind to the AU- or U-rich RNA elements (AREs) in the 3′UTRs of target mRNAs and regulate them. This family of proteins include human antigen R (HuR), and T-cell Intracellular Antigen 1 (TIA1) and regulate the expression of numerous mRNAs (Dixon, Balch et al. 2003; Abdelmohsen and Gorospe 2010; Subramaniam, Ooi et al. 2010).

mRNAs bound to HuR in the cytoplasm usually have greater stability and increased translation (Brennan and Steitz 2001). However, HuR can also increase the expression of target transcripts without affecting their stability (Mazan-Mamczarz, Galban et al. 2003; Lal, Kawai et al. 2005) possibly via coordinating with translational repressors, such as TIA1 (Kawai, Lal et al. 2006). TIA1 generally inhibits the translation

(Forch and Valcarcel 2001). TIA1 contains three tandem RRMs at the N-terminus of the protein followed by a glutamine-rich C-terminal domain (Kawakami, Tian et al. 1992). RRM2 of TIA1 has specificity for U-rich RNA and allows for high affinity binding to the intronic and 3′UTR regions (Dember, Kim et al. 1996; Wang, Kayikci et al. 2010). TIA1 is present in both the nucleus and the cytoplasm and can shuttle between the two compartments (Kedersha, Cho et al. 2000; Zhang, Delestienne et al. 2005). Similar to HuR, TIA1 localization shifts toward the cytoplasm upon oxidative stress and transcriptional inhibition (Zhang, Delestienne et al. 2005). During oxidative stress, TIA1 binding to the 3′UTR of target mRNAs promotes the compartmentalization of translationally incompetent preinitiation complexes into stress granules, resulting in translational repression (Anderson and Kedersha 2002).

Transcriptome-wide analyses of both HuR and TIA1 binding reveal a variety of mRNAs that can bind to these RBPs (Wang, Kayikci et al. 2010; Kishore, Jaskiewicz et al. 2011; Lebedeva, Jens et al. 2011; Mukherjee, Corcoran et al. 2011; Uren, Burns et al. 2011). HuR may potentially bind to approximately 10% of the transcriptome, specifically within the 3′UTR and introns. These analyses show HuR binding to the U-rich sequences with a greater affinity than the AU-rich regions, contradicting the conventional assumption about HuR binding (Kishore, Jaskiewicz et al. 2011; Lebedeva, Jens et al. 2011; Mukherjee, Corcoran et al. 2011; Uren, Burns et al. 2011). Secondary structural predictions of HuR binding sites suggest a preference for single-stranded RNA for binding to HuR, specifically within a loop (Lopez de Silanes, Zhan et al. 2004; Uren, Burns et al. 2011). A recent TIA1 iCLIP study reveals a high degree of TIA1 binding to U-rich regions found within the 3′UTR (Wang, Kayikci et al. 2010). With the U-rich

regions as potential targets for both HuR and TIA1, they may compete if an mRNA has limited U-rich regions in the 3'UTR or potentially cooperate if otherwise.

These transcriptome-wide studies validate the binding sites of many well-characterized HuR targets, including the cell cycle regulators, cyclin A, B1, D1 and E1 (Wang, Caldwell et al. 2000; Lal, Mazan-Mamczarz et al. 2004; Guo and Hartley 2006), p53 (Mazan-Mamczarz, Galban et al. 2003; Pryzbylkowski, Obajimi et al. 2008), and Estrogen Receptor α (ERα) (Pryzbylkowski, Obajimi et al. 2008). Additionally, HuR has been found to regulate many apoptotic factors, such as Prothymosin α (Lal, Kawai et al. 2005), cytochrome c (Kawai, Lal et al. 2006), Bcl-2 and Mcl-1 (Abdelmohsen and Gorospe 2010). Similarly, TIA1 also regulates apoptotic mRNAs, including the Tumor Necrosis Factor α mRNA (TNF-α) (Piecyk, Wax et al. 2000; Forch and Valcarcel 2001). These studies suggest a potential role for HuR and TIA1 in coordinating the apoptotic program (Abdelmohsen and Gorospe 2010).

HuR and TIA1 regulate several cancer-relevant targets. Programmed Cell Death 4 (*PDCD4*) is a tumor suppressor that was identified in transcriptome-wide analyses. The PDCD4 protein inhibits the activity of the eukaryotic translation initiation factor 4A (eIF4A) (Yang, Jansen et al. 2003), which is an RNA helicase responsible for unwinding the secondary structure in the 5′UTRs of translating mRNAs (Rogers, Richter et al. 1999). Decreased PDCD4 protein levels, observed in a number of cancer types (Lankat-Buttgereit and Goke 2009), increases protein production and tumor promotion (Cmarik, Min et al. 1999; Yang, Jansen et al. 2003). PDCD4 may be a key regulator of global translational levels and likely regulated by multiple factors.

The oncomiR, *miR-21*, which is overexpressed in almost all cancer types studied (Pan, Wang et al. 2010), regulates *PDCD4* by binding to its 3′UTR and reducing its protein levels (Asangani, Rasheed et al. 2008; Frankel, Christoffersen et al. 2008). *PDCD4* expression also is regulated at the transcriptional (Leupold, Asangani et al. 2012; Vikhreva, Shepelev et al. 2014) and post-translational levels (Dorrello, Peschiaroli et al. 2006; Lankat-Buttgereit and Goke 2009; Powers, Fay et al. 2011). The transcriptome-wide sequencing analyses of HuR and TIA1 suggest that they may bind to *PDCD4* mRNAs. These RBPs may serve as additional post-transcriptional regulators of PDCD4 expression.

In this study, we extensively demonstrated the *PDCD4* mRNA as a novel target of HuR and TIA1 in a breast cancer cell line, MCF-7 (Soule, Vazguez et al. 1973). In addition to RNA-immunoprecipitation (RNA-IP) with HuR and TIA1, we employed RNA-imaging probes deliverable to live cells (Santangelo, Lifland et al. 2009) and proximity ligation assay (PLA) (Soderberg, Gullberg et al. 2006; Jung, Lifland et al. 2013) to examine the interplay between HuR and TIA1 on the *PDCD4* transcripts with single-interaction sensitivity on a per cell basis. Contrary to previous studies that describe a cooperative relationship between HuR and TIA1 in binding to *cytochrome C* mRNA (Kawai, Lal et al. 2006), we demonstrate that HuR and TIA1 compete for interaction with *PDCD4* transcripts, likely via shared binding sites in the 3′UTR. This competitive interplay between the two RBPs may be a novel mechanism for fine-tuning the level of PDCD4 protein.

***PDCD4* mRNA is a candidate target of HuR**

Many transcriptome-wide PAR-CLIP studies in HeLa and HEK293 cells reveal novel functions and potential targets of HuR (Kishore, Jaskiewicz et al. 2011; Lebedeva, Jens et al. 2011; Mukherjee, Corcoran et al. 2011; Uren, Burns et al. 2011), including potential tumorigenic targets. One such candidate transcript is *PDCD4*, which encodes a tumor suppressor that inhibits neoplastic transformation by interfering with the helicase activity of eIF4A (Yang, Jansen et al. 2003). The *PDCD4* mRNA contains multiple predicted AREs (Gruber, Fallmann et al. 2011) within the 3′UTR as well as CLIP-Seq tags from HuR-CLIP studies, suggesting that it is a candidate target of HuR.

To assess whether HuR binds to *PDCD4* mRNA in MCF-7 breast cancer cells, CP Wigington performed RNA immunoprecipitation (RNA-IP) with endogenous HuR protein. As expected, HuR protein was detected in the bound fraction when purified with HuR antibody but not with IgG control antibody (**Figure 5.1A**). The input and bound fractions were then analyzed for the presence of bound *PDCD4* transcript using qRT-PCR. As shown in **Figure 5.1B**, the *PDCD4* transcript was robustly enriched with HuR. As controls, she also examined a known HuR target, Estrogen Receptor α (ERα) (Pryzbylkowski, Obajimi et al. 2008), as well as *GAPDH*, which is not bound by HuR (Lopez de Silanes, Zhan et al. 2004). As expected, the *GAPDH* transcript showed no enrichment with HuR; however, the previously defined HuR target, *ERα* (Pryzbylkowski, Obajimi et al. 2008), showed enrichment. These results provide evidence that HuR binds to *PDCD4* mRNA in MCF-7 cells.

HuR RRMs 1 and 2 are required for *PDCD4* binding

CP Wigington identified that the HuR protein contains three RRMs (**Figure 5.2A**). The two N-terminal RRMs are critical for ARE recognition while the third RRM is thought to recognize polyadenosine sequences (Abe, Sakashita et al. 1996; Ma, Chung et al. 1997). The crystal structure of RRMs 1 and 2 (residues 18-186) of HuR in complex with an AUUUUUUAUUUU RNA oligomer (PDB # 4ED5) (Wang, Zeng et al. 2013) is shown in **Figure 5.2A**. While RRM1 is the primary ARE recognition domain within HuR, the conformational change that takes place upon RNA binding leads to additional interactions between RRM2 and the target mRNA, ultimately increasing RNA binding affinity (Wang, Zeng et al. 2013). This structure, along with other studies examining the structural basis of HuR-RNA interactions (Wang, Li et al. 2011), illustrates important key residues that are predicted to be crucial for high affinity RNA-binding by HuR (Wang, Li et al. 2011; Wang, Zeng et al. 2013).

To define specific residues within RRM1 and 2 that are critical for HuR binding to target RNA, we focused on three of the residues (asparagine 21 [N21], tyrosine 109 [Y109] and arginine 147 [R147]) shown *in vitro* to be critical for RNA binding (Wang, Li et al. 2011). CP Wiginton changed each of these residues to alanine in an N-terminally FLAG-tagged HuR expression vector to create a FLAG-HuR binding mutant, which she term FLAG-HuR(BM). To ensure that FLAG-HuR(BM) is expressed at comparable levels to the wild type FLAG-HuR, she transfected MCF-7 cells with the FLAG-HuR and -HuR(BM) constructs and analyzed expression by immunoblotting for HuR (**Figure 5.2B**). HuR antibody detects both endogenous HuR (lower band) and FLAG-tagged HuR protein (upper band). The steady-state level of FLAG-HuR protein is comparable for HuR and HuR(BM), demonstrating that the amino acid changes within the RRM do not

significantly impact the steady-state level of HuR protein. Importantly, the localization of HuR(BM) is also indistinguishable from HuR(WT) as assessed by indirect immunofluorescence (**Figure 5.1C**).

To test whether the residues altered in HuR(BM) are critical for HuR binding to target mRNA, she expressed FLAG-HuR and -HuR(BM) in MCF-7 cells and subjected these cell lysates to RNA-IP analysis. To ensure specific purification of FLAG-tagged HuR, she performed the RNA-IP with FLAG antibody-conjugated protein A beads. As shown in **Figure 5.2C**, CP Wigington achieved robust purification of both FLAG-HuR and -HuR(BM) with no purification of the untagged, endogenous HuR protein. To identify RNA transcripts that co-purify with the FLAG-tagged HuR proteins, qRT-PCR analysis was performed (**Figure 5.2D**). As expected, the well-studied HuR target, *ERα* (Pryzbylkowski, Obajimi et al. 2008), was robustly enriched upon purification of FLAG-HuR. Significantly reduced enrichment of the *ERα* transcript was detected with FLAG-HuR(BM) as compared to WT FLAG-HuR, providing the first evidence that these key residues within HuR RRM1 and RRM2 are important for interaction with HuR target RNA in cells and demonstrating the utility of this mutant for validating ARE-containing HuR target RNAs. As expected, the negative control transcript, *RPLP0*, did not enrich with either FLAG-HuR or -HuR(BM).

CP Wiginton next exploited the HuR(BM) to assess whether *PDCD4* binding depends on HuR RRMs 1 and 2, as established for the ARE-containing *ERα* transcript. She analyzed *PDCD4* mRNA enrichment with both FLAG-HuR and -HuR(BM). Consistent with the results from the endogenous HuR RNA-IP, she observed robust enrichment of the *PDCD4* transcript upon purification of wild type HuR. In contrast, no

significant enrichment of *PDCD4* was detected in the HuR binding mutant sample. The loss of enrichment of the *ERα* and *PDCD4* transcripts with FLAG-HuR(BM) demonstrate that *PDCD4* binding to HuR is similar to that of the classical ARE-containing target, *ERα*.

HuR binds to two distinct regions within the *PDCD4* 3'UTR

Previous CLIP-Seq studies examining HuR binding across the transcriptome reveal that HuR binds primarily within the 3′UTRs and introns of mRNAs. Additional preliminary data from these CLIP-Seq studies show that the 3′UTR of the PDCD4 transcript contains multiple AU- and U-rich stretches that could be bound by HuR. (Kishore, Jaskiewicz et al. 2011; Lebedeva, Jens et al. 2011; Mukherjee, Corcoran et al. 2011; Uren, Burns et al. 2011) The UCSC Genome Browser defines the *PDCD4* 3′UTR as being 1,918 nt long; however, data from poly(A)-Seq analyses in various human tissues suggest that an evolutionarily conserved upstream polyadenylation site may be used for 3′ end processing of the *PDCD4* transcript, resulting in a 3′UTR of approximately 672 nt. To determine the precise length of the *PDCD4* 3′UTR in MCF-7 cells, CP Wigington performed 3′ RACE analysis using primers specific to the *PDCD4* 3′UTR. The *GAPDH* 3′UTR was used as a control. To define the size of the *PDCD4* 3′UTR in two other human cancer cell lines, she also performed 3′ RACE analyses using cDNA from HeLa (cervical adenocarcinoma; ATCC CCL-2) and MDA-MB-231 (mammary adenocarcinoma; ATCC HTB-26) cells. As shown in **Figure 5.3A** and verified by sequence analysis, the 3′UTR of *PDCD4* is 672 nucleotides in all cell types analyzed. These results focus our analysis of post-transcriptional regulation of *PDCD4* on the 672 nt 3′UTR present in MCF-7 cells.

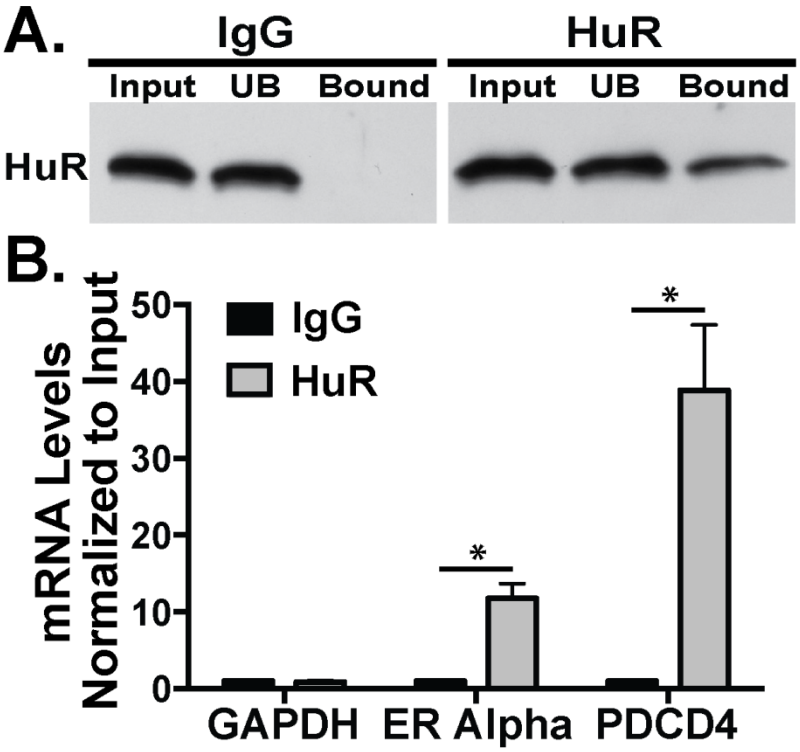

FIGURE 5.1: HuR RNA-IP in MCF-7 cells enriches for *PDCD4* mRNA. Endogenous HuR protein was immunoprecipitated from MCF-7 cells using either HuR antibody-coated protein A beads or isotype control Mouse IgG-coated beads. (A) Proteins from the Input, unbound (UB) and Bound fractions were resolved on an SDS-PAGE gel and subjected to immunoblotting with HuR antibody. HuR was detected in the HuR bound fraction but not the IgG bound fraction. (B) RNA isolated from the HuR RNA-IP was subjected to qRT-PCR analyses with *GAPDH*, *ER Alpha* and *PDCD4* primers. mRNA levels in HuR bound fractions were normalized to input levels and then compared by fold-enrichment over IgG control. Significant enrichment of *ERα* and *PDCD4* transcripts was observed with HuR IP. Values represent the mean ± SEM for n=3 independent experiments. *represents $p<0.05$. (Wigington, Jung et al. 2014)

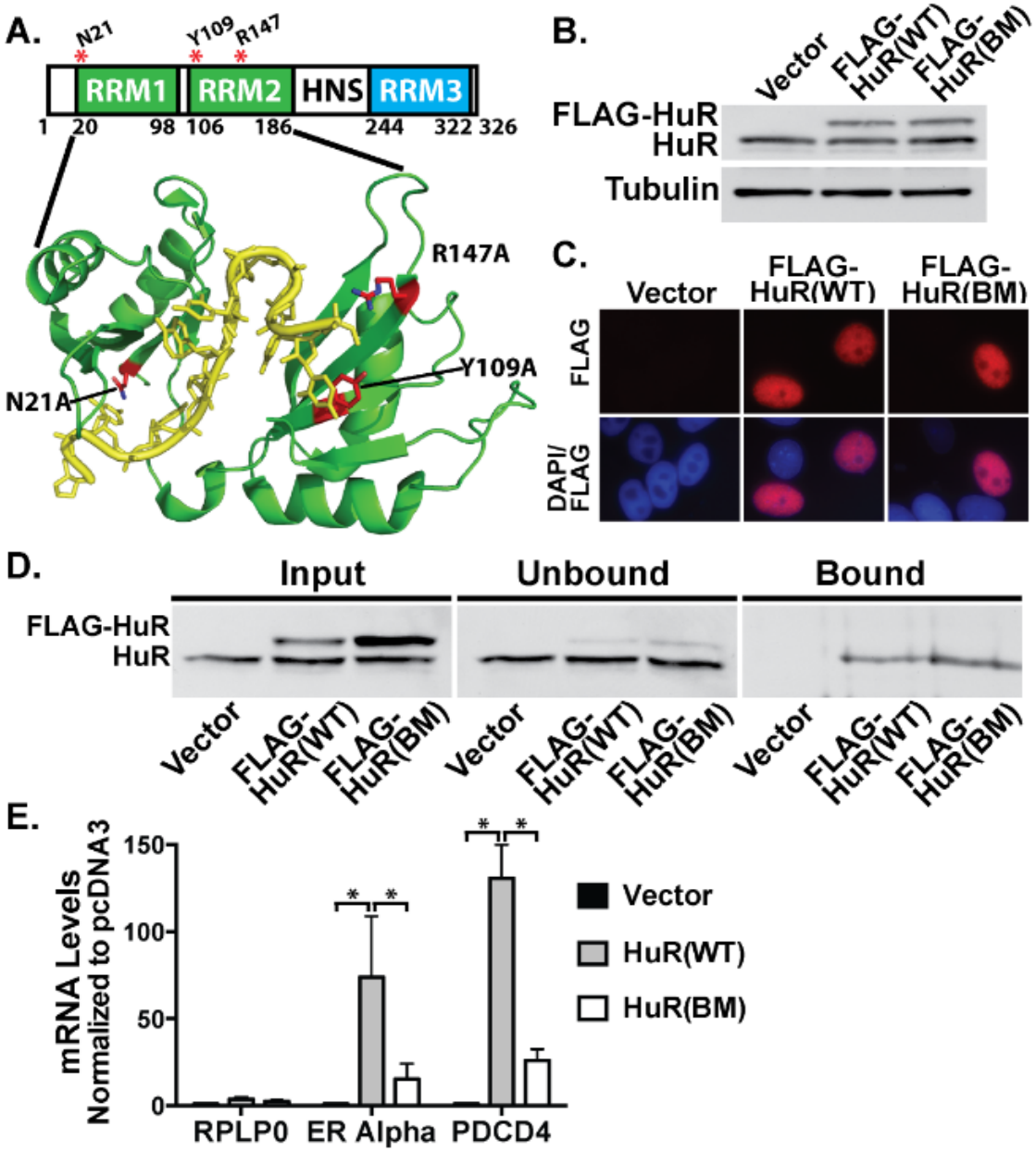

FIGURE 5.2: Key residues in HuR RRMs 1 and 2 are required for binding to ARE-containing target mRNAs, including *PDCD4*. (A) The HuR protein contains three RRMs (RRM1, RRM2 and RRM3) and a HuR Nucleocytoplasmic Shuttling sequence (HNS), which mediates bidirectional transport of HuR between the nucleus and cytoplasm. The two N-terminal RRMs (green) are responsible for ARE recognition while the C-terminal RRM (blue) is thought to bind to the poly(A) tail of mRNA transcripts. Shown below the linearized map of HuR is a recently solved co-crystal structure (PDB # 4ED5) of HuR RRMs 1 and 2 (green) in complex with an AUUUUUUAUUUU RNA oligomer (yellow). Residues shown to be important for RNA recognition in *in vitro* binding studies are highlighted in red (N21, Y109 and R147). A putative HuR RNA

binding mutant (BM) was generated by changing these residues to alanine in a FLAG-tagged HuR expression construct. (B) MCF-7 cells were transfected with vector control, FLAG-HuR(WT) or -HuR(BM) plasmids and subjected to immunoblotting with HuR and Tubulin antibodies. FLAG-HuR proteins were detected only in FLAG-transfected cells and levels of BM are comparable to WT. (C) Transfected MCF-7 cells were analyzed by indirect immunofluorescence with FLAG antibody to detect FLAG-HuR(WT) or (BM). Colocalization with DAPI reveals steady-state nuclear localization of both FLAG-HuR proteins (WT and BM). (D) Cells expressing vector control or FLAG-HuR proteins were subjected to RNA-IP using FLAG antibody-conjugated beads. Immunoblot analysis of IP samples demonstrates specific enrichment of FLAG-HuR proteins in bound fractions. (E) RNA that co-precipitated with FLAG-HuR proteins was subjected to qRT-PCR analyses with *RPLP0*, *ER Alpha* and *PDCD4* primers to detect bound transcripts. *ER Alpha* and *PDCD4* transcripts were significant enriched upon wildtype HuR purification; however, a significant decrease in enrichment was observed upon purification of HuR binding mutant. mRNA levels in FLAG-HuR-bound fractions were normalized to input levels and then compared by fold-enrichment over vector control samples. Values represent the mean ± SEM for n=3. * represents $p<0.05$. (Wigington, Jung et al. 2014)

To determine whether HuR binds to the 3′UTR of *PDCD4*, she generated a biotinylated RNA probe that corresponds to the 672 nt region of the *PDCD4* 3′UTR. As controls, she employed the *c-Myc* 3′UTR, which is a well-defined target of HuR (Ma, Cheng et al. 1996) and the *GAPDH* 3′UTR, which is not a HuR target (**Figure 5.3B**). The biotinylated probes were incubated with MCF-7 cell lysates, precipitated by neutravidin-coated beads, and then subjected to immunoblot analysis with HuR antibody to detect HuR bound to the probes. As shown in Figure 3C, HuR protein was readily detected in the input fractions, verifying the presence of HuR protein in these cell lysates. She detected robust HuR binding to the full-length *PDCD4* 3′UTR probe, suggesting that HuR binds to the 3′UTR of *PDCD4*. As expected, she detected HuR protein bound to the *c-Myc* 3′UTR probe but not samples without a probe or with the negative control *GAPDH* 3'UTR probe. These results confirm that HuR binds to the 3′UTR of *PDCD4* mRNA.

To define specific regions of the *PDCD4* 3′UTR that allow HuR binding, CP Wigington generated a set of biotinylated probes that correspond to the first 290 and final 382 nucleotides of the *PDCD4* 3′UTR (5′290 and Δ290 probes, respectively; **Figure 5.3B**). As shown in **Figure 5.3C**, she detected robust HuR binding to the 5′290 probe. But we did not detect HuR binding to the Δ290 probe, suggesting that HuR binds specifically to the 5′290 nucleotides of the *PDCD4* 3′UTR. Interestingly, the 5′290 nucleotides of the *PDCD4* 3′UTR contain multiple AU- and U-rich stretches to which HuR can bind (Gruber, Fallmann et al. 2011). To determine whether HuR binds to one or more of these stretches, she generated additional biotinylated probes that correspond to 100 or 90 nucleotide regions of the *PDCD4* 5′290 3′UTR region (**Figure 5.3B**; Probes A, B and C). She detected robust binding of HuR to the first two 100 nucleotide regions of

the *PDCD4* 3′UTR, but not to the third 90 nucleotides (**Figure 5.3C**). These results show two distinct HuR binding sites within the first 200 nucleotides of the *PDCD4* 3′UTR.

RNA imaging probes can be used to visualize *PDCD4* mRNA in live cells

Recent studies demonstrate the ability to accurately visualize RNA granules and RNA-protein interactions at a single molecule level in live cells (Santangelo, Lifland et al. 2009; Jung, Lifland et al. 2013). To detect HuR-*PDCD4* interactions in MCF-7 cells, we designed four imaging probes that target four different sequences in the *PDCD4* 3′ UTR, avoiding the defined HuR binding sites (HuR BS) (**Figure 5.4A**). To determine probe specificity, we delivered each probe, labeled with Cy3b fluorophores, along with the other three probes labeled with Dylight 650 fluorophores. For example, in order to examine the specificity of probe 1, probe 1 was labeled with Cy3b while probes 2, 3, and 4 were labeled with Dylight 650 (**Figure 5.4B**). Therefore, colocalization of probe 1 with the other three probes would suggest specificity of probe 1 in targeting the *PDCD4* 3′UTR.

For each probe, three images were obtained for analysis and colocalization was quantified by Mander's coefficient. The mean Mander's coefficients for probes 1-3 were greater than 0.8 and were not statistically different from one another ($p>0.9$), suggesting good colocalization. Probes 1-3 overlapped well with the other probes, as shown in the intensity profile of the representative mRNA punctae (**Figure 5.4B**). However, the mean Mander's coefficient for probe 4 was 0.6 and was significantly less than the other three probes ($p<0.009$). Generally, probe 4 did not overlap well with the other probes as shown in the intensity profile (**Figure 5.4B**). Where the probe signal was bright, the signal of the

other probes was dim or vice versa. Thus, probe 4 was deemed non-specific and was not used for further analysis and probes 1-3 were employed in all experiments. These results suggest that probes 1-3 specifically recognize the *PDCD4* 3′UTR and allow us to visualize *PDCD4* RNA granules in MCF-7 cells.

Proximity ligation assay can detect HuR-PDCD4 mRNA interactions

To visualize HuR protein-*PDCD4* mRNA interactions in MCF-7 cells, we performed proximity ligation assay (PLA) between HuR and the FLAG peptides on the *PDCD4* RNA probes. As schematized in **Figure 5.4C**, primary antibodies of different species bind to HuR and the FLAG tag (mouse and rabbit, respectively), which can then be detected by species-specific PLA probes with oligonucleotides. The oligonucleotides attached to the PLA probe form a circularized DNA strand by enzymatic ligation, one of which can serve as a primer for rolling circle amplification. This amplification ultimately results in a coiled single-stranded DNA, or the PLA product, which is complementary to the circular DNA strand. The PLA product is then detected by hybridizing complementary fluorophore labeled oligonucleotides (**Figure 5.4C**) (Soderberg, Gullberg et al. 2006; Jung, Lifland et al. 2013). As shown in **Figure 5.4D**, we observe endogenous HuR-*PDCD4* interactions by PLA in untransfected and untreated cells (top row; quantified in **Figure 5.4F**), which supports the HuR-*PDCD4* binding data obtained from both RNA-IP (**Figures 5.1** and **5.2**) and biotin pulldown analyses (**Figure 5.3**). As expected, we observed no PLA signal in cells treated with negative control probes lacking FLAG tags (NA; **Figure 5.4D**).

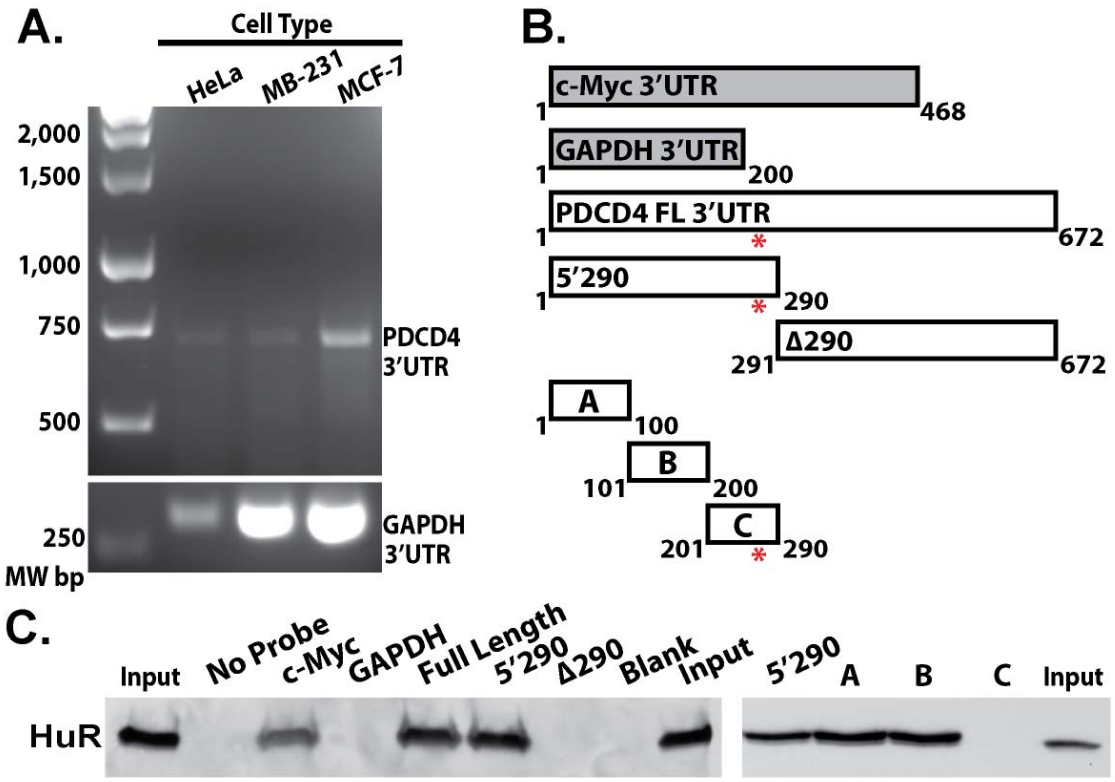

FIGURE 5.3: HuR binds to sites within the *PDCD4* 3′UTR. (A) Total RNA isolated from HeLa, MB-231 and MCF-7 cells was subjected to 3′RACE analysis using *PDCD4* and *GAPDH* 3′UTR-specific primers as described in Materials and Methods. PCR products were resolved on a 2% agarose gel and represent the 3′UTR plus the length of the primers used for amplification. The *PDCD4* 3′UTR is 672 nt and was verified by sequencing. The *GAPDH* 3′UTR is shown as a control. Molecular weight markers in base pairs (MW bp) are shown to the left of the gel. (B) Biotinylated probes corresponding to the 3′UTRs of the *c-Myc*, *GAPDH* and *PDCD4* transcripts were generated and used for biotin pulldown experiments in MCF-7 cells. The red asterisk denotes the well-defined *miR-21* seed region in the *PDCD4* 3'UTR. The *PDCD4* 3'UTR was also dissected to generate various biotin probes that represent different regions of the transcript. (C) Proteins that co-precipitated with the avidin-bound biotinylated probes, as shown in (B), were subjected to immunoblotting with HuR antibody. HuR protein co-precipitates with a probe corresponding to the *c-Myc* 3′UTR as well as the first two 100 nt regions of the *PDCD4* 3′UTR. Images are representative of n=3 independent experiments. (Wigington, Jung et al. 2014)

To validate the interaction of HuR with the *PDCD4* transcript, we also modulated both HuR levels and localization and assessed the impact on PLA signal. These experiments were carried out either in cells expressing endogenous HuR or where total levels of HuR were increased by expression of HuR-GFP. For both of these conditions, cells were also treated with the transcriptional inhibitor, Actinomycin D (ActD), which increases the cytoplasmic localization of HuR (Peng, Chen et al. 1998). To assess changes in the frequency of HuR-*PDCD4* mRNA interactions, we counted the number of HuR-*PDCD4* PLA punctae and normalized to the amount of mRNA in each cell, which was quantified by measuring the volume of probe signal for each cell. The probe volume was the same in both untransfected and HuR-GFP transfected cells with ($p=0.16$) and without ($p=0.26$) ActD (**Figure 5.4E**). This analysis confirms that the probe delivery and binding as well as the amount of RNA granules are not significantly affected by transfection. In contrast, as expected for treatment with a transcriptional inhibitor, incubation of cells with ActD reduced the total volume of PDCD4 mRNA by approximately 40% ($p<0.001$; quantified in **Figure 5.4E**).

Treatment with ActD resulted in significantly more HuR-*PDCD4* PLA punctae than untreated cells due to increased cytoplasmic HuR in both untransfected ($p<0.02$) and HuR-GFP transfected cells ($p<0.001$; quantified in **Figure 5.4F**). As experiments employed a low amount of HuR-GFP plasmid (0.8 μg) for transfection, HuR-GFP transfected cells untreated with ActD showed only a slight increase in PLA frequency compared to the untransfected samples ($p=0.046$). Without ActD, HuR was predominately in the nucleus, unavailable to interact with cytoplasmic *PDCD4* mRNA. Addition of ActD caused HuR to localize to the cytoplasm and resulted in a greater

increase in HuR-*PDCD4* interactions in the HuR-GFP transfected cells than in untransfected cells ($p<0.001$). These results demonstrate individual HuR-*PDCD4* interactions in MCF-7 cells and further validate the interaction between HuR and *PDCD4*.

HuR alters PDCD4 protein levels without affecting transcript stability

These immunoprecipitation, immunoblotting, and PLA data clearly demonstrate binding of HuR to the 3′UTR of the *PDCD4* transcript and raise the important question of whether HuR modulates the expression of *PDCD4*. The canonical role for HuR in the post-transcriptional regulation of target mRNA transcripts is as a positive regulator of mRNA stability (Brennan and Steitz 2001), however, some studies also suggest HuR modulating mRNA translation (Mazan-Mamczarz, Galban et al. 2003; Lal, Kawai et al. 2005; Kawai, Lal et al. 2006). To determine whether transient modulation of HuR levels has an impact on PDCD4 steady-state protein or mRNA levels, we performed siRNA-mediated knockdown of HuR in MCF-7 cells. As shown in Figure 5A, immunoblotting revealed a robust knockdown of HuR with HuR siRNA but not with scramble control siRNA. Probing these same samples with PDCD4 antibody reveals a decrease in PDCD4 protein upon HuR knockdown, but no change in a control protein, tubulin. Performed by CP Wigington, quantification of PDCD4 steady-state protein levels upon HuR knockdown confirmed a significant decrease in PDCD4 protein levels (**Figure 5.5B**). In contrast, qRT-PCR analyses performed with RNA from these samples revealed no significant change in *PDCD4* steady-state mRNA levels upon HuR knockdown (**Figure 5.5C**). These results implicate HuR in modulating levels of PDCD4 protein rather than RNA.

As mentioned above, generally, HuR binding to target mRNAs increases transcript stability. In fact, many HuR target mRNAs are inherently labile and responsive to cellular stimuli (Dani, Blanchard et al. 1984; von Roretz, Macri et al. 2011). As shown in **Figure 5.5C**, knockdown of HuR in MCF-7 cells does not impact steady-state *PDCD4* mRNA levels; however, this result does not technically preclude the possibility that HuR could modulate stability of the *PDCD4* transcript with some concomitant change in rates of *PDCD4* transcription. To determine the half-life of the *PDCD4* transcript in MCF-7 cells, CP Wigington treated cells with the potent transcriptional inhibitor, ActD (Hurwitz, Furth et al. 1962), and collected cells at 0, 3, 6 and 9 hours after drug addition. She performed qRT-PCR analysis with *PDCD4* primers to determine the percent mRNA remaining over time following ActD treatment (**Figure 5.5D**). For controls, she also analyzed the *c-Myc* transcript, which has a short half-life (Dani, Blanchard et al. 1984) as well as the very stable *RPLP0* transcript (Tani, Mizutani et al. 2012). As shown in **Figure 5.5D**, the *PDCD4* transcript showed significant decay over the course of the experiment, with a calculated half-life of 5.5 hours, which is less than the average mRNA half-life of 9 hours (Schwanhausser, Busse et al. 2011). These results suggest that the *PDCD4* transcript is labile. As expected, the *c-Myc* transcript levels decreased dramatically after ActD treatment with a calculated half-life of 1.5 hours, which is comparable to previously determined *c-Myc* mRNA half-life values (Dani, Blanchard et al. 1984). The *RPLP0* transcript did not decay over the time course examined as expected for a highly stable transcript.

To determine whether HuR modulates the stability of the *PDCD4* transcript, CP Wigington transfected MCF-7 cells with scrambled and HuR specific siRNA followed by

treatment with ActD. Cells collected at 0, 2, 3, 4, 5 and 6 hours after ActD treatment were analyzed by qRT-PCR to detect *PDCD4* transcript. As shown in **Figure 5.5A** and **5.5F**, she achieved a robust knockdown of HuR; however, no significant difference in the half-life of *PDCD4* mRNA between siScramble and siHuR-treated cells (**Figure 5.5E**) was detected, revealing that HuR does not modulate *PDCD4* mRNA stability.

Although the rate of decay of the *PDCD4* transcript was not altered, steady-state PDCD4 protein decreased rapidly over the time course of the ActD experiment. As shown in **Figure 5.5F**, immunoblot analysis of siScramble and siHuR-treated ActD samples with PDCD4 antibody revealed a sharp decrease in PDCD4 steady-state protein levels upon ActD treatment. Notably, the samples depleted of HuR displayed a greater initial decrease in PDCD4 protein upon ActD treatment (quantified in **Figure 5.5G**), again suggesting that HuR may play a role in influencing the translation of *PDCD4*.

The U-rich element RNA binding protein, TIA1, binds to *PDCD4* mRNA in MCF-7 cells

Several studies describe HuR as a positive regulator of target mRNA translation (Mazan-Mamczarz, Galban et al. 2003; Lal, Kawai et al. 2005; Kawai, Lal et al. 2006). Consistently, our results suggest that HuR may positively regulate the translation of the *PDCD4* transcript. Often such regulation occurs when a balance or competition exists between positive and negative regulators of translation. Interestingly, a previous study has defined a cooperative relationship between HuR and TIA1 in regulating the translation of specific target RNAs (Kawai, Lal et al. 2006). As shown in **Figure 5.6A**, alignment of iCLIP-Seq tags from a recent transcriptome-wide TIA1 iCLIP study in

HeLa cells (Wang, Kayikci et al. 2010) reveals two predicted TIA1 binding sites that overlap with the HuR binding site in 3'UTR (**Figure 5.3C**). These observations suggest that HuR and TIA1 could bind to similar or overlapping regions in the *PDCD4* 3′UTR.

To assess whether TIA1 binds to *PDCD4* mRNA in MCF-7 cells, CP Wigington performed RNA-IP with endogenous TIA1 protein. As shown in **Figure 5.6B**, TIA1 protein was detected in the bound fraction when purified with TIA1 antibody but not with IgG control antibody. The input and bound fractions were then analyzed for *PDCD4* transcript using qRT-PCR. As shown in **Figure 5.6C**, the *PDCD4* transcript was robustly enriched with TIA1. As controls, she also examined known TIA1 targets, Cytochrome c (*CYCS*) (Kawai, Lal et al. 2006) and Prothymosin α (*PTMA*) (Lal, Kawai et al. 2005), as well as *GAPDH*, which is not bound by TIA1. As expected, the *GAPDH* transcript showed no enrichment with TIA1, however, the previously defined TIA1 targets, *CYCS* and *PTMA*, showed enrichment. These results suggest that *PDCD4* mRNA is a target of TIA1 in MCF-7 cells.

To further validate the interaction between TIA1 and *PDCD4* mRNA, we performed PLA between TIA1 and FLAG-tagged probes on *PDCD4* mRNA in MCF-7 cells with and without TIA1-GFP transfection (**Figure 5.6D**). As shown in **Figure 5.6E**, we observed no significant difference in the amount of mRNA probes under any of the experimental conditions employed ($p=0.855$), suggesting that probe delivery and binding was not affected by TIA1-GFP transfection. TIA1-*PDCD4* mRNA interactions were observed by PLA with endogenous TIA1 levels and, as expected, a significant increase in TIA1-*PDCD4* interactions was observed by PLA upon TIA1-GFP transfection ($p<0.001$),

which demonstrates specific interaction between TIA1 and *PDCD4* mRNA in these cells (**Figure 5.6F**).

HuR and TIA1 compete for binding to *PDCD4* mRNA

To assess whether HuR and TIA1 cooperate or compete for binding to the *PDCD4* transcript, we modulated levels of TIA1 or HuR in MCF-7 cells and analyzed HuR-*PDCD4* interactions using PLA (**Figure 5.7A-C**). No difference in the probe volume was observed between treatment groups ($p=0.12$), demonstrating that probe delivery and binding as well as the level of *PDCD4* mRNA were not affected by transfection. As expected, upon reduction of HuR, HuR-*PDCD4* interactions decreased significantly ($p<0.001$; quantified in **Figure 5.7C**). A similar decrease in HuR-*PDCD4* interactions was observed upon overexpression of TIA1 through transfection of TIA1-GFP ($p<0.001$). In contrast, knockdown of TIA1 resulted in increased HuR-*PDCD4* interactions comparable to HuR-GFP transfected cells ($p=0.76$). These results suggest that increasing TIA1 may prevent HuR from binding to the *PDCD4* 3′UTR, while decreasing TIA1 facilitates HuR-*PDCD4* interactions (**Figure 5.7A-C**), which suggests a competitive relationship between HuR and TIA1 for binding to the *PDCD4* 3′UTR.

To determine whether changing HuR levels affects TIA1-*PDCD4* interactions, we modulated HuR by siRNA or HuR-GFP transfection and assessed TIA1-*PDCD4* PLA values. Again, we found no difference in probe volume between different transfection groups ($p=0.21$), indicating that probe delivery and binding as well as the level of *PDCD4* mRNA were not affected by transfection. As expected, knockdown and overexpression of TIA1 resulted in decreased and increased, respectively, TIA1-*PDCD4*

PLA interactions (**Figure 5.7D** and **5.7F**). Consistent with our model where HuR and TIA1 compete for binding to *PDCD4*, upon reduction of HuR, we observed an increase in TIA1 binding to *PDCD4* mRNA ($p<0.001$; **Figure 5.7D** and **5.7F**). In contrast, overexpression of HuR did not have a significant effect on TIA1 binding to *PDCD4* ($p=0.21$), but the level of HuR overexpression was quite modest (**Figure 5.7D-F**). These results suggest that the *PDCD4* transcript is competitively bound and regulated by HuR and TIA1 and therefore is regulated in a different manner than a previously described target mRNA that is cooperatively regulated by HuR and TIA1 (Kawai, Lal et al. 2006).

Conclusion

In this study, we identified the PDCD4 mRNA transcript as a novel target of HuR. Our results show that HuR binds to the *PDCD4* transcript via at least two distinct binding sites within the 3′UTR that overlap with predicted TIA1 binding sites. We demonstrate binding of TIA1 to the *PDCD4* mRNA and also show that modulation of TIA1 levels regulates HuR-*PDCD4* interactions in MCF-7 cells, suggesting a competitive interaction between HuR and TIA1 on the *PDCD4* transcript. This work as well as recent studies implicating HuR and TIA1 as dynamic and coordinate regulators of target mRNA expression (Kawai, Lal et al. 2006; Pullmann, Kim et al. 2007) suggests a model for regulation of *PDCD4* by HuR and TIA1 (**Figure 5.8**) and yields mechanistic insight into the post-transcriptional regulation of U-rich-containing mRNAs, such as *PDCD4*.

Recent transcriptome-wide CLIP-Seq studies on HuR demonstrate a preference for U-rich sequences (Kishore, Jaskiewicz et al. 2011; Lebedeva, Jens et al. 2011; Mukherjee, Corcoran et al. 2011; Uren, Burns et al. 2011). A few of these studies

performed RNA secondary structure prediction analyses on their target motifs, revealing a putative secondary structural motif for HuR binding (Lebedeva, Jens et al. 2011; Uren, Burns et al. 2011). An over-representation of U-rich motifs predicted to be located within variably sized hairpin loops was detected in one study (Uren, Burns et al. 2011). Another study reported a U-rich preference for HuR binding within 3′UTRs; however, computational folding predictions suggested single-stranded U-rich motifs with no indication of hairpins (Lebedeva, Jens et al. 2011). Our results show that HuR binds to two independent regions within the first 200 nt of the *PDCD4* 3′UTR. The *PDCD4* 3′UTR is considerably AU- or U-rich (68% and 37%, respectively) and contains two striking U-rich stretches within the 5′290 nt region of the 3′UTR. Indeed, these two U-rich regions are found within the first 200 nt of the 3′UTR and are consistent with the mapped HuR binding sites (**Figure 5.3**). Preliminary secondary structure prediction analyses of the 672 nt 3′UTR of *PDCD4* predict two single-stranded U-rich motifs within the first 200 nt, suggesting that these are the motifs bound by HuR (Zuker 2003). The predicted binding sites of TIA1 on the *PDCD4* 3′UTR overlap with the HuR binding sites and, due to the U-rich preference of TIA1, may represent U-rich regions that are competitively bound by HuR and TIA1 (**Figure 5.8A,B**).

Previous studies demonstrate that competition between HuR and TIA1 for binding to 5′ splice sites regulates alternative splicing in numerous cell types (Zhu, Hasman et al. 2006; Izquierdo 2008; Zhu, Hinman et al. 2008). However, there is no precedent for competition between HuR and TIA1 that influences mRNA stability and/or translation. Employing RNA imaging probes and PLA, we detected and quantified individual interactions between native *PDCD4* mRNA and either endogenous HuR or TIA1 in

single cells *in situ*. These PLA studies (**Figure 5.7**) provide evidence that HuR and TIA1 compete for binding to the *PDCD4* 3′UTR. Overexpression of TIA1 reduced interactions between HuR and *PDCD4*, while knockdown of TIA1 increased HuR-*PDCD4* interactions (**Figure 5.7**). Similarly, knockdown of HuR increased TIA1 interactions with *PDCD4* (**Figure 5.7**). This competition between HuR and TIA1 could regulate the translation of *PDCD4*, as suggested by the significant reduction of PDCD4 protein, but not mRNA, observed upon HuR knockdown (**Figure 5.5** and **5.8B**).

Other transcripts may be subject to coordinated regulation by HuR and TIA1. For example, the *β-actin* mRNA is bound by HuR via a U-rich region in its 3′UTR (1300-1339 nt) and this binding is associated with increased stability and translation of the mRNA (Dormoy-Raclet, Menard et al. 2007). TIA1 may bind to the same region as well as another U-rich region more distal from the coding region (Carrascoso, Sanchez-Jimenez et al. 2014). Interestingly, knockdown of HuR in HeLa cells led to a decrease in both β-actin protein and mRNA. Depletion of TIA1 did not affect *β-actin* mRNA levels but did increase protein levels. Such competition for binding sites need not be limited to HuR and TIA1. HuR and CUG triplet repeat RNA binding protein 2 (CUGBP2) have been reported to compete for binding to the 3′UTR of *cyclooxygenase-2* (*COX2*) mRNA to regulate translation. However, the binding sites of these RNA binding proteins have not been defined (Sureban, Murmu et al. 2007). Taken together, these studies support a general model where HuR and other RNA binding proteins, such as TIA1, compete for binding to target transcripts to modulate gene expression.

While the data presented in this study suggest a model where HuR and TIA1 compete for binding to overlapping *cis*-acting sequences, other RNAs may be regulated

through a mechanism where these RNA binding proteins cooperate with one another. For example, post-transcriptional regulation of the *cytochrome c* gene, which is a key regulator of apoptosis (Kulikov, Shilov et al. 2012), occurs through HuR and TIA1 binding to non-overlapping binding sites in the AU-rich regions within the 3′UTR (Kawai, Lal et al. 2006). Consistent with our finding, this study observed that HuR binding promotes the translation the *cytochrome c* mRNA without affecting mRNA levels while TIA1 binding inhibits translation (Kawai, Lal et al. 2006). In contrast to the observed competition between HuR and TIA1 reported here, the study of the *cytochrome c* transcript reported that HuR and TIA1 bind cooperatively to the *cytochrome c* 3′UTR such that increasing TIA1 levels increased HuR binding; however, increasing HuR levels had no detectable effect on TIA1 binding (Kawai, Lal et al. 2006). The caveat of this study, as the authors noted, is that the analysis of *cytochrome c* employed recombinant, exogenous proteins. In direct binding assays that employed RNA electrophoretic mobility shift assays, the authors did not observe simultaneous binding of HuR and TIA1 (Kawai, Lal et al. 2006). These results indicate that coordinate regulation by RNA binding proteins needs to be individually defined for each transcript.

In addition to competing or cooperating for binding sites on mRNAs, HuR and TIA1 bind to one another's 3′UTR and have the potential to co-regulate one another. *TIA1* mRNA stability and translation are controlled by HuR binding to its 3′UTR. In contrast, modulation of TIA1 does not affect HuR expression (Kawai, Lal et al. 2006; Pullmann, Kim et al. 2007). Hence, HuR appears to be a strong regulator of TIA1, but the reverse may not be true, suggesting a possible negative feedback mechanism for general regulation of gene expression. Understanding the interplay between HuR and TIA1 is

critical to further understand the post-transcriptional regulation of all HuR/TIA1 target mRNAs, including *PDCD4*.

The PDCD4 protein is an inhibitor of the eIF4A helicase, which unwinds secondary structural elements located within the 5′UTR of mRNA transcripts to facilitate translation (Yang, Jansen et al. 2003). PDCD4 expression is upregulated after the initiation of programmed cell death (or apoptosis) (Shibahara, Asano et al. 1995) and a reduction in PDCD4 protein levels leads to neoplastic transformation (Yang, Jansen et al. 2001). Because of the critical role for PDCD4 as a global regulator of protein synthesis and as a tumor suppressor, *PDCD4* expression is regulated at multiple levels (Lankat-Buttgereit and Goke 2009). *PDCD4* is regulated at the transcriptional level by the transcription factor, v-Myb (Schlichter, Burk et al. 2001) as well as by epigenetic regulation through DNA methylation (Fan, Zhao et al. 2007). With regard to post-transcriptional regulation of *PDCD4*, the only study beyond the extensive analysis of *miR-21* (Asangani, Rasheed et al. 2008; Frankel, Christoffersen et al. 2008), examines the regulation of the *PDCD4* transcript by the splicing factor, SRSF3 (Kim, Park et al. 2014). SRSF3 binds to the 5′UTR of the *PDCD4* transcript and modulates splicing and translational efficiency (Kim, Park et al. 2014) (**Figure 5.8C**). Post-translational regulation of PDCD4 includes phosphorylation of PDCD4 at serine 67 by Akt or S6K1, which leads to significantly decreased PDCD4 protein levels via increased proteasomal degradation (Dorrello, Peschiaroli et al. 2006; Schmid, Jansen et al. 2008) and methylation of PDCD4 at an N-terminal arginine residue that accelerates tumor growth (Powers, Fay et al. 2011) and promotes tumor cell viability during nutrient deprivation (Fay, Clegg et al. 2014). Our observation that reduction of HuR levels results in reduced

PDCD4 protein levels (**Figure 5.5**), as well as the fact that modulation of TIA1 levels inversely correlates with interactions between HuR and *PDCD4* (**Figure 5.7**), suggests that HuR and TIA1 compete to modulate the *PDCD4* mRNA and therefore represents an additional point of regulation for *PDCD4* expression (**Figure 5.8**).

Analysis of RNA regulons and the cooperation and/or competition of multiple RNA binding proteins on target mRNAs suggest a complex and dynamic post-transcriptional regulatory program (Keene 2007). The observation that RBPs such as HuR interface with miRNA machinery (Srikantan, Tominaga et al. 2012) adds additional complexity to the regulation of target mRNAs. In fact, numerous studies demonstrate a competitive relationship between HuR and miRNA machinery at both the individual transcript (Bhattacharyya, Habermacher et al. 2006; Epis, Barker et al. 2011; Srikantan, Abdelmohsen et al. 2011; Tominaga, Srikantan et al. 2011; Young, Moore et al. 2012) and transcriptome-wide (Lebedeva, Jens et al. 2011; Mukherjee, Corcoran et al. 2011) levels. The transcriptome-wide PAR-CLIP analyses that examined interplay between HuR and miRNAs suggest that transcripts with non-overlapping HuR/miRNA binding sites (such as *PDCD4*) are likely regulated by the miRNA instead of HuR (Lebedeva, Jens et al. 2011; Mukherjee, Corcoran et al. 2011). Our results demonstrate that modulation of HuR impacts the steady-state protein, but not mRNA, level of *PDCD4* and suggest a model where HuR regulates the translation of *PDCD4*. The mechanism by which HuR modulates translation is not well understood; however, recent studies demonstrate that direct competition between HuR and miRNAs can influence translation (Bhattacharyya, Habermacher et al. 2006). Alternatively, HuR binding could influence the secondary structure of the 3′UTR to modulate miRNA binding/accessibility

(Srikantan, Tominaga et al. 2012). This type of coordination is challenging to study and is therefore less understood than direct competition.

As mentioned previously, the *PDCD4* 3'UTR is a well-studied target of the oncomiR, *miR-21* (Asangani, Rasheed et al. 2008; Frankel, Christoffersen et al. 2008), which is overexpressed in many cancer types (Pan, Wang et al. 2010) and targets the *PDCD4* transcript via a well-studied seed region within the 3′UTR (Asangani, Rasheed et al. 2008). The *miR-21* seed region lies within the 290 nt region of the *PDCD4* 3′UTR that was identified in a HuR iCLIP study (Uren, Burns et al. 2011). However, the *miR-21* seed region does not overlap with the HuR binding sites identified here (**Figure 5.3**) and is instead located more distal to the coding region (miRNA seed region designated by red asterisk in **Figure 5.3B**). If *miR-21* is involved in HuR-mediated regulation of *PDCD4* translation, the location of the *miR-21* binding site is more consistent with a model where HuR impacts the local RNA structure to modulate miRNA binding than direct competition.

In addition to possible modulation of *miR-21* binding, growing evidence shows that HuR binds to and regulates the processing of primary miRNA (pri-miR) transcripts (Lebedeva, Jens et al. 2011; Mukherjee, Corcoran et al. 2011; Young, Moore et al. 2012). A recent study demonstrated HuR binding to and destabilizing *miR-7* (Lebedeva, Jens et al. 2011), suggesting that this may represent another mode of regulation by HuR in post-transcriptional processing. Interestingly, another study identified HuR binding to the *pri-miR-21* transcript (Mukherjee, Corcoran et al. 2011), which could indicate direct regulation of the *miR-21* transcript by HuR. These results suggest that knocking down HuR could result in elevated *miR-21* levels, leading to reduced PDCD4 protein levels, as

reported in this study. Like HuR, TIA1 also may play a role in modulating gene expression via interactions with miRNA machinery.

Further study is required to understand how direct interactions and feedback mechanisms between *miR-21*, as well as other miRNAs predicted to bind the *PDCD4* 3′UTR, and RBPs, such as HuR and TIA1, function coordinately to control post-transcriptional regulation of biologically important transcripts such as *PDCD4*.

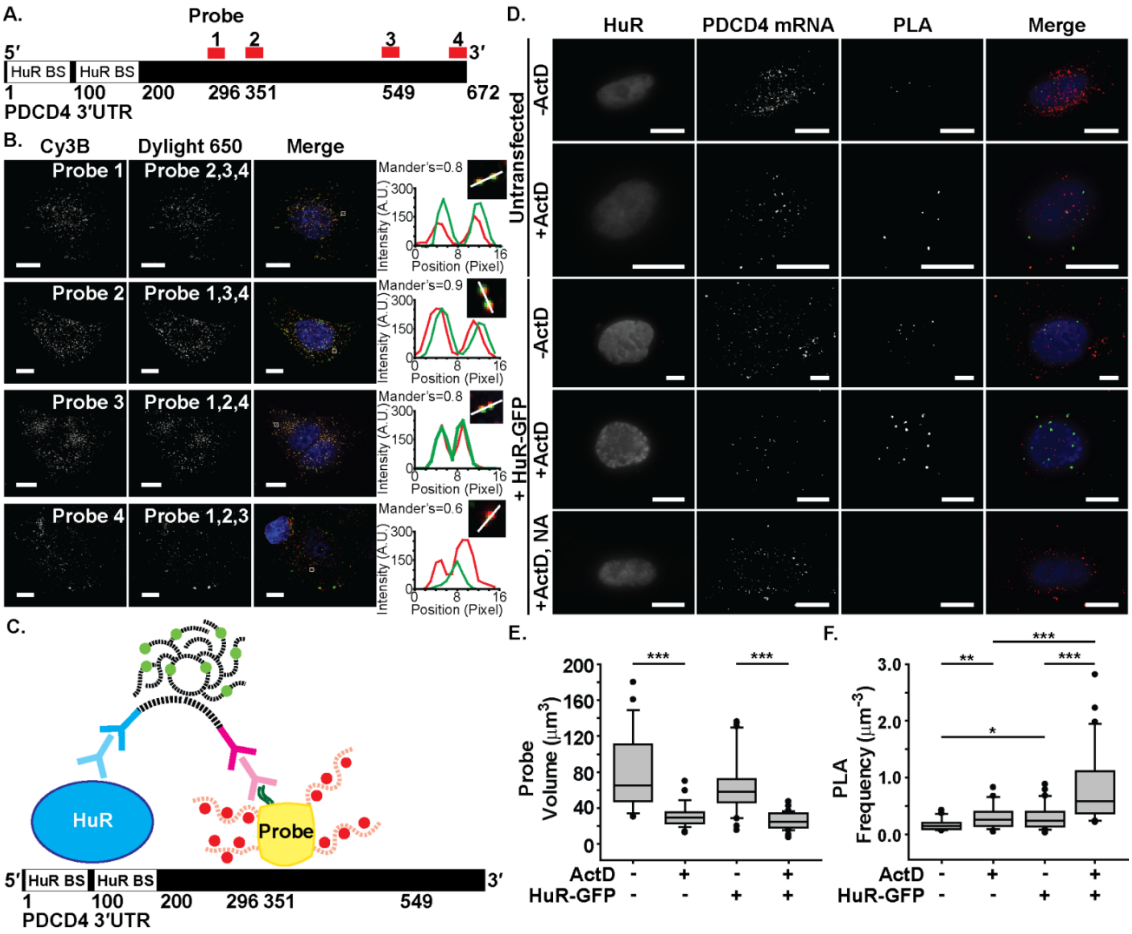

FIGURE 5.4: Visualization of HuR-*PDCD4* interactions *in situ* using FLAG-tagged probes. (A) The 672 nt *PDCD4* 3′UTR contains two HuR binding sites (HuR BS) within the first 200 nt. Four mRNA probes (1, 2, 3 and 4) were designed to target distinct positions within the *PDCD4* 3′UTR (shown in red). (B) Each of four PDCD4 3′UTR probes labeled with Cy3B fluorophores was delivered to MCF-7 cells along with the other three probes labeled with Dylight 650 fluorophores. Merge images of Cy3B-labeled probe (red), Dylight 650-labeled probe (green), and DAPI-stained nuclei (blue) are also shown. All image planes are represented. Magnified, merge images of overlapping probes in the boxed region are shown with profile plot of the fluorescence intensity of Cy3B (red) and Dylight 650 (green) along an intersection of the probes (white line). Scale bar, 10 μm. The mean Mander's coefficient of Cy3B and Dylight 650 probe colocalization is shown. (C) A schematic of the proximity ligation assay (PLA), which measures the interaction between HuR and probes specific to the *PDCD4* 3'UTR is shown. As described in Experimental Procedures, PLA was performed between HuR and FLAG-tagged (dark green lines) probes with four Cy3b-labeled (red) oligonucleotides (red dash lines) and a neutravidin core (yellow) in nucleotides 296-549 of the *PDCD4* 3′UTR. Anti-HuR mouse primary antibody (light blue) and anti-mouse PLA probe (dark blue) bind to HuR, while anti-FLAG rabbit primary antibody (light magenta) and anti-rabbit

PLA probe (dark magenta) bind to FLAG. Once they are in proximity, the oligonucleotides (black dash lines) attached to the PLA probe come together via ligation to form a template for DNA polymerase, which resulted in a coiled DNA product that can be labeled with Cy5-equivalent fluorophore (light green) bound complementary DNA strands (black dash lines). (D) HuR, *PDCD4* mRNA and PLA between HuR and *PDCD4* mRNA were imaged in untransfected and HuR-GFP transfected MCF-7 cells exposed to (+ActD) or unexposed to (-ActD) actinomycin D. MCF-7 cells transfected with HuR-GFP and exposed to ActD received *PDCD4* mRNA probes with neutravidin lacking the FLAG tag (NA) and were used as a negative control. Merge images of HuR (blue), *PDCD4* mRNA (red) and PLA between HuR and *PDCD4* mRNA (green) are shown. All image planes are represented. Scale bar, 10 μm. (E) Probe volume (μm^3) measured for each untransfected and HuR-GFP transfected cell exposed or unexposed to ActD (Untransfected: n=46 cells; Untransfected, +ActD: n=125; HuR-GFP transfected: n=51; HuR-GFP transfected, +ActD: n=62). (F) PLA frequency normalized to the probe volume (μm^{-3}) for each cell. * represents $p \geq 0.025$, $p < 0.05$; ** represents $p \geq 0.001$, $p < 0.025$; *** represents $p < 0.001$ (one-way ANOVA with Dunn's method). (Wigington, Jung et al. 2014)

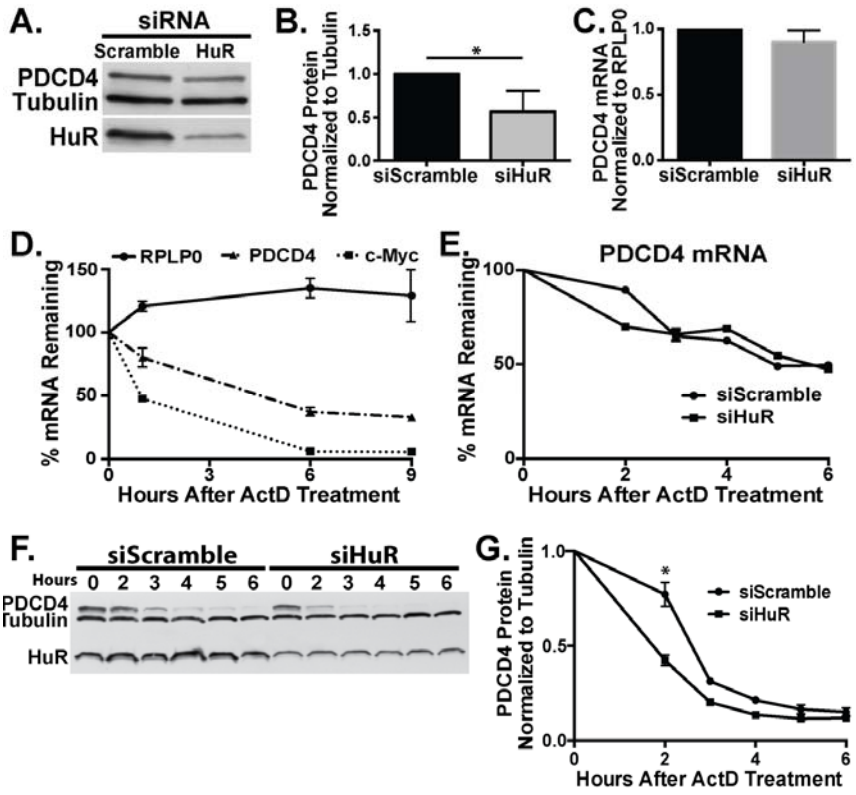

FIGURE 5.5: HuR modulates PDCD4 protein levels. (A) MCF-7 cells transiently transfected with Scramble or HuR siRNA were subjected to immunoblot analysis with PDCD4, Tubulin, or HuR antibody. (B) Results of (A) were quantified as described in Experimental Procedures. The level of PDCD4 protein is normalized to tubulin loading control and siScramble set to 1.0. (C) qRT-PCR analysis of total RNA isolated from siRNA-treated cells demonstrates no significant difference in *PDCD4* steady-state mRNA levels upon HuR knockdown. (D) MCF-7 cells were treated with ActD and collected at the indicated time points after drug addition. Total RNA isolated from ActD-treated cells was subjected to qRT-PCR analysis with *RPLP0*, *PDCD4* and *c-Myc* primers. mRNA levels were normalized to time zero and are represented as % of amount present at time 0. The half-life of the *c-Myc* and *PDCD4* transcripts was calculated to be 1.5 and 5.5 hours, respectively. (E) MCF-7 cells transfected with Scramble or HuR siRNA were treated with ActD and collected at the indicated time points after drug addition. Results are analyzed and presented as in (D). No significant difference in *PDCD4* mRNA half-life was observed between scramble and HuR knockdown samples. (F) Immunoblot analysis of total protein isolated from the samples in (E) to detect PDCD4, Tubulin and HuR reveal a sharp decrease in PDCD4 protein upon treatment with ActD. (G) Quantification of data from panel F reveals a significant difference in PDCD4 protein levels shortly after ActD treatment. Data points represent the mean ± SEM for n=3 independent experiments. * represents $p<0.05$. Images are representative of n=3 independent experiments. (Wigington, Jung et al. 2014)

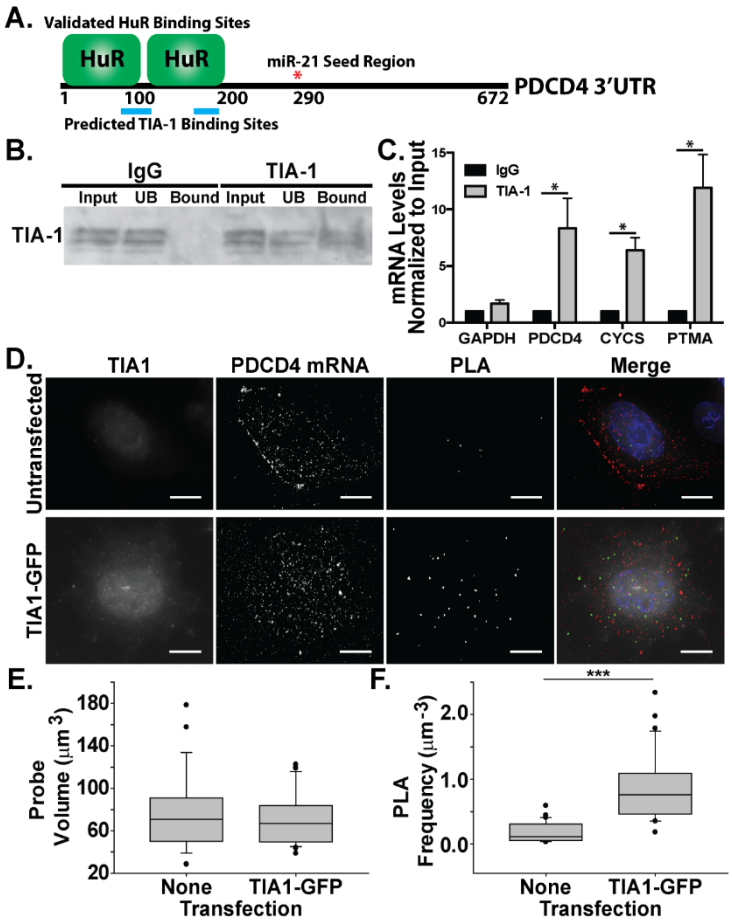

FIGURE 5.6: The RNA binding protein, TIA1, interacts with *PDCD4* mRNA. (A) A recent TIA1 iCLIP study reveals two predicted TIA1 binding sites (shown here in blue) within the first 200 nt of the *PDCD4* 3′UTR that overlap with the validated HuR binding sites (green) defined here. The red asterisk denotes the well-defined *miR-21* seed region. (B) Endogenous TIA1 protein was immunoprecipitated from MCF-7 cells using TIA1 antibody-coated protein A beads alongside isotype control Goat IgG-coated beads. Proteins from the Input, unbound (UB) and Bound fractions were subjected to immunoblotting with TIA1 antibody. TIA1 was detected in the HuR-bound fraction but not the control IgG bound fraction. TIA1 is alternatively spliced to generate two distinct protein products that correspond to the two bands detected. (C) qRT-PCR analysis of RNA isolated from the TIA1 RNA-IP using *PDCD4*, *CYCS* and *PTMA* primers reveals clear enrichment of these transcripts upon TIA1 pulldown. A control mRNA, *GAPDH*, did not co-precipitate with TIA1. Values represent the mean ± SEM for n=3 independent experiments. * represents $p<0.05$. (D) PLAs performed with TIA1 antibody and *PDCD4* 3′UTR probes 1-3 reveal interactions between TIA1 and the *PDCD4* 3′UTR. (E) Probe volume (μm^3) measured for each untransfected (n=11 cells) and TIA1-GFP transfected (n=15) cell. (F) The PLA frequency normalized to the probe volume (μm^{-3}) for each cell. *** represents $p<0.001$ (Mann-Whitney rank sum test). (Wigington, Jung et al. 2014)

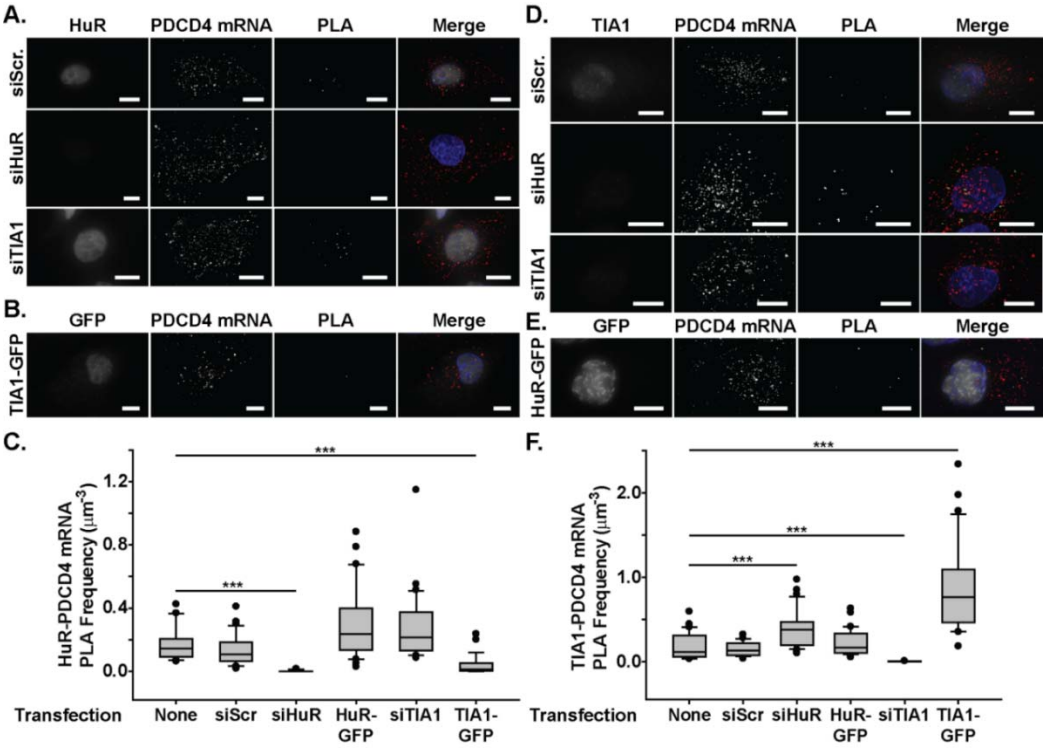

FIGURE 5.7: HuR and TIA1 compete for binding to the *PDCD4* 3′ UTR. A) Visualization of HuR protein, *PDCD4* mRNA and interaction between HuR and *PDCD4* mRNA (PLA) in control cells transfected with scrambled siRNA (siScr), or siRNA directed against either HuR (siHuR) or TIA1 (siTIA1). Merged images of HuR (white), *PDCD4* mRNA (red), PLA (green) and nuclei (blue) are also shown. All image planes are represented. Scale bar, 10 μm. B) Visualization of GFP, *PDCD4* mRNA and interaction between HuR and *PDCD4* mRNA in TIA1-GFP transfected cells. Merged images of GFP (white), *PDCD4* mRNA (red), PLA (green) and nuclei (blue) are also shown. All image planes are represented. Scale bar, 10 μm. C) HuR-*PDCD4* mRNA PLA frequency normalized to probe volume (μm^{-3}) for untransfected (n=46 cells), siScramble (n=81), siHuR (n=25), HuR-GFP (n=51), siTIA1 (n=97), and TIA1-GFP (n=69) cells. *** represents $p<0.001$ (one-way ANOVA with Dunn's method). D) Visualization of TIA1 protein, *PDCD4* mRNA and PLA interaction between TIA1 and *PDCD4* mRNA in siScramble (siScr), siHuR and siTIA1 transfected cells. Merged images of TIA1 (white), *PDCD4* mRNA (red), PLA (green) and nuclei (blue) are also shown. All image planes are represented. Scale bar, 10 μm. E) Visualization of GFP, *PDCD4* mRNA and PLA interaction between TIA1 and *PDCD4* mRNA in HuR-GFP transfected cells. Merged images of HuR (white), *PDCD4* mRNA (red), PLA (green) and nuclei (blue) are shown. All image planes are represented. Scale bar, 10 μm. F) TIA1-*PDCD4* mRNA PLA frequency normalized to probe volume (μm^{-3}) for untransfected (n=55 cells), siScramble (n=49), siHuR (n=66), HuR-GFP (n=46), siTIA1 (n=44), and TIA1-GFP (n=76) cells. ***represents $p<0.001$ (one-way ANOVA with Dunn's method). (Wigington, Jung et al. 2014)

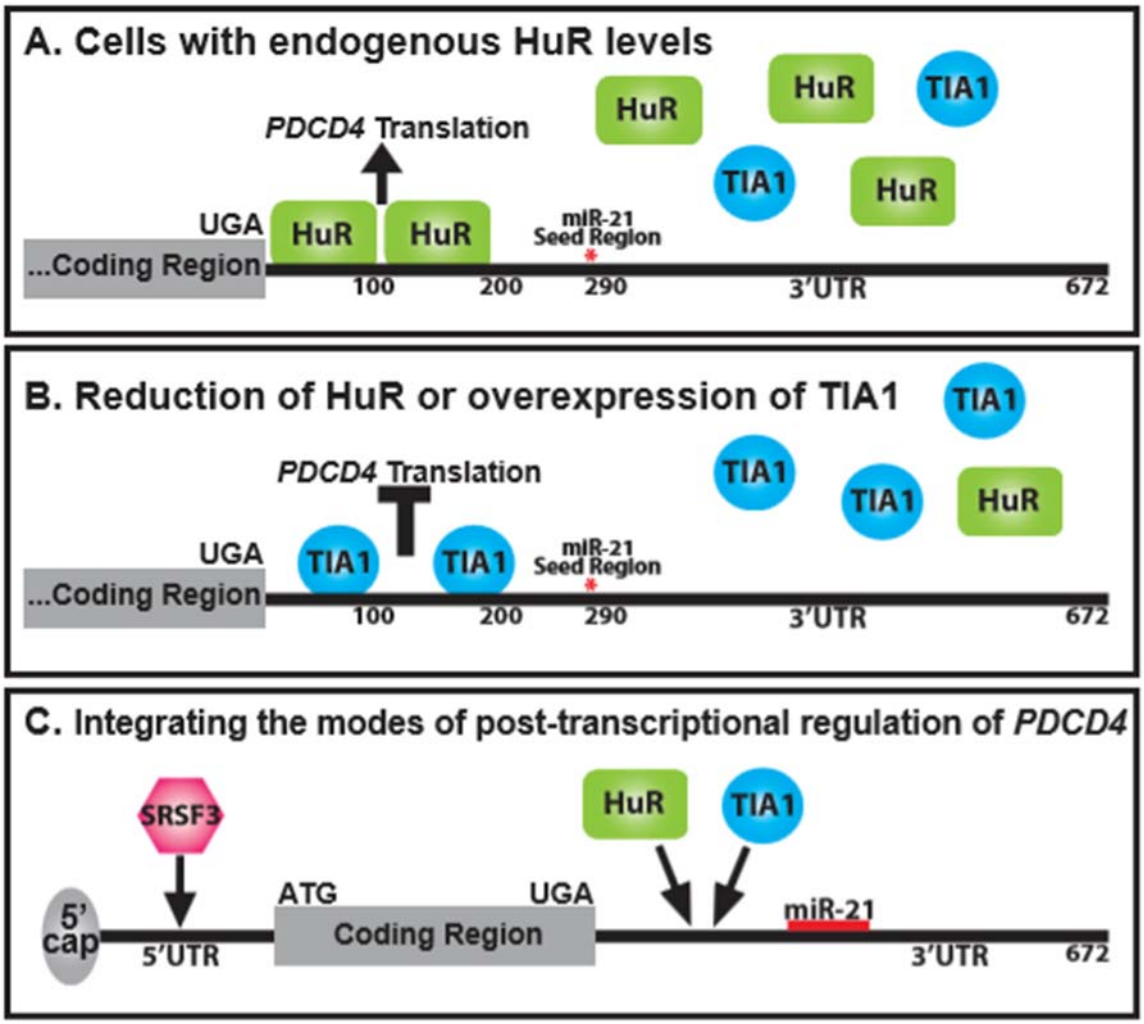

FIGURE 5.8: Model for post-transcriptional regulation of the *PDCD4* transcript. (A) HuR binds two independent regions proximal to the stop codon (UGA) in the *PDCD4* 3'UTR. Our data suggest that HuR (green rectangles) binding to the *PDCD4* transcript maintains the level of PDCD4 protein present in these cells (**Figure 5.5**) and therefore may positively regulate the translation of *PDCD4*, possibly through competition with TIA1 (blue circle). The *PDCD4* 3'UTR is a well-studied target of *miR-21* (red asterisk), and therefore may represent a site of dynamic interplay between miRNA machinery and HuR. (B) Either Reduction of HuR or overexpression of TIA1, causes an increase in TIA1-*PDCD4* interactions, suggesting that HuR and TIA1 compete for binding to an overlapping binding site within the *PDCD4* 3'UTR. (C) The *PDCD4* transcript is post-transcriptional regulated by a number of different factors, including the splicing factor, Serine/Arginine-rich Splicing Factor 3 (SRSF3; pink hexagon) and *miR-21* (red line). This study uncovers an additional point of regulation on the *PDCD4* transcript that impacts the cellular pool of PDCD4 protein. (Wigington, Jung et al. 2014)

Materials and methods

MCF-7 cells (ATCC HTB-22; Estrogen Receptor positive [ER+] breast cancer cell line) were obtained from ATCC and maintained in Dulbecco's modified Eagle's medium (DMEM) supplemented with 10% FBS and antibiotics. DNA plasmids and siRNA (Invitrogen) were transfected into cultured cells using Lipofectamine2000 (Invitrogen) or Neon Electroporation System (Invitrogen) according to manufacturer's protocol. Cells were plated on No 1.5 glass coverslips (Ted Pella) one day prior to transfection for imaging.

A FLAG fusion construct for HuR was generated using PCR primers that include the FLAG sequence, creating an N-terminally FLAG tagged protein. The PCR product was then subcloned into the pcDNA3.1 vector (Invitrogen). The HuR RNA binding mutant (HuR(BM); N21A, Y109A, R147A) was generated by site-directed mutagenesis using the Quikchange Kit (Stratagene). Primers used throughout the study are shown in Table 1. MCF-7 cells were transfected with 0.8 μg HuR-GFP or 0.8 μg TIA1-GFP plasmid (gifts from Dr. Myriam Gorospe, NIH/NIA). mRNA-targeted probes were delivered 36 h after plasmid transfection. A set of three pre-designed Stealth siRNAs (Assay ID numbers s4608, s4609, and s4610; Invitrogen) or 200 nM On-TARGET SMARTPool HuR siRNA (Thermo Scientific Dharmacon) were employed for knockdown of HuR. For control, 200 nM On-TARGETplus Non-targeting siRNA #1 (Thermo Scientific Dharmacon) was used. mRNA-targeted probes were delivered 48 h after siRNA transfection.

MCF-7 cells were harvested and washed in 1X PBS and then lysed on ice in RIPA-2 buffer (150 mM NaCl, 1% NP40, 0.5% deoxycholate, 0.1% SDS, 50 mM Tris pH 8.0) containing protease inhibitors (PLAC: 3 μg/ml of pepstatin, leupeptin, aprotinin, and chymostatin and 0.5 mM PMSF). Immunoblotting was performed using standard methods. Briefly, 30 μg of total protein lysate per sample was resolved by SDS-PAGE and transferred onto a nitrocellulose membrane. For immunoblotting, a 1:1,000 dilution of HuR or TIA1 antibody (Santa Cruz; Clones 3A2 and c-20, respectively), a 1:4,000 dilution of PDCD4 antibody (Rockland; Rabbit polyclonal), or a 1:5,000 dilution of α-tubulin antibody (Sigma; Clone DM1A) was used followed by 1:3,000 dilutions of HRP-conjugated goat anti-mouse IgG, HRP-conjugated goat anti-rabbit IgG, or HRP-conjugated mouse anti-goat IgG secondary antibodies (Jackson ImmunoResearch).

Total RNA was isolated from MCF-7 cells using TRIzol reagent (Invitrogen) in accordance with the manufacturer's instructions. Reverse transcriptase reactions with M-MLV RT (Invitrogen) used 1 μg of RNA for a final concentration of 50 ng/μL cDNA per sample that was used for quantitative RT-PCR.

For qRT-PCR analyses, 1 μg of total RNA was transcribed to cDNA as described above. Relative mRNA levels were measured by quantitative PCR analysis of triplicate samples of 5 ng cDNA with QuantiTect SYBR Green Master Mix using an Applied Biosystems real time machine (ABI). Results were analyzed using the ΔΔCT method and normalized to the *18s rRNA* or *RPLP0* transcript. Statistical significance was determined using One-Way ANOVA.

RNA-IPs to assay endogenous HuR/*PDCD4* mRNA interactions were performed using standard methods (Jain, Devine et al. 2011). Briefly, MCF-7 cells were grown to confluency in 100-mm dishes and rinsed twice with ice cold PBS. Lysates were prepared with an equal pellet volume of polysome lysis buffer (PLB; 10 mM HEPES pH 7.0, 100 mM KCl, 5 mM MgCl2, 0.5% NP-40, 1 mM DTT, RNase OUT [Invitrogen], and 1 cOmplete protease inhibitor tablet [Roche]) and stored at -80°C. Protein A sepharose beads (Santa Cruz) were incubated at 4°C overnight with either mouse IgG or HuR antibody (Santa Cruz). Beads coated in antibody were resuspended in NT2 buffer (50 mM Tris-HCl, pH 7.4, 150 mM NaCl, 1 mM $MgCl_2$, 0.05% NP-40) supplemented with RNase OUT (Invitrogen) and 1 mM DTT. Thawed and clarified cell lysates were added and the bead-antibody-cell lysate mixture was incubated at 4°C for 2 hours while tumbling end over end. After incubation, beads were spun down and washed 5 times with cold NT2 buffer. The bound RNA was isolated with TRIzol (Invitrogen) and purified according to manufacturer's instructions.

To detect FLAG-HuR/*PDCD4* mRNA interactions, MCF-7 cells were grown to near confluency in 100-mm plates and transfected with pcDNA3, FLAG-HuR, or -HuR(BM) plasmids. After 48 hours, cell lysates were prepared and frozen as described above. FLAG-M2 magnetic beads (Sigma) were resuspended in supplemented NT2 buffer described above. Thawed and clarified cell lysates were added to beads and incubated at 4°C for 2 hours while tumbling end over end. After incubation, beads were magnetized and washed 5 times with cold NT2 buffer. FLAG-HuR/RNA complexes were eluted with excess FLAG peptide (Sigma) and bound RNA was isolated with TRIzol (Invitrogen) and purified according to manufacturer's instructions.

Prior to visualization by indirect immunofluorescence, MCF-7 cells were fixed with 1-2% formaldehyde (EM Science) for 10 min, permeabilized with 0.1%Triton X-100 for 5 min, and incubated with Hoechst or DAPI (Invitrogen) to mark the position of the nucleus. To localize endogenous HuR, FLAG-HuR, or HuR-GFP by immunofluorescence, cells were probed with mouse monoclonal anti-HuR (1:1,000; 3A2, Santa Cruz), mouse monoclonal anti-FLAG (1:1,000; M2, Sigma), or goat polyclonal anti-GFP (1:500; ab5450, Abcam) antibody followed by staining with Texas Red or Fluorescein-conjugated secondary antibodies (Jackson ImmunoResearch). For immunostaining endogenous TIA1 or TIA1-GFP, cells were probed with polyclonal rabbit anti-TIA1 (1:500; AV40981, Sigma) or anti-GFP (1:500; ab5450, Abcam) antibody followed by staining with Cy3 or Fluorescein-conjugated secondary antibody (Jackson ImmunoResearch). Images were obtained using an Olympus IX81 microscope with a 0.3 numerical aperture (NA) 100× Zeiss Plan-Neofluor objective or an Axiovert 200 M microscope (Zeiss) with a 1.4 NA 63× Plan-Apochromat objective unless otherwise stated. Images were captured using a Hamamatsu digital camera with Slidebook software (version 1.63) or Volocity acquisition software (PerkinElmer) and globally processed for brightness and contrast using Adobe Photoshop.

To determine the precise length of the *PDCD4* 3′UTR in human cell lines, we isolated RNA from HeLa (ATCC CCL-2), MDA-MB-231 (ATCC HTB-26) and MCF-7 (ATCC HTB-22) cells using TRIzol reagent (Invitrogen) in accordance with the manufacturer's instructions. Reverse transcriptase reactions were carried out as follows: 1 μg of RNA was combined with 1 μL of dNTPs (10 mM), 1 μL of the 3′RACE adaptor (See Table 1; 10 mM) and DEPC-treated water for a total volume of 13 μL. Samples

were incubated at 65ºC for 5 minutes and then transferred to ice. To the RNA mixture-3′RACE adaptor mixture, 4 μL 5X First-Strand buffer (Invitrogen), 1 μL 0.1 M DTT and 1 μL RNaseOUT (40 U/μL; Invitrogen) were added. Samples were incubated at 42ºC for 2 minutes before adding 1 uL SuperScript III RT (200 U/μL; Invitrogen), briefly vortexing, and returning to 42ºC for 50 minutes. Following first strand synthesis, samples were heated to 70ºC for 15 minutes to denature the RT enzyme. For each PCR reaction, 40 ng of cDNA was used along with the outer 3′RACE primer and a gene-specific inner primer (see Table 1) with the AmpliTaq Gold 360 Master Mix (Invitrogen), according to manufacturer's instructions. PCR products were resolved on a 2% agarose gel and confirmed by TOPO cloning (Invitrogen) and sequencing.

To assess direct binding of HuR to the *PDCD4* transcript, DNA sequences corresponding to the 3′UTRs of *c-Myc* and *GAPDH* as well as various regions of the *PDCD4* 3′UTR (full length, 5′290, Δ290, 1-100, 101-200, and 201-290) were amplified by PCR and inserted into pGEM T-easy vectors (Promega) and linearized by digestion with *SpeI* (New England Biolabs). Biotinylated RNA probes were generated by *in vitro* transcription using the T7 Maxiscript kit (Ambion) with Biotin-11-cytidine-5′-triphosphate (biotin-11-CTP; Roche). Biotinylated CTP and normal CTP were used at a ratio of 1:4 to ensure adequate transcription yield and sufficient labeling. Nonincorporated nucleotides were removed with a G-25 column (GE Healthcare Bio-Sciences) followed by ethanol precipitation. RNA concentration was determined by A260 absorption and the quality was examined by denatured RNA electrophoresis. MCF-7 cells were lysed in IP buffer (50 mM Tris-HCl, pH 7.5, 150 mM NaCl, 5 mM $MgCl_2$, 0.5 mM DTT, 1% NP-40 supplemented with cOmplete protease inhibitor tablets [Roche] and

RNase OUT [Invitrogen]), spun at 13,000 RPM for 20 minutes at 4°C, and ~200 µg of purified cell lysate were rotated end-over-end with 400 ng of biotinylated RNA probe for 20 minutes at room temperature. To precipitate biotinylated RNA probes from MCF-7 cell lysates, NeutrAvidin beads (Thermo Scientific) pre-blocked with BSA (Roche) were added and rotated end-over-end for 30 minutes at 4°C. After precipitation, the beads were washed 5 times in IP buffer and then subjected to elution by boiling in reducing sample buffer (RSB). Bound proteins were analyzed by immunoblotting to detect HuR.

To measure mRNA stability in MCF-7 cells, 5 µg/ml actinomycin D (Sigma) was added to the growth medium to inhibit transcription and cells were harvested 0, 1, 6, and 9 hours later. To measure mRNA stability in MCF-7 cells with reduced HuR levels, cells were transfected with HuR siRNA 24 hours after seeding. Following a 48-hour incubation with siRNA, 5 µg/ml actinomycin D was added to the growth medium and cells were harvested 0, 2, 3, 4, 5, and 6 hours later. Total RNA was extracted from cells (described above) and analyzed by qRT-PCR. Half-lives were determined by normalization to *18s* rRNA and to time 0.

Probes were synthesized as previously described (Santangelo, Lifland et al. 2009; Jung, Lifland et al. 2013). Briefly, FLAG-hyNic (Solulink) was added to 4FB-modified (Solulink) neutravidin (Thermo Scientific Pierce) according to the manufacturer's protocol. For each probe, 2′-O-methyl RNA-DNA oligonucleotide chimeras complementary to the target sequence were designed with a 5′-biotin and dT-C6-NH2 internal modifications (Biosearch Technologies). Cy3B NHS ester fluorophores (GE Healthcare) or Dylight 650 NHS Ester fluorophores (Thermo Scientific Pierce) were conjugated to the oligonucleotide amino groups using the manufacturer's protocol. Free

dye was removed using 30 kDa Amicon spin columns (EMD Millipore). The purified, labeled oligonucleotides were tetramerized by incubation for 1 hour at room temperature with untagged or FLAG-tagged neutravidin. Free ligands were removed using 30 kDa Amicon spin columns (EMD Millipore). Three probes each targeting different sequences in the 3′ UTR of *PDCD4* mRNA (Table 2) were assembled separately prior to delivery and combined during delivery. To deliver total 60nM probes targeting *PDCD4* mRNA, 20 nM of each probe was combined.

For probe delivery, cells were washed in Dulbecco's phosphate buffered saline (DPBS) without Ca^{2+} and Mg^{2+} (Lonza) and subsequently, incubated with 0.15 U/mL activated streptolysin O (Sigma) in OptiMEM (Invitrogen) containing 60 nM *PDCD4* mRNA probes for 10 min at 37°C. Delivery media were replaced with growth media for 15 min to restore membrane integrity before actinomycin D treatment or fixation. For actinomycin D treatment, cells were incubated for 90 min at 37°C with 5 μg/mL actinomycin D (Sigma) in growth media and fixed at the end of the exposure.

The Proximity Ligation Assay (PLA) was performed as previously described (Jung, Lifland et al. 2013). Cells were fixed with 1% paraformaldehyde (Electron Microscopy Science) in PBS for 10 min, permeabilized with 0.2% Triton X-100 (Sigma) for 5 min, and blocked for 1 h with a blocking solution. The blocking solution consisted of 0.5% Tween-20 (CalBioChem), 0.1% Triton X-100, 0.1% gelatin (Aurion), 2% donkey serum (Sigma), and 1% bovine serum albumin (BSA) (EMD) in PBS. Cells were washed with PBS, incubated in two primary antibodies, one against the FLAG-tagged neutravidin and one against the protein of interest. For anti-FLAG antibodies, either rabbit polyclonal (1:2000; F7425, Sigma) or mouse monoclonal (1:2000; M2, Sigma)

anti-FLAG antibody was used. Mouse monoclonal anti-HuR (1:750; 3A2, Santa Cruz) was used to detect HuR, and rabbit polyclonal anti-TIA1 (1:1500; AV40981, Sigma) was used to detect TIA1. After washing with Duolink wash solution (Olink Bioscience), the cells were incubated with species-corresponding oligonucleotide-labeled PLA probes (Olink Bioscience) diluted in 0.05% Tween-20 in PBS and washed with Duolink wash solution. The ligation and rolling circle amplification reaction (Olink Bioscience) were performed as instructed in the manufacturer's protocol. The cells were then immunostained and DAPI-stained (Invitrogen) and mounted on slides using Prolong (Invitrogen).

All the images were collected using an Axiovert 200 M microscope (Zeiss) with a 63×, NA 1.4 Plan-Apochromat objective and an ORCA-ER AG camera (Hamamatsu). The images were acquired using the Volocity acquisition software (PerkinElmer). Image stacks were recorded at 200 nm intervals to sample volumes for iterative deconvolution using Volocity's deconvolution algorithms. Probe and PLA signal quantification and Mander's coefficients were computed in Volocity and imported into Excel (Microsoft) and Sigma Plot (Systat) for further analysis and plotting. Images presented have been linearly contrast enhanced for clarity. All calculations were performed directly on raw, deconvolved widefield data.

The RNA volume and PLA frequency normalized to the RNA volume were measured using Volocity (PerkinElmer). Each cell was identified by the probe signal or immunofluorescence and analyzed individually. The Mander's coefficient calculation for probe colocalization was performed using Volocity. We analyzed three representative images. In Sigma Plot, all pairwise multiple comparison procedure was performed with

Tukey method to compare the Mander's coefficients for each probe. The RNA volume was determined based on standard deviation intensity of the probe. The PLA signal initially was identified as objects by their standard deviation intensity then separated into individual punctae using the 'separate touching objects' tool. The punctae were further filtered based on size and maximum intensity. For each experiment, we analyzed at least ten images of each coverslip and three repeated experiments. In Sigma Plot, when comparing more than two groups, all pairwise multiple comparison procedure was performed with Dunn's method to compare the RNA volume and PLA frequency. When comparing two groups, Mann-Whitney rank sum test was used.

References

Abdelmohsen, K. and M. Gorospe (2010). "Posttranscriptional regulation of cancer traits by HuR." Wiley Interdiscip Rev RNA **1**(2): 214-229.

Abe, R., E. Sakashita, et al. (1996). "Two different RNA binding activities for the AU-rich element and the poly(A) sequence of the mouse neuronal protein mHuC." Nucleic Acids Res **24**(24): 4895-4901.

Anderson, P. and N. Kedersha (2002). "Visibly stressed: the role of eIF2, TIA-1, and stress granules in protein translation." Cell Stress Chaperones **7**(2): 213-221.

Asangani, I. A., S. A. Rasheed, et al. (2008). "MicroRNA-21 (miR-21) post-transcriptionally downregulates tumor suppressor Pdcd4 and stimulates invasion, intravasation and metastasis in colorectal cancer." Oncogene **27**(15): 2128-2136.

Bhattacharyya, S. N., R. Habermacher, et al. (2006). "Relief of microRNA-mediated translational repression in human cells subjected to stress." Cell **125**(6): 1111-1124.

Brennan, C. M. and J. A. Steitz (2001). "HuR and mRNA stability." Cell Mol Life Sci **58**(2): 266-277.

Carrascoso, I., C. Sanchez-Jimenez, et al. (2014). "Long-term reduction of T-cell intracellular antigens leads to increased beta-actin expression." Mol Cancer **13**: 90.

Cmarik, J. L., H. Min, et al. (1999). "Differentially expressed protein Pdcd4 inhibits tumor promoter-induced neoplastic transformation." Proc Natl Acad Sci U S A **96**(24): 14037-14042.

Dani, C., J. M. Blanchard, et al. (1984). "Extreme instability of myc mRNA in normal and transformed human cells." Proc Natl Acad Sci U S A **81**(22): 7046-7050.

Dember, L. M., N. D. Kim, et al. (1996). "Individual RNA recognition motifs of TIA-1 and TIAR have different RNA binding specificities." J Biol Chem **271**(5): 2783-2788.
Dixon, D. A., G. C. Balch, et al. (2003). "Regulation of cyclooxygenase-2 expression by the translational silencer TIA-1." J Exp Med **198**(3): 475-481.
Dormoy-Raclet, V., I. Menard, et al. (2007). "The RNA-binding protein HuR promotes cell migration and cell invasion by stabilizing the beta-actin mRNA in a U-rich-element-dependent manner." Mol Cell Biol **27**(15): 5365-5380.
Dorrello, N. V., A. Peschiaroli, et al. (2006). "S6K1- and betaTRCP-mediated degradation of PDCD4 promotes protein translation and cell growth." Science **314**(5798): 467-471.
Epis, M. R., A. Barker, et al. (2011). "The RNA-binding protein HuR opposes the repression of ERBB-2 gene expression by microRNA miR-331-3p in prostate cancer cells." J Biol Chem **286**(48): 41442-41454.
Fan, H., Z. Zhao, et al. (2007). "DNA methyltransferase 1 knockdown induces silenced CDH1 gene reexpression by demethylation of methylated CpG in hepatocellular carcinoma cell line SMMC-7721." Eur J Gastroenterol Hepatol **19**(11): 952-961.
Fay, M. M., J. M. Clegg, et al. (2014). "Enhanced Arginine Methylation of Programmed Cell Death 4 Protein during Nutrient Deprivation Promotes Tumor Cell Viability." J Biol Chem **289**(25): 17541-17552.
Forch, P. and J. Valcarcel (2001). "Molecular mechanisms of gene expression regulation by the apoptosis-promoting protein TIA-1." Apoptosis **6**(6): 463-468.
Frankel, L. B., N. R. Christoffersen, et al. (2008). "Programmed cell death 4 (PDCD4) is an important functional target of the microRNA miR-21 in breast cancer cells." J Biol Chem **283**(2): 1026-1033.
Gruber, A. R., J. Fallmann, et al. (2011). "ARESite: a database for the comprehensive investigation of AU-rich elements." Nucleic Acids Res **39**(Database issue): D66-69.
Guo, X. and R. S. Hartley (2006). "HuR contributes to cyclin E1 deregulation in MCF-7 breast cancer cells." Cancer Res **66**(16): 7948-7956.
Hurwitz, J., J. J. Furth, et al. (1962). "The role of deoxyribonucleic acid in ribonucleic acid synthesis. III. The inhibition of the enzymatic synthesis of ribonucleic acid and deoxyribonucleic acid by actinomycin D and proflavin." Proc Natl Acad Sci U S A **48**: 1222-1230.
Izquierdo, J. M. (2008). "Hu antigen R (HuR) functions as an alternative pre-mRNA splicing regulator of Fas apoptosis-promoting receptor on exon definition." J Biol Chem **283**(27): 19077-19084.
Jain, R., T. Devine, et al. (2011). "RIP-Chip analysis: RNA-Binding Protein Immunoprecipitation-Microarray (Chip) Profiling." Methods Mol Biol **703**: 247-263.
Jung, J., A. W. Lifland, et al. (2013). "Quantifying RNA-protein interactions in situ using modified-MTRIPs and proximity ligation." Nucleic Acids Res **41**(1): e12.
Kawai, T., A. Lal, et al. (2006). "Translational control of cytochrome c by RNA-binding proteins TIA-1 and HuR." Mol Cell Biol **26**(8): 3295-3307.
Kawakami, A., Q. Tian, et al. (1992). "Identification and functional characterization of a TIA-1-related nucleolysin." Proc Natl Acad Sci U S A **89**(18): 8681-8685.

Kedersha, N., M. R. Cho, et al. (2000). "Dynamic shuttling of TIA-1 accompanies the recruitment of mRNA to mammalian stress granules." J Cell Biol **151**(6): 1257-1268.
Keene, J. D. (2007). "RNA regulons: coordination of post-transcriptional events." Nat Rev Genet **8**(7): 533-543.
Kim, J., R. Y. Park, et al. (2014). "Splicing factor SRSF3 represses the translation of programmed cell death 4 mRNA by associating with the 5'-UTR region." Cell Death Differ **21**(3): 481-490.
Kishore, S., L. Jaskiewicz, et al. (2011). "A quantitative analysis of CLIP methods for identifying binding sites of RNA-binding proteins." Nat Methods **8**(7): 559-564.
Kulikov, A. V., E. S. Shilov, et al. (2012). "Cytochrome c: the Achilles' heel in apoptosis." Cell Mol Life Sci **69**(11): 1787-1797.
Lal, A., T. Kawai, et al. (2005). "Antiapoptotic function of RNA-binding protein HuR effected through prothymosin alpha." EMBO J **24**(10): 1852-1862.
Lal, A., K. Mazan-Mamczarz, et al. (2004). "Concurrent versus individual binding of HuR and AUF1 to common labile target mRNAs." EMBO J **23**(15): 3092-3102.
Lankat-Buttgereit, B. and R. Goke (2009). "The tumour suppressor Pdcd4: recent advances in the elucidation of function and regulation." Biol Cell **101**(6): 309-317.
Lebedeva, S., M. Jens, et al. (2011). "Transcriptome-wide analysis of regulatory interactions of the RNA-binding protein HuR." Mol Cell **43**(3): 340-352.
Leupold, J. H., I. A. Asangani, et al. (2012). "Promoter cloning and characterization of the human programmed cell death protein 4 (pdcd4) gene: evidence for ZBP-89 and Sp-binding motifs as essential Pdcd4 regulators." Biosci Rep **32**(3): 281-297.
Lopez de Silanes, I., M. Zhan, et al. (2004). "Identification of a target RNA motif for RNA-binding protein HuR." Proc Natl Acad Sci U S A **101**(9): 2987-2992.
Ma, W. J., S. Cheng, et al. (1996). "Cloning and characterization of HuR, a ubiquitously expressed Elav-like protein." J Biol Chem **271**(14): 8144-8151.
Ma, W. J., S. Chung, et al. (1997). "The Elav-like proteins bind to AU-rich elements and to the poly(A) tail of mRNA." Nucleic Acids Res **25**(18): 3564-3569.
Mazan-Mamczarz, K., S. Galban, et al. (2003). "RNA-binding protein HuR enhances p53 translation in response to ultraviolet light irradiation." Proc Natl Acad Sci U S A **100**(14): 8354-8359.
Mukherjee, N., D. L. Corcoran, et al. (2011). "Integrative regulatory mapping indicates that the RNA-binding protein HuR couples pre-mRNA processing and mRNA stability." Mol Cell **43**(3): 327-339.
Pan, X., Z. X. Wang, et al. (2010). "MicroRNA-21: a novel therapeutic target in human cancer." Cancer Biol Ther **10**(12): 1224-1232.
Peng, S. S., C. Y. Chen, et al. (1998). "RNA stabilization by the AU-rich element binding protein, HuR, an ELAV protein." EMBO J **17**(12): 3461-3470.
Piecyk, M., S. Wax, et al. (2000). "TIA-1 is a translational silencer that selectively regulates the expression of TNF-alpha." EMBO J **19**(15): 4154-4163.
Powers, M. A., M. M. Fay, et al. (2011). "Protein arginine methyltransferase 5 accelerates tumor growth by arginine methylation of the tumor suppressor programmed cell death 4." Cancer Res **71**(16): 5579-5587.

Pryzbylkowski, P., O. Obajimi, et al. (2008). "Trichostatin A and 5 Aza-2' deoxycytidine decrease estrogen receptor mRNA stability in ER positive MCF7 cells through modulation of HuR." Breast Cancer Res Treat **111**(1): 15-25.
Pullmann, R., Jr., H. H. Kim, et al. (2007). "Analysis of turnover and translation regulatory RNA-binding protein expression through binding to cognate mRNAs." Mol Cell Biol **27**(18): 6265-6278.
Rogers, G. W., Jr., N. J. Richter, et al. (1999). "Biochemical and kinetic characterization of the RNA helicase activity of eukaryotic initiation factor 4A." J Biol Chem **274**(18): 12236-12244.
Santangelo, P. J., A. W. Lifland, et al. (2009). "Single molecule-sensitive probes for imaging RNA in live cells." Nat Methods **6**(5): 347-349.
Schlichter, U., O. Burk, et al. (2001). "The chicken Pdcd4 gene is regulated by v-Myb." Oncogene **20**(2): 231-239.
Schmid, T., A. P. Jansen, et al. (2008). "Translation inhibitor Pdcd4 is targeted for degradation during tumor promotion." Cancer Res **68**(5): 1254-1260.
Schwanhausser, B., D. Busse, et al. (2011). "Global quantification of mammalian gene expression control." Nature **473**(7347): 337-342.
Shibahara, K., M. Asano, et al. (1995). "Isolation of a novel mouse gene MA-3 that is induced upon programmed cell death." Gene **166**(2): 297-301.
Soderberg, O., M. Gullberg, et al. (2006). "Direct observation of individual endogenous protein complexes in situ by proximity ligation." Nat Methods **3**(12): 995-1000.
Soule, H. D., J. Vazguez, et al. (1973). "A human cell line from a pleural effusion derived from a breast carcinoma." J Natl Cancer Inst **51**(5): 1409-1416.
Srikantan, S., K. Abdelmohsen, et al. (2011). "Translational control of TOP2A influences doxorubicin efficacy." Mol Cell Biol **31**(18): 3790-3801.
Srikantan, S., K. Tominaga, et al. (2012). "Functional interplay between RNA-binding protein HuR and microRNAs." Curr Protein Pept Sci **13**(4): 372-379.
Subramaniam, K., L. L. Ooi, et al. (2010). "Transcriptional down-regulation of IGFBP-3 in human hepatocellular carcinoma cells is mediated by the binding of TIA-1 to its AT-rich element in the 3'-untranslated region." Cancer Lett **297**(2): 259-268.
Sureban, S. M., N. Murmu, et al. (2007). "Functional antagonism between RNA binding proteins HuR and CUGBP2 determines the fate of COX-2 mRNA translation." Gastroenterology **132**(3): 1055-1065.
Tani, H., R. Mizutani, et al. (2012). "Genome-wide determination of RNA stability reveals hundreds of short-lived noncoding transcripts in mammals." Genome Res **22**(5): 947-956.
Tominaga, K., S. Srikantan, et al. (2011). "Competitive regulation of nucleolin expression by HuR and miR-494." Mol Cell Biol **31**(20): 4219-4231.
Uren, P. J., S. C. Burns, et al. (2011). "Genomic analyses of the RNA-binding protein Hu antigen R (HuR) identify a complex network of target genes and novel characteristics of its binding sites." J Biol Chem **286**(43): 37063-37066.
Vikhreva, P. N., M. V. Shepelev, et al. (2014). "mTOR-dependent transcriptional repression of Pdcd4 tumor suppressor in lung cancer cells." Biochim Biophys Acta **1839**(1): 43-49.
von Roretz, C., A. M. Macri, et al. (2011). "Transportin 2 regulates apoptosis through the RNA-binding protein HuR." J Biol Chem **286**(29): 25983-25991.

Wang, H., H. Li, et al. (2011). "Preliminary crystallographic analysis of the RNA-binding domain of HuR and its poly(U)-binding properties." Acta Crystallogr Sect F Struct Biol Cryst Commun **67**(Pt 5): 546-550.
Wang, H., F. Zeng, et al. (2013). "The structure of the ARE-binding domains of Hu antigen R (HuR) undergoes conformational changes during RNA binding." Acta Crystallogr D Biol Crystallogr **69**(Pt 3): 373-380.
Wang, W., M. C. Caldwell, et al. (2000). "HuR regulates cyclin A and cyclin B1 mRNA stability during cell proliferation." EMBO J **19**(10): 2340-2350.
Wang, Z., M. Kayikci, et al. (2010). "iCLIP predicts the dual splicing effects of TIA-RNA interactions." PLoS Biol **8**(10): e1000530.
Wigington, C. P., J. Jung, et al. (2014). "Post-transcriptional regulation of programmed cell death 4 (PDCD4) mRNA by the RNA binding proteins human antigen R (HuR) and T-cell intracellular antigen 1 (TIA1)." J Biol Chem **Under revision**.
Yang, H. S., A. P. Jansen, et al. (2003). "The transformation suppressor Pdcd4 is a novel eukaryotic translation initiation factor 4A binding protein that inhibits translation." Mol Cell Biol **23**(1): 26-37.
Yang, H. S., A. P. Jansen, et al. (2001). "A novel transformation suppressor, Pdcd4, inhibits AP-1 transactivation but not NF-kappaB or ODC transactivation." Oncogene **20**(6): 669-676.
Young, L. E., A. E. Moore, et al. (2012). "The mRNA stability factor HuR inhibits microRNA-16 targeting of COX-2." Mol Cancer Res **10**(1): 167-180.
Zhang, T., N. Delestienne, et al. (2005). "Identification of the sequence determinants mediating the nucleo-cytoplasmic shuttling of TIAR and TIA-1 RNA-binding proteins." J Cell Sci **118**(Pt 23): 5453-5463.
Zhu, H., R. A. Hasman, et al. (2006). "A nuclear function of Hu proteins as neuron-specific alternative RNA processing regulators." Mol Biol Cell **17**(12): 5105-5114.
Zhu, H., M. N. Hinman, et al. (2008). "Regulation of neuron-specific alternative splicing of neurofibromatosis type 1 pre-mRNA." Mol Cell Biol **28**(4): 1240-1251.
Zuker, M. (2003). "Mfold web server for nucleic acid folding and hybridization prediction." Nucleic Acids Res **31**(13): 3406-3415.

CHAPTER 6

FUTURE DIRECTIONS

Introduction

Combining multiply-labeled tetravalent RNA imaging probes (MTRIPs) and proximity ligation assay (PLA) to visualize and quantify RNA-protein interactions *in situ* have allowed for the detection of mRNA-cytoskeleton and mRNA-RBP interactions, which underlie post-transcriptional localization and regulation of mRNAs. Using this method, we revealed a novel mechanism for RBPs to regulate the translation of a tumor suppressor, programmed cell death 4 (PDCD4). Nevertheless, several aspects of this method can be improved. Additionally, this method can be further applied to samples other than cultured cells, such as clinical biopsy and tissues.

Probe design and delivery

When performing PLA experiments, the interactants, mRNAs and proteins, are under-sampled in order to detect their binding randomly for comparative analyses between different samples with varying levels of mRNA or RNA-binding proteins (RBP). Usually, the RNA probes and primary antibodies against the probes are used in concentrations that provide minimal non-specific binding in samples with the highest amount of RNA probes or RBPs. To minimize non-specific interactions and dynamic range of mRNA granules, we typically use RNA probes at concentrations (30-60nM) less than the concentration (90nM) that results in the maximum intensity for the mRNA granules. Reduced concentrations are used to best distribute the probes uniformly across the mRNA granules, to sample the mRNAs randomly, and to visualize most mRNAs

optimally. However, while delivering less probes allows for detection of relative differences between samples, it has an unwanted effect of possibly detecting only a few interactions in samples with the lowest level of mRNAs.

In order to improve this method so that mRNAs can be detected more accurately without sacrificing the dynamic range of probe imaging (imaging only a few granules with the highest fluorescent intensity), probes with fluorophores can be delivered at a less concentration of 30-60nM, while probes without fluorophores are delivered at a concentration (60-30nM) such that the total probe concentration equals the concentration that results in the maximum intensity (90nM). This may allow for maximizing both the sampling of mRNA and the frequency of mRNA-protein interactions.

RNA-protein interaction detection

PLA relies on two enzymatic reactions: ligase and phi29 DNA polymerase. The ligase allows for bridging of two oligonucleotide tails on the secondary antibodies, termed PLA probes, bound to the interactants when the two interactants are less than 30-40 nm apart. Phi29 DNA polymerase allows for one of the two oligonucleotides on the secondary antibodies to serve as a primer for rolling circle amplification (RCA). Three mismatched exonuclease-resistant 2'O-methyl RNA nucleotides at the 3' end prevent the other of the two oligonucleotides from acting as a primer. This reaction results in a coiled single-stranded DNA, the PLA product, complementary to the circular DNA strand and covalently bound to the antibody-antigen complex. The PLA product is detectable by hybridizing complementary fluorophore-labeled oligonucleotides.

Although these enzymatic reactions are generally predictable, it can be variable and difficult to optimize. Ensuring uniform enzymatic reactions across all the samples is impossible. When using primary antibody concentrations that allow for maximal coverage of the samples as detected by fluorophore bound secondary antibodies, non-specific signal is prevalently observed in negative controls lacking the primary antibody. Although comparatively, significantly more signal is observed in the positive control, the experimental results are often difficult to demonstrate with such high variable levels of non-specific PLA products. This prevalence of non-specific signal and variability in PLA products due to non-uniform distribution of enzymatic reactions can be resolved potentially by using a method that does not rely on enzymatic reactions.

Hybridization chain reaction (HCR) is a method that uses two fluorophore-bound DNAs in hairpin motif that contain complementary sequences that allow for the opening and binding of the hairpins, which result in a long, fluorescent strand of two opened DNA hairpins bound together by Watson-and-Crick pairing. Although these DNA hairpins remain closed and do not open at room temperature, they can open and bind more readily at higher temperatures. HCR may replace the enzymatic reactions. Theoretically, a DNA sequence can be designed to encode a complementary sequence to the two oligonucleotides on the PLA probes as well as a sequence that can initiate the opening of fluorophore-bound DNA hairpins. This DNA can bind to the oligonucleotides on the PLA probes in close proximity via Watson-and-Crick pairing and can be detected by a cascade of opened fluorophore-bound DNA hairpin strands.

This HCR method would allow for detection of protein-protein or RNA-protein interactions without necessitating enzymes. Moreover, the components of this method are

all DNA; therefore, less costly than conventional PLA. The DNA reactants can be easily designed and purchased commercially. These DNA binding and hairpin reactions can be achieved by simply modifying the conventional fluorescent in situ hybridization protocol. There may be numerous advantages to using HCR rather than conventional PLA. However, further studies must be performed to demonstrate the benefits of HCR.

Detecting multiple interactions

The PLA may be modified to detect interactions between more than two biomolecules. For example, it may be used to detect whether one mRNA is simultaneously bound to two proteins. This may be useful in detecting the interplay between RBPs and miRNAs in post-transcriptional regulation of mRNAs. PLA maybe used to sense interactions between RBPs and the RNA-inducing silencing complex (RISC) with specific mRNAs. This would allow for the coordination of RBPs and miRNAs to be studied.

In order to achieve this, the current PLA used for RNA-protein interactions need to be modified. Additional PLA probes and bridging DNA sequences would need to be designed and synthesized such that the PLA product is synthesized only when all three oligonucleotide strands on the PLA probes are in proximity. They should be designed to achieve high specificity and to avoid inaccurate detection in the presence of two of the three components. This may be further modified such that PLA of one fluorescent signal would be present for interactions consisting of two of the components and another fluorescent signal in a different color would be present for interactions consisting of all three components.

High-throughput analysis

Our current PLA method could easily be adapted for high-throughput analysis. For example, cells can be plated into multi-well plates. Each well with a few cells can be examined for specific interactions. Interactions between an array of RBPs and specific mRNAs can be examined rapidly using a plate reader or a microscope. A useful experiment would be to first determine the baseline variability in mRNA-RBP interactions for various cell population. Quantitative characterization of the distribution of these interactions for various mRNAs and RBPs would be helpful in establishing the cell-to-cell variability for these post-transcriptional regulatory events.

Moreover, implementing PLA in a high-throughput setting would streamline the experiments that examine how multiple RBPs affect the expression of multiple genes. For example, how a group of RBPs affect expression of a family of cytokine genes can be studied by examining interactions between these RBPs and these cytokine mRNAs in multi-well plates. The level of mRNA can be detected via mRNA probe signal, the frequency of interactions via PLA signal, and the protein signal via ELISA. Using these methods, multiple genes and multiple RBPs can be studied rapidly.

Broadening the application

In our lab, PLA experiments have only been performed in cells grown on coverslips. Although they were effective experimental models for demonstrating the method and describing acute changes in the cells, applying this method to biopsied cells or tissues would allow for more clinically relevant questions to be addressed. Additionally, PLA may be applied to cells grown in three-dimensional settings may allow

for detection of RNA-protein interaction changes in spatial variations. Further experiments would need to be performed to accurately apply this method in different settings, such as tissues and three-dimensional cellular models. However, these samples may be thinly sliced and examined with PLA by using a modified version of the conventional immunohistochemistry protocols.

Investigating post-transcriptional regulations

Our examination of competition between HuR and TIA1 for post-transcriptional regulation of PDCD4 demonstrate that RBPs may modulate mRNA and protein levels of a gene not only by binding to their targets but also by influencing the binding of other RBPs and possibly, miRNAs. To study how various RBPs regulate the gene expression coordinately, PLA can be used to further examine interactions of other RBPs, such as tristetraprolin, TIAR, or CUG-BP, with mRNAs. Identifying the locations of these RBPs and whether they bind cooperatively or competitively with the other RBPs can help establish a model system for examining how changes in RBPs modulate mRNAs and their translation. We can also study how RBPs affect miRNA binding or vice versa by examining interactions between the RNA-induced silencing complex (RISC) and RBPs.

VITA

JEENAH JUNG

Jeenah Jung was born in Seoul, South Korea and raised in Glenview, IL. There, she attended public schools and graduated from Glenbrook South High School. She received a B.A. in Chemistry from Wellesley College in Wellesley, MA, where she worked for Nolan Flynn at Wellesley College. She worked with Matthew Wilson at Massachusetts Institute of Technology as an undergraduate research student and a laboratory technician, before coming to Emory University and Georgia Institute of Technology to pursue doctorates in medicine and biomedical engineering.